DATE DUE	DATE DUE	DATE DUE

THE DEVELOPMENT OF NON-CONTACT AND NON-DESTRUCTIVE EXPERIMENTAL TECHNIQUES CAPABLE OF MEASURING THE THERMAL DIFFUSIVITY OF CVD DIAMOND FILM.

Matthew J. White

A Thesis
Submitted to Michigan State University
in partial fulfillment of the requirements for
the degree of

MASTER OF SCIENCE

Department of Mechanical Engineering

1996

ABSTRACT

THE DEVELOPMENT OF NON-CONTACT AND NON-DESTRUCTIVE EXPERIMENTAL TECHNIQUES CAPABLE OF MEASURING THE THERMAL DIFFUSIVITY OF CVD DIAMOND FILM.

By

Matthew J. White

A new optical, non-contact, and non-destructive experimental technique has been developed. When used with existing analytical tools, this system is capable of estimating the thermal diffusivity of thin films. A significant portion of this work is devoted to establishing the general capabilities of the experimental components. The major components include two infrared temperature measurement devices, a Q-Switched Nd:YAG laser, instrumentation for laser beam diagnostics, and a data acquisition and instrument control system.

Beyond the development, estimates for the thermal diffusivity of copper, iron and CVD diamond film were obtained. In these experiments, the Nd:YAG laser was used to perturb the thermal equilibrium of the sample and infrared thermography was used to record the established temperature gradients. The method of least squares was used to minimize the errors between the measured temperatures and the calculated temperatures determined from a one dimensional quasi-steady state model.

to my family

Acknowledgments

I would like to take this time to thank my co-advisors, Professor J.J. McGrath and Professor J.V. Beck. I feel they provided me with an excellent example of how to conduct myself as an engineer, a researcher, and most importantly as a person. I believe the skills I developed under their guidance will help me successfully overcome any hurdles placed in front of me in the future.

I would also like to thank colleagues such as Kevin Dowding, Heidi Relyea, Scott Morris, and Dr. Moshen Shabana. Each of these individuals were always willing to take the time to give a creative suggestion or if need be a meticulous explanation.

My thanks go out to Professor C.W. Somerton for his review of the present work. Beyond Professor Somerton's ability as instructor, his guidance over the past two years was very helpful.

A special thanks goes out to my family. They always encouraged me to strive for my goals and were willing to make the necessary sacrifices so I could be in a position to obtain them. They may never realize the degree to which their support and encouragement over the past few years was appreciated.

As I write this thesis I close the chapter on my days at Michigan State University. M.S.U. has provided an environment in which I have had an opportunity to mature as a person, meet some great people, and enjoy some good times. All this while obtaining a high quality education. As I look back through all the good memories, however I leave Michigan State with one regret. I believe a person can never have enough friends, and the

way I conducted myself during recent stressful periods seemingly cost me a great friend. I hope some day she will forgive me.

Table of Contents

Chapter

List of Tables

List of Figures

Nomenclature

k	Thermal Conductivity	[W/m °C]
α	Thermal Diffusivity	[m^2/s]
C_p	Specific Heat	[J/Kg K]
ε	Emissivity	
τ	Transmissivity	
ρ	Reflectivity	
ρ_m	Mass Density	[kg/m^3]
T	Temperature	[°C]
S	Least Squares Funciton	
t, τ	Time	[sec]
β	Eigenvalue	
r, r'	Cylindrical Coordinate	[m]
β_j	Estimate Parameter	
μm	Micron	[10^{-6} m]
Hz	Hertz	[cycle/sec]
q	Heat Flux	[W/m^2]
g	Heat Generation	[W/m^3]
δ	Sample Thickness	[m]

a, b	Radial Distances	[m]
T_i	Initial Temperature	[°C]
Y_j	Measured Temperature	[°C]
T_j	Calculated Temperature	[°C]
F_o	Fourier Number	

Subscripts / Superscripts

QS	Quasi-Steady State
TR	Transient Term
I	Initial
j	Indexing Constant
r,x,y,x	Directions

Chapter 1

Introduction

Since the time Fourier so concisely set forth the principles of heat conduction, the theoretical treatment of heat transmission through media has and will continue to be important to many fields of science and engineering. The advent of the mechanical refrigerator in the late 1920's brought about a need for insulating materials and an increased interest in thermal conductivity measurements. In the late 1930's and early 1940's an increased need to know the thermal conductivity of metals was in evidence and further accelerated by nuclear energy and missile developments [Lucks, 1963]. The space race in the late 1950's and early 60's brought about a considerable advancement in parameter estimation as the design of reentry heat shields became a major issue [Beck, 1996]. The most recent impetus to this type of measurement is associate with the emphasis on semi-conductors, heat sinks and high performance materials. Thermal conductivity measurements are now being made over a wide spectrum of materials and

range of temperatures. Consequentially, many methods are now being used for these measurements.

One material under scrutiny by the scientific world is diamond. Well known for its aesthetic beauty and for its practical importance, diamond is a material which has fascinated humankind since the early ages. Not only is it one of the rarest gem in the world, but diamond is both harder and conducts heat better than any other known substance. These two physical properties make diamond an excellent choice for many technical applications, such as cutting, abrasion, protective coatings, and heat conduction, to name a few. The use of diamond in such application has been hindered by the difficulty and expense encountered by an experimentalist as he/she tries to synthesize diamond in the laboratory.

Over the past 15 years the situation has changed to a large degree as researchers have explored new and innovative techniques to synthesize diamond films. In particular, a great deal of attention has been focused on growing diamond using far-from-equilibrium thin growth techniques such as microwave or hot filament chemical vapor deposition (CVD)[Jones, 1994]. This approach has been inviting since many applications, particularly in the electronics industry, require thin films. It is progress such as this that will be responsible for transforming diamond from a rare jewel into a viable engineering solution.

Before diamond can be used in thermal applications, it is important to gain a complete understanding of how these films conduct heat. A great deal of work has been done which illustrates that the thermal conductivity of diamond film is related to the film thickness, ambient temperature, amount of impurities, and growth techniques. This thesis

discusses the development of a new general purpose system capable of measuring the thermal diffusivity of these films. This system incorporates non-destructive and non-contact experimental techniques with the analytical tools necessary for thermal physical property estimation.

1.1 Objectives

The objective of this research was the development of experimental methods and the use of analytical tools which would allow for the thermal analysis of various materials of manufacturing interest. The primary objective is to utilize these techniques to measure the thermal diffusivity of diamond films. In particular the objectives were:

1.) To develop the general capabilities of an experimental system capable of measuring the thermophysical properties of thin films. The components within this system provide optical, non-contact, and non-destructive temperature measurement and heating techniques.

2.) To demonstrate the utility of this system by measuring the thermal diffusivity of three CVD diamond films.

3.) To validate this newly developed system along with existing analytical tools by determining the thermal diffusivity of high purity copper and iron samples. These materials were selected as verification materials due to their well defined thermal properties.

Chapter 2

Background and Literature Review

Perhaps the area of greatest potential for diamond films is in commercial and military electronics [Herr 1993]. As electronic components becomes smaller and more dense, temperature increases become a critical issue concerning their performance and reliability. This issue currently limits the miniaturization of high-power electronic systems. Because of their high thermal conductivity and large dielectric constant, diamond materials are expected to successfully address the problem of local heat build-up. One example for the passive use of diamond films is the silicon on diamond (SOD) technology which employs these films as a direct substrate for the silicon micro-components [Annamalai et al, 1993]. As diamond insulates the electronic circuits, heat is effectively dissipated to the substrate (provided good contact between the circuits and diamond can be established). Thin diamond films have shown promising applications in radiation

detectors, field effect transistors and sensors [Tamor and Aslam, 1994]. These application potentials have propelled the development of diamond thin film synthesis techniques, but the direct applicability of diamond films may be limited until a through understanding of the thermophysical properties can be developed.

2.1 - CVD Diamond Films

Diamond films, like the gem, consists of carbon atoms bonded together in strong sigma type covalent bonds. The atomic orbitals are sp^3 and the bonds formed are very strong. The carbon atoms are arranged in a tetrahedral formation resulting in the diamond cubic unit cell seen in Figure 2.1.

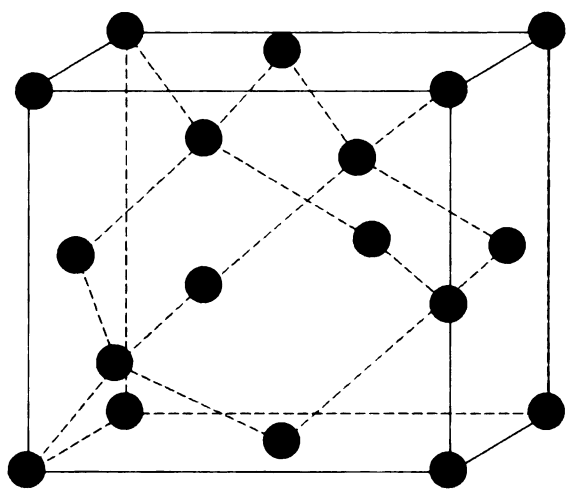

Figure 2.1. *The diamond cubic unit cell.[Herr 1993]*

The structure of diamond gives rise to the extreme hardness with the ability to withstand pressures over 900,000 lbs/in^2. The stiffness of the these unique molecular bonds also contribute to the diamond's high thermal conductivity [Herr 1993]. In nonmetallic

materials, heat conduction primarily occurs through a phonon transfer phenomenon. This mechanism, which is dependent on the molecular vibrational energy and the amount of defects and/or impurities, is most efficient when atomic bonds are stiff and dampened when bonds are elastic.

Through a process known as Chemical Vapor Deposition (CVD), polycrystalline diamond films can be deposited on a variety of substrates, including Si, SiC, WC, Ta, W, Mo, and Al_2O_3. The two most commonly used CVD methods are the hot filament assisted method and plasma enhanced microwave method. Recent variations of these methods have resulted in steadily increased growth rates. However, Common in all techniques a high supersaturation of atomic hydrogen is created along with a supersaturation of carbonic species and a substrate temperature in the range of 600 C - 1000 C [Jones, 1994]. Other similarities include process parameters of gas pressure, the percentage of hydrogen in the gas phase, and the resulting film morphology. However, there are a number of other specific process parameters which are considerably different from technique to technique. These process parameters lead to differences in the energy partitioning in the deposition process, the deposition efficiency, deposition rate, film purity, physical properties and film uniformity to name just a few [Jones, 1994].

Regardless of the technique, the film qualities are dependent on the deposition conditions. Generally, a diamond film grown on a non-diamond substrate will have a highly faceted, large grained (>1μm) film morphology as shown in Figures 2.2(a) and 2.2(b). However, if the growth parameters are not optimized, especially the substrate temperature and the methane concentration, the morphology becomes submicrocystalline and cauliflower-like as shown in Figure 2.2(c) [Stoner *et al*, 1991].

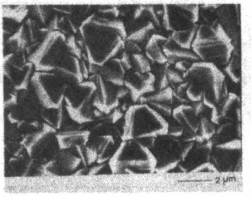

(a.)

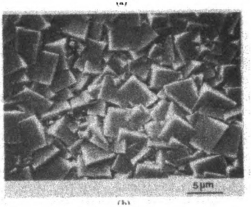

(b.)

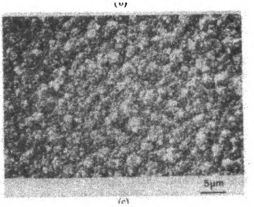

(c.)

Figure 2.2. *Scanning Electron Microscope (SEM) micrographs of diamond films with typical surface morphologies with (a.) trigular shaped crystal faces, (b.) square shaped crystal faces, and (c.) cauliflower-like crystalline aggregates [Stoner et al, 1991].*

The extreme properties and application potential of diamond has spawned research into the CVD process. Over the past few years this research has increased the quality of the synthesized diamond films. However, even when using the best CVD system one must be aware that a certain amount of impurities and defects normally are present as a result of this process. It is these impurities which have a major effect on the film's physical properties. For example, Baba et al. (1991) reported that by increasing the methane concentration from 1% to 5% the thermal conductivity decreased from 1200 W/mK to 200W/mK. This reduction was assumed to be the result of phonon scattering due to the hydrogen impurity found in the films. The thermal conductivity can also be severely affected by structural defects in the film. Grain boundaries can result in poor thermal contact within the film [Graebner et al, 1991]. Since CVD diamond films are prone to impurities and small defects, the application of such films as heat sinks could be quite restrictive without experimentally determining the thermal conductivity and relating it to deposition technique [Herr, 1993].

Chapter 2.2 - Methods for Determining Thermophysical Properties

2.2.1 Standard Methods

Generally, methods of determining the thermophysical characteristics of materials are divided into three groups: steady state experiments, quasi-stationary methods, and transient methods [Vorobei, 1986]. The American Society of Test and Materials (ASTM) annual book of standards recommends two procedures for experimentally determining a material's thermophysical properties. The limitations of these methods are significant and can be observed by closely inspecting each method. The "flash method" is cited as the

standard technique for determining the thermal diffusivity (ASTM 1995a). In practice this method subjects one side of a small disk shaped sample to an energy pulse with a duration on the order of milliseconds. Solid state lasers or flash lamps are used to provide the energy burst. The temperature rise on the opposite side of the sample is then recorded via a pyrometer or thermocouple. A vacuum enclosure containing a resistive heater provides environmental control. One dimensional heat transfer theory is applied and from the measured temperature rise the diffusivity is determined. The main limitation of this transient test procedure is that it only determines the thermal diffusivity in one location.

The standard method for determining the thermal conductivity is a guarded-comparative-longitudinal heat flow technique [ASTM, 1995b]. Typically, a heat source and heat sink are applied at opposite ends of a composite rod system formed by rods of know and unknown conductivities. Thermocouples are embedded inside the rods along the longitudinal axis and the whole system is surrounded by insulating material and auxiliary heaters to act as a one-dimensional heat flow guard. Thermal conductivity, k, can be calculated by the one-dimensional steady state Fourier equation under those conditions. This technique is limited because it does not allow for in situ measurement and requires the destructive insertion of thermocouples.

2.2.2 Variations to Standard Methods and Special Experiments for CVD Diamond Film

In both of the above standard tests, a heat source is used to perturb the thermal equilibrium in the material of interest. The phenomenon of heat conduction attempts to restore equilibrium by allowing heat to flow down temperature gradients. By measuring

this temperature gradient and quantifying the amount of applied heat, the thermophysical properties can be estimated [Herr, 1993]. Over the past several years, researchers have used this idea to develop new experimental techniques and analytical tools to estimate the thermal properties of CVD diamond film.

The polycrystalline anisotropic nature of diamond films also presents an interesting problem. As with other anisotropic thermally conducting materials techniques had to be developed which allowed for the determination of the thermal conductivity both parallel ($k_{\parallel}$) and perpendicular ($k_{\perp}$) to the surface of the film.

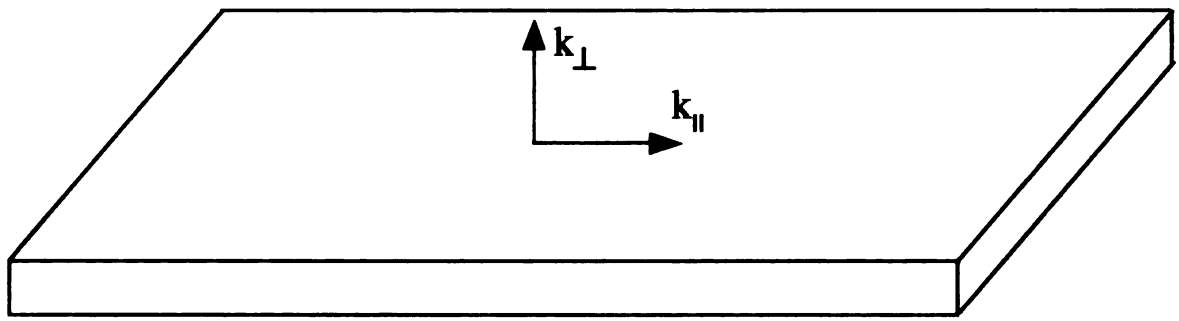

Figure 2.3. *Thermal conductivity parallel ($k_{\parallel}$) and perpendicular ($k_{\perp}$) to the surface of the film [Herr, 1993].*

The different experimental techniques used in these works can be divided into three categories: surface instrumentation, non - contact temperature measurement, and photothermal laser beam deflection. In the following pages different variations of these experimental techniques will be discussed.

Surface Instrumentation

Thermocouples, thermistors, and other surface instrumentation are commonly used by researchers to detect and record the temperature distribution on the surface of diamond films. In 1988 Morelli, Beetz and Perry used a four probe thermocouple probe to estimate the parallel thermal conductivity of diamond films created using hot filament CVD as a function of temperature. In this experiment two free standing diamond films with lateral dimensions of approximately 10 mm x 5 mm and thickness on the order of 15μm were tested. A thin film heater was attached to one end of the film and the temperature distribution was recorded using type T thermocouples. Of crucial importance to this experiment, was the minimization of heat loss due to convection and radiation. This was accomplished by placing the experimental samples between two metal shrouds within a vacuum. The heat input and temperature distribution were recorded at steady state and the thermal conductivity of the two samples was determined as a function of temperature. The absolute uncertainty in their data (~15%) is determined by the accuracy to which the film thickness can measured. The results of their experiment are shown in Figure 2.4.

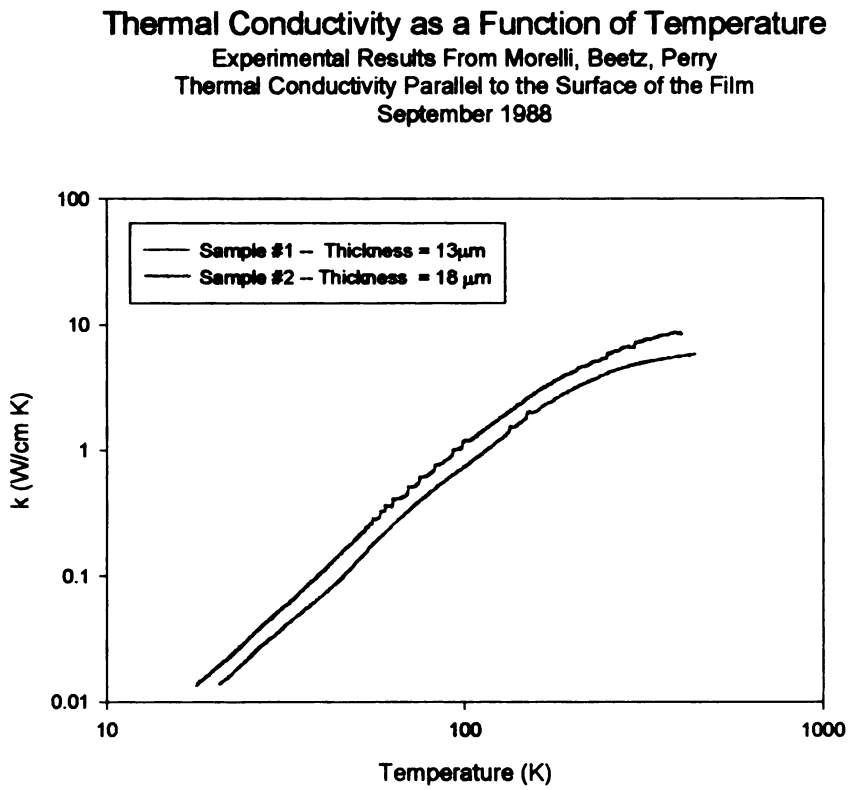

Figure 2.4. *Thermal conductivity of two diamond films as measured by Morelli, Beetz and Perry. The films used in this experiment were created using the hot filament assisted CVD method.*

Baba, Aikawa, and Shohata (1991) studied the thermal diffusivity parallel to the surface of the film. In this case, the diamond films were grown on Si substrates by the hot-filament CVD technique in gas mixtures of 1% to 5% methane concentration, and measurements were made using a AC calorimetric method. In their experiment, one end of the sample was periodically heated using a with a halogen lamp. The temperature at a distance x from the heated area was monitored using a thermocouple directly attached to film's surface. The relation between the temperature and distance is given by the following equation,

$$\ln|T| = \ln(q / 4\pi fCd) - (\pi f / \alpha)x \tag{2.1}$$

where q is the heat quantity absorbed by the sample, f is the heating frequency and C, d, and α are the specific heat, thickness, and thermal diffusivity of the sample respectively. The thermal conductivity was extracted from the thermal diffusivity of the samples and evaluated from the slope of Eqn 2.1 by varying x. Their results illustrate that the thermal conductivity for diamond films was dependent on the amount of hydrogen impurity deposited from the methane gas mixture. For example, as the methane concentration during the synthesis process is increased from 1% to 5%, the thermal conductivity decreased from 1200 W/mK to 200 W/mK.

Graebner, Muncha, Seibles, and Kammlott (1992) used a procedure similar to the Morelli, Beetz and Perry method to determine that the diamond film thermal conductivity was inversely proportional to the growth rate. In their procedure the silicon substrate was etched creating a 2 x 4 mm^2 free standing window. The remaining silicon substrate served as a rugged platform as well as a heat sink and reference temperature. The flow of heat from the thin foil heater in the center of this window was monitored with thermocouples. The steady state temperature distribution was then compared with a numerical simulation to extract a value for the thermal conductivity. The window dimensions were chosen in an effort to minimize the effect of radiation. To predict the influence of radiation they developed the following ratio,

$$\frac{k_{rad}}{k_{cond}} \sim \frac{2\sigma\varepsilon W^2 T_o^3}{\kappa t} \tag{2.2}$$

where k_{cond} is the conductance along the film of thickness t, k_{rad} is the effective conductance due to radiation between the film and its surroundings, α is the Stefan-Boltzmann constant, ε is the emissivity, T_o is the initial temperature, and κ is the thermal conductivity. For example, they were able to use Eqn 2.2 and determine that even under non-ideal conditions ($\varepsilon = 1$, T_o=300 K, t=2μm, k=3 W/cm K) the effects of radiation could be ignored if the proper width dimensions were selected. The results of their study are shown in Figure 2.5.

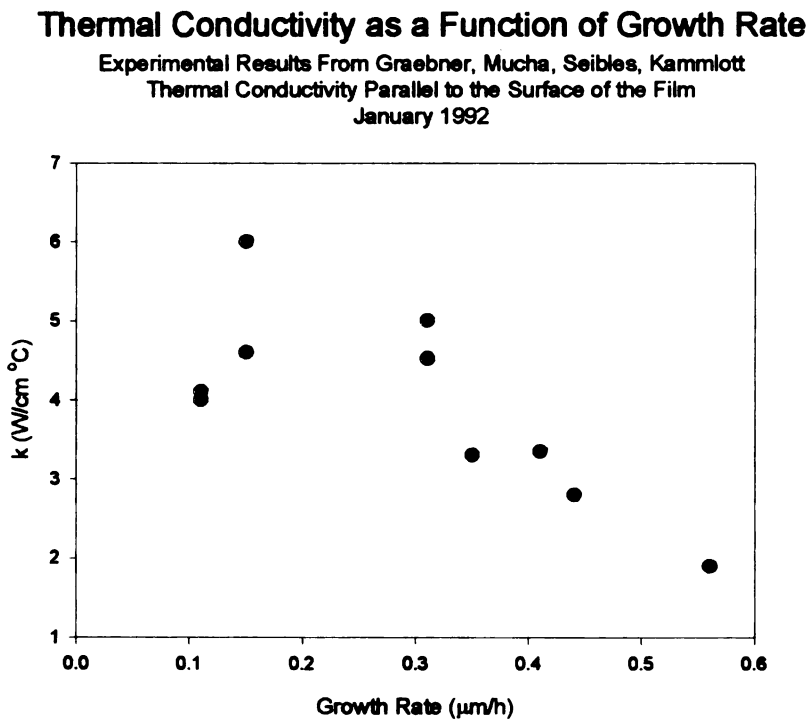

***Figure 2.5** Graebner, Muncha, Seibles, and Kammlott (1992) results for the Thermal Conductivity parallel to the surface of the film ($k_{\parallel}$). The diamond films in this study were created using a microwave-plasma CVD technique.*

Later in 1992 Graebner, Jin, Herb, Kammlott, and Gardinier introduced another similar technique to determine the parallel thermal conductivity. This method employees two thin-film heaters evaporated directly onto each end of a bar shaped sample. The temperatures between the heaters were monitored by a row of four fine diameter thermocouples attached to the surface with silver-epoxy. A schematic representation of the experimental setup is shown in Figure 2.6. The tests were conducted on samples with different thicknesses and the samples were placed in a vacuum where the effects of radiation and convection could be avoided. From their test, Graebner, Jin, Herb, Kammlott, and Gardinier were able to show that the thermal conductivity of diamond was a function of film thickness. Their results are shown in Figure 2.7.

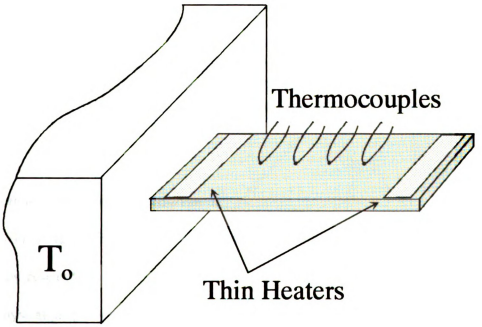

Figure 2.6. *Schematic diagram of the experimental setup used by Graebner, Jin, Herb, Kammlott, and Gardinier for determining the parallel thermal conductivity.*

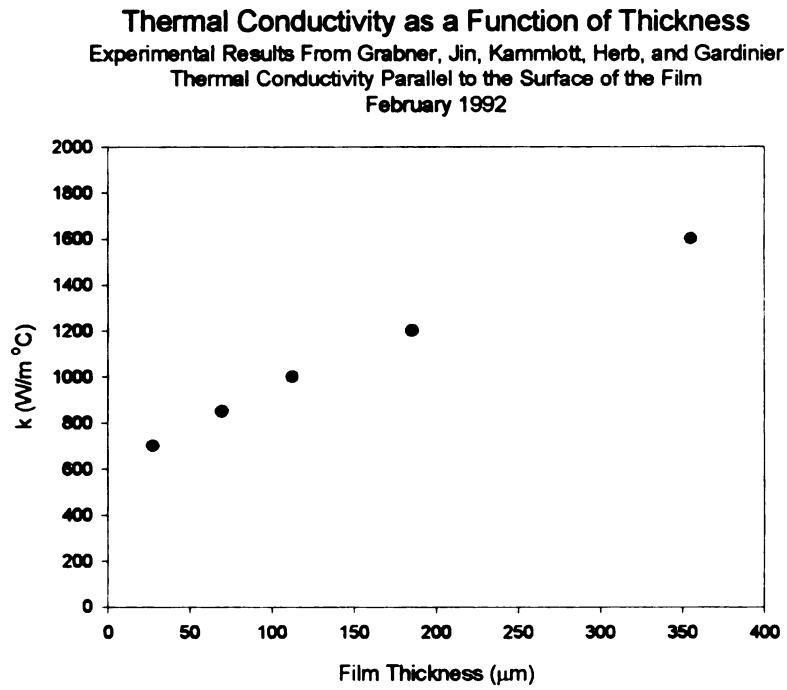

Figure 2.7. *Graebner, Jin, Herb, Kammlott, and Gardinier (1992) results for the thermal conductivity parallel to the surface of the film. These results show an increase in thermal conductivity by more than a factor of two as the thickness is increased by a factor of ten.*

Non - Contact Temperature Measurement

Non-contact infrared temperature measurement systems have been and continue to be used by researchers to capture and record the temperature distribution necessary for thermophysical property estimation.

Ono, Baba, Tunomoto and Nishikawa (1986) utilized a non-contact method to determine the thermal conductivity parallel to the film surface. Using a long diamond film sample suspended by heated supports in a vacuum, the temperature distribution along the

length was measured using infrared thermography. The surface area of the samples analyzed was 20 mm x 5 mm while the thicknesses varied between 7-30 mm. Measurements were made between 100°C and 130°C on microwave plasma CVD diamond. From the results of this study, the thermal conductivity of the diamond films was found to rapidly increase with decreasing concentration of methane. The highest value for $k_{\parallel}$ was approximately 1000 W/m K.

Another significant study determining the $k_{\parallel}$ of diamond films using IR thermography was done later by Albin, Winfree, Crews (1990). The thermal conductivity was extracted from measurement of thermal diffusivity. Periodic heating was provided by a 20W, 1.064 μm Nd:YAG laser and the time dependent surface temperature was measured by a 8-12 μm infrared camera. A diagram of the setup is shown in Figure 2.8.

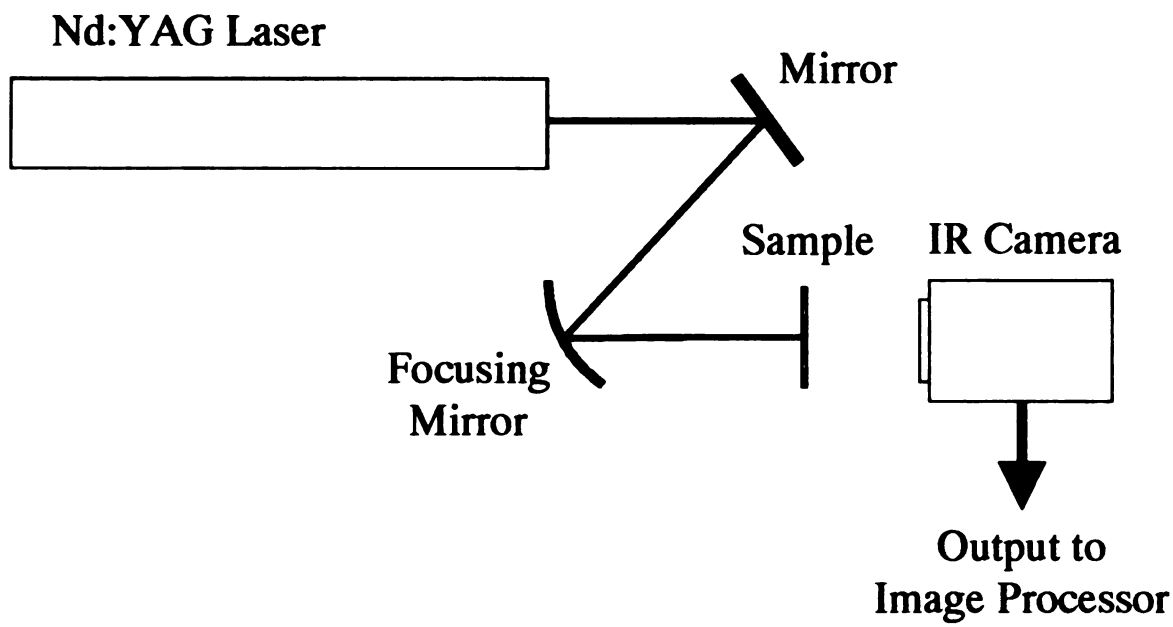

Figure 2.8. *Schematic representation of the experimental setup used by Albin, Winfree, Crews to measure the thermal conductivity parallel to the surface of the film.*

Temperature measurements between 25-35°C were made on the back side of the sample using the infrared camera. The camera scanned a single horizontal line which passed through the center of the sample of the heating area. An image processor was used to digitize 128 successive images. Each image was compressed into a single temperature profile resulting in a sampling rate of 1/30 of a second. The IR camera allowed for a temperature resolution of less than 0.02°C and a spatial resolution of better than 1mm. In this study $k_{\parallel}$ for two samples of thickness 16 and 32 mm were determined to be 1350 and 1328 W/m K respectively. The major advantage of their technique is that the thermal diffusivity and thermal conductivity of diamond films can be determined without special sample preparation.

In 1992 Lu and Swann measured the in plane thermal conductivity of CVD diamond films using a converging wave technique. As shown in Figure 2.9 a 5 J/pulse ruby

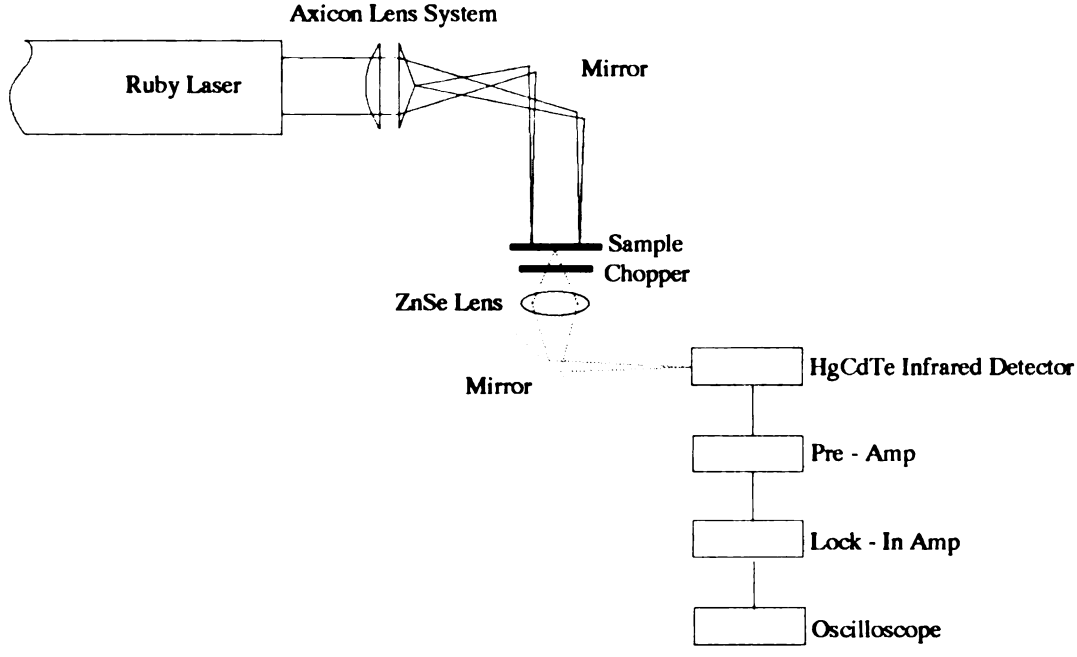

Figure 2.9. *Schematic representation of the converging wave apparatus used by Lu and Swann for determining the thermal conductivity parallel to the surface of the film.*

laser was converted into a ring of light with a positive axicon (lens of conical cross section) with an angle of 2°. The ring was focused onto the sample and heated in a sharp annular pattern. A HgCdTe detector was focused on the center of the back surface of the sample. This detector was used to monitor the time required for the heat to travel from the perimeter of the ring to the center of the sample.

For a thin sample (thickness << radius), the temperature at the center of the ring is given by:

$$T = \left[E / 4\pi\rho C_p \alpha t\right] \exp\left(-R^2 / 4\alpha t\right) \tag{2.3}$$

where E is the energy absorbed per unit thickness, ρ is the density, C_p is the specific heat , α is the thermal diffusivity, t is the time, and R is the radius of the ring. The diffusivity is determined by:

$$\alpha = R^2 / 4t_m \tag{2.4}$$

where t_m is the time needed to reach the maximum temperature at the center of the ring. Based on this measured thermal diffusivity the thermal conductivity was extracted and determined to be 1280 W/m K.

Lu and Swann chose this technique because it could be used on samples of varying and unknown thickness, is independent of laser power, and yields accurate measurements in less than a minute.

While it is relatively straightforward to measure $k_{\parallel}$ using surface instrumentation and non-contact infrared cameras, it is much more difficult to measure $k_{\perp}$ due to the small

thermal resistance in this direction [Graebner et al. 1992]. For this reason high speed infrared detectors are being used by many researchers for temperature acquisition.

Graebner, Jin, Kammlott, Bacon, and Seibles (1992) employed a non-contact temperature acquisition method to determine the thermal conductivity perpendicular to the surface of the film ($k_{\perp}$). Basically their procedure, shown in Figure 2.10 was similar to the standard "laser flash" discussed in Section 2.2.1. In this case, pulses of radiant energy were used to heat one face of the sample and fast IR thermography was used to monitor the arrival of the thermal response on the opposite face.

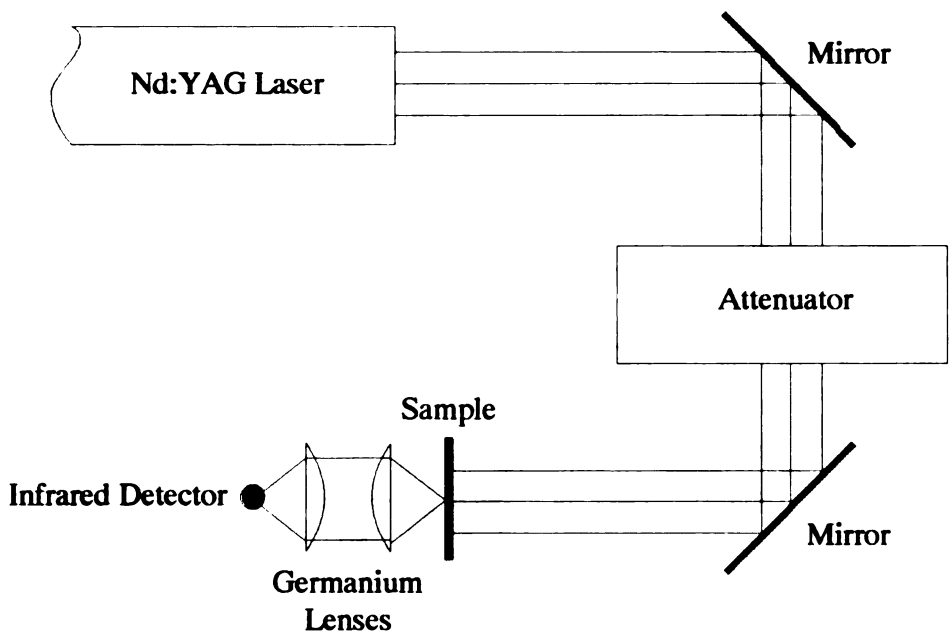

Figure 2.10. *The experimental arrangement used by Graebner, Jin, Kammlott, Bacon, and Seibles to measure the thermal conductivity perpendicular to the surface of the film.*

A Q-Switched Nd:YAG laser was used as the heat source. The sample was glued with silver paste over a hole in a temperature-controlled copper plate. Germanium lenses were used to collect thermal radiation from one side of the sample. Heat was conducted

laterally through the sample to thermal ground at its edges. The temperature rise on the back surface and the rapid transient response were recorded by the data acquisition system. An expression for the change in temperature with respect to time corresponding to short heating pulses such as this was analytical determined by Parker *et al.* in 1961 as,

$$\Delta T(t) = A\left[1 + 2\sum_{n=1}^{\infty}(-1)^n \exp\left(\frac{-n^2\pi^2}{L^2}\alpha t\right)\right] \tag{2.5}$$

where $A = q/\rho C_p L$ and $\alpha = k_\perp/\rho C_p$; q is the absorbed energy per unit area; L is the sample thickness and α is the thermal diffusivity. Eqn. 2.3 is used to solve a system of equations where A and α are the unknown quantities. By solving for the thermal diffusivity and measuring both the thermal response and characteristic length of the film (film thickness), the thermal conductivity, $k_\perp$, was calculated assuming a value for ρC_p. Conductivities, $k_\perp$, of 800 and 1210 W/mK were found for two different samples with thicknesses of 234 and 144μm respectively. When compared to $k_\parallel$ measurements made on the same films, it was shown that the thermal conductivity through the thickness of the film could be as much as 50% higher than the thermal conductivity parallel to the surface of the film.

In January of 1993, Graebner, Jin, Kammlott, Herb, Wong, and Gradinier utilized the same setup to complete an in depth study on $k_\perp$. In their study, several films were synthesized using similar deposition techniques and the results show that $k_\perp$ increases with film thickness. These results are shown in Figure 2.11.

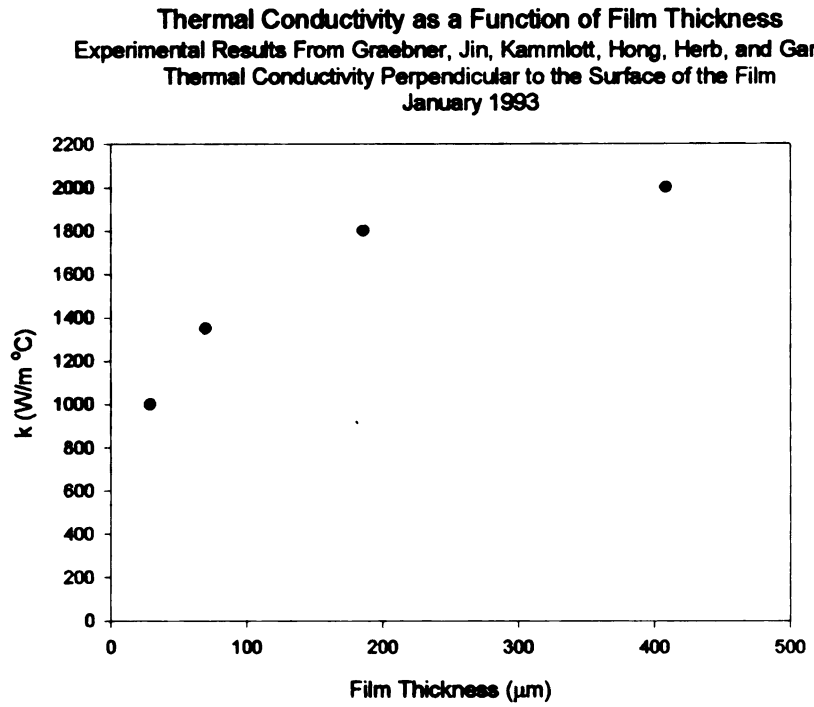

Figure 2.11. *Thermal conductivity measurements perpendicular to the surface of the film. In these test conducted by Graebner, Jin, Kammlott, Herb, Wong, and Gradinier it is clear that* $k_{\perp}$ *increases with film thickness.*

Photothermal Beam Deflection:

The technique known as photothermal laser beam deflection was introduced by Petrovsky, Salnick, Mukhin, and Spitsyn (1993). This is another of many alternate methods of determining $k_{\parallel}$ in diamond films. This technique also know as the "mirage effect" uses the assistance of two separate laser beams

One beam generates heat pulses within the sample producing heat pulses in the air above the sample. The thermal pulse in the air results in an optical index of refraction gradient. The second beam passes through the established gradient and is deflected with components both in plane and perpendicular to the plane of the sample. Since the heating

is periodic, the wavelength of these propagating waves can be detected. Because the wavelength of these thermal waves depends on the frequency of the heating beam and on the thermal properties, the thermal conductivity parallel to the surface of the film can be obtained. The experimental results of their study are shown in Figure 2.12.

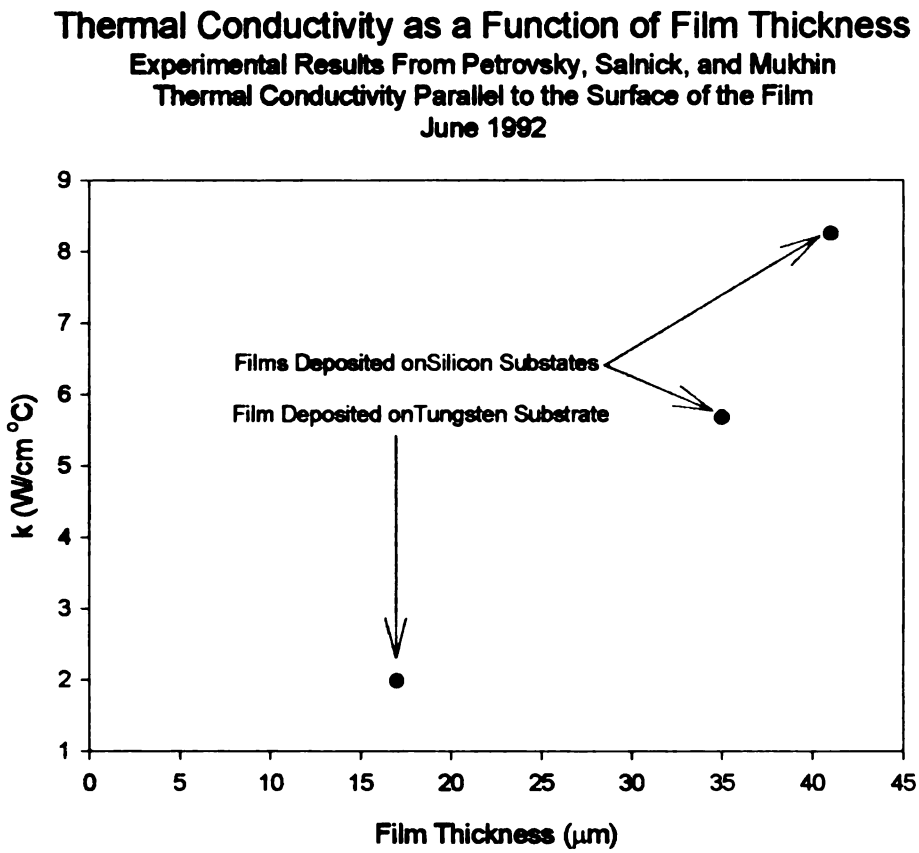

Figure 2.12. *Typical values for $k_{\parallel}$ obtained by Petrovsky, Salnick, Mukhin, and Spitsyn using the photothermal beam deflection technique.*

2.2.3 General Purpose System Development at Michigan State University

Although there have been several studies concerning the thermophysical properties of CVD diamond films, there seems to be a large discrepancy between the results of different research groups. This discrepancy can be illustrated by examining

Figure 2.13. The driving force behind this research is to develop a general purpose system capable of measuring the thermophysical properties of diamond films and other manufacturing materials. Particular attention in this research is paid to thin films.

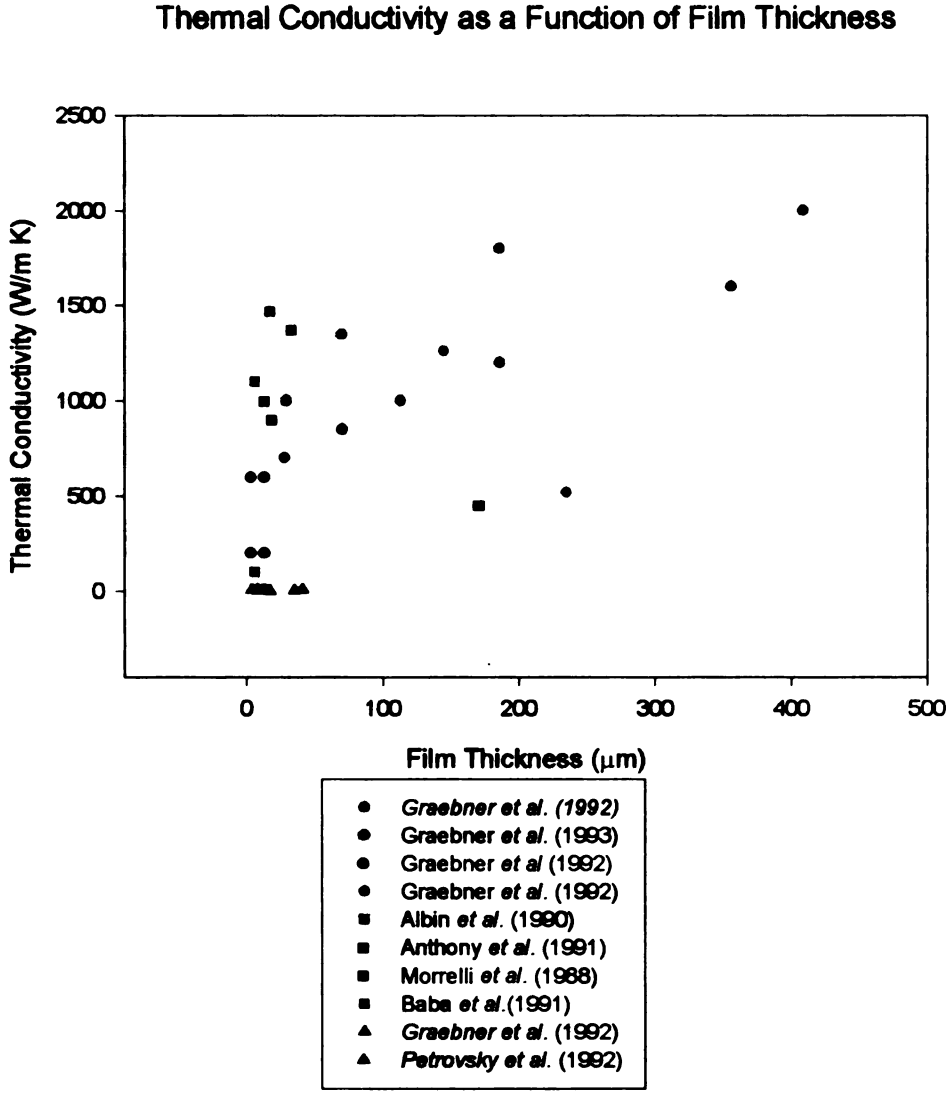

Figure 2.13. *A plot of the thermal conductivity as a function of film thickness. This plot illustrates the discrepancy in the estimated values among separate research groups.*

In this newly developed system, the experimental equipment was selected to provide flexibility and a non-contact and non-destructive means of heating and

temperature measurement. For example, a solid state Nd:YAG laser was selected as the heating source. This laser allows for variations in radiation intensity as well as spatial distribution and temporal deposition of energy. Two infrared temperature measurement systems were selected because of the challenge associated with the micro-structural size and fast thermal response of diamond films and other materials. Temperature measurement systems such as these eliminate some of the problems associated with surface instrumentation and provide a great deal of information in space and/or time.

In the following chapter, the experimental equipment comprising this newly developed system will be discussed and characterized. In the chapters to follow, the equipment is then used with existing analytical tools to determine the thermal diffusivity of circular specimens. In this study, the thermal diffusivity of three CVD diamond films with average thicknesses between 240μm and 370μm were measured. In order to validate the experimental techniques, high purity and thermally well defined copper and iron samples were also measured.

Chapter 3

System Development and Component Description

In the areas of inverse heat conduction and parameter estimation, it is imperative that experimental techniques are well understood. In general, most experimental techniques used in these areas involve three processes. First, a heat source is used to perturb the thermal equilibrium in the material of interest. Second, the phenomenon of conductive heat transfer attempts to restore thermal equilibrium by flowing heat down a temperature gradient. Third, the temperature gradients are measured, the heat source quantified, the data are analyzed based on a mathematical model, and the thermal properties are estimated.

In order to assure accuracy in such experiments, the equipment must be thoroughly characterized. As a result, this chapter is dedicated to a discussion of each of the

experimental components used in the development of this non-contact and non-destructive system capable of measuring the thermal properties of various materials.

In order to avoid confusion and to give the reader a brief introduction into the use of the experimental equipment, schematic representations of the overall system and two typical test configurations are displayed in Figures 3.1, 3.2 and 3.3 respectively.

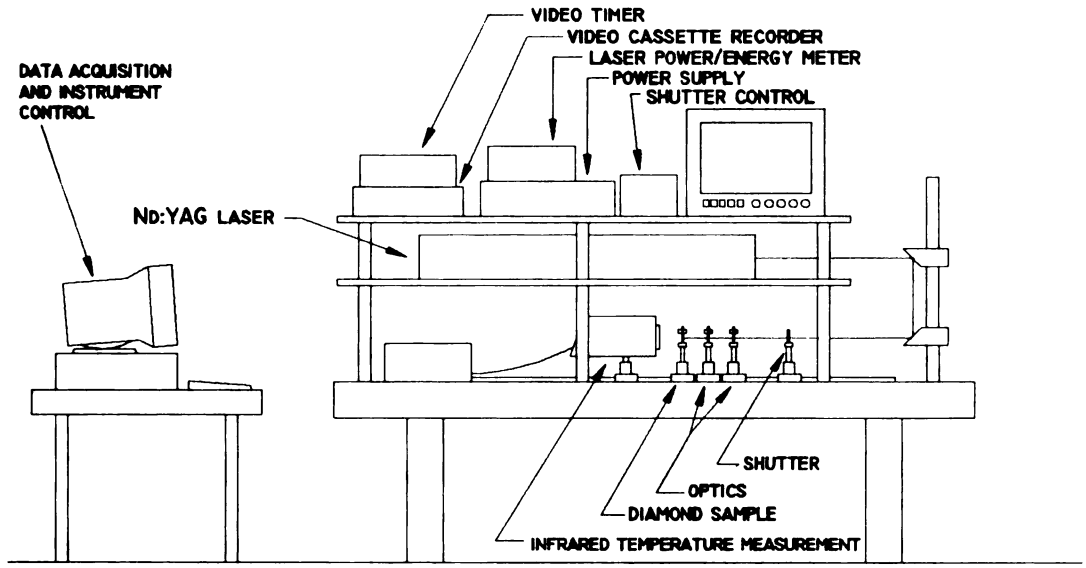

Figure 3.1. *A generalized schematic representation of the newly developed experimental setup.*

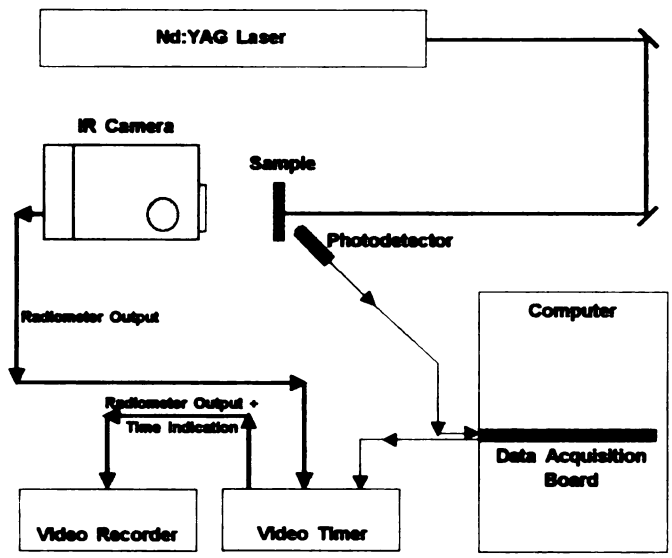

Figure 3.2. *A typical test configuration for measuring the thermal diffusivity parallel to the surface of the film.*

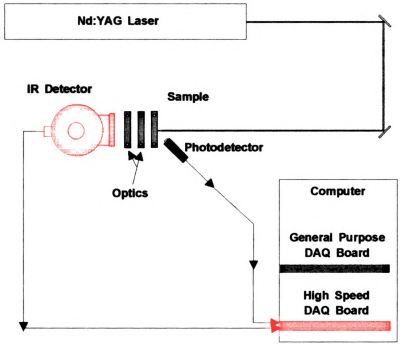

Figure 3.3. *A typical experimental configuration used to measure the thermal conductivity perpendicular to the surface of the film.*

In Figure 3.2, infrared thermography is used to record the transient temperature distributions along the surface as it is heated with the Nd:YAG laser. Since the output of the IR camera is a video signal, digital indications of time are superimposed and the data is recorded using a standard video timer and video cassette recorder. Since timing issues are important, a photodetector, with a response proportional to the intensity of light, is used to sense the presence of the laser. The response of the photodetector is monitored by a general purpose data acquisition board programmed using LabVIEW. Once the response of the photodetector increases beyond a preprogrammed trigger level, a TTL low signal is sent to the video timer and timing is initiated. Once the test is complete, the data are analyzed using a general purpose image processing system

In Figure 3.3, transient temperature measurements at one point on the back surface of the test sample are measured using an infrared detector. The data is collected

using a "fast data acquisition board" which has the ability to sample at 1MHz. Once again, the sample is energized using a Nd:YAG laser and the photodetector is used to sense the presence of the laser and initiate data collection.

3.1 Temperature Measurements

Experimentally, diamond films and other similar materials are very challenging to analyze thermally. Their microstructural size and rapid thermal response pose spatial and temporal problems for experimental techniques utilizing surface mounted temperature sensors such as thermocouples and resistive thermometers. In order to make surface temperature measurements with these devices, small voids are commonly machined into the sample for probe installation. The very presence of these probes, however, makes these techniques intrusive and can affect the thermal behavior. These probes generally have thermophysical properties different from those of the test specimen, and as a result their response would be different than that of the substrate. That is, these probes can act as a heat sink or source, thus measuring temperatures that would be significantly different than the temperatures that would have existed in the absence of the probes. For these reasons optical, non-contact infrared techniques were implemented for temperature acquisition [Puram, 1991].

Each of these infrared techniques obtain surface temperatures indirectly and rely on the simple premise that all real objects in the universe exist at temperatures above absolute zero. As a result, the atoms and molecules that compose the object are in motion. These motions are constrained by interactions with other atoms and molecules; therefore the elementary charges radiate electromagnetically. The magnitude of this

electromagnetic radiation increases with temperature and as a result the output of the infrared detector focused onto the surface of the sample increases. In the following subsections the two infrared temperature measurement systems used are discussed.

3.1.1 Infrared Imaging Radiometer

Infrared imaging provides a two-dimensional representation of surface temperature variations across the target and hence it is a global technique as opposed to thermocouples and resistance thermometers which only make point measurements. The technique is totally non-intrusive and because of its non-destructive nature, repetitive surface measurements are possible.

Infrared imagers sense temperature by detecting thermal radiation. Thermal radiation is the radiation emitted by an object due to its temperature and covers the 0.3 to 50 micrometer spectral range of the electromagnetic spectrum. In general, IR imagers are available in the 2 to 5 or 8 to 12 micrometer range of the spectrum. The major components of IR imaging system include a geranium optical lens system, a scanning mechanism, a detector, an electronic signal processing unit, a control unit and a display device.

The thermal radiation entering the scanner through a germanium window is deflected by the horizontal and vertical scanning mirrors and is focused on a HgCdTe detector. Motorized focus and zoom mechanisms are operated within the scanner by remote control. With the HgCdTe detector cooled by liquid nitrogen to approximately 77 K, detector noise is reduced and the maximum thermal sensitivity is obtained.

The low-level signal generated by the HgCdTe detector is processed, digitized, reformatted and prepared for visual display by the video processor within control unit. The result is a monochrome video signal which can be stored on a video cassette recorder. The signal can also be processed on a image processing system to digitize the video signal, calculate and display target absolute temperatures, pseudo-color thermal images, and apply image enhancement features.

In the development of this system, transient surface temperature measurements were made utilizing an Inframetrics Model 600L infrared imaging radiometer in conjunction with an image processing system. The infrared system, shown in Figure 3.4, allows for real-time thermal imaging of static and dynamic thermal events with user defined amounts of imaging averaging, temperature ranges, emissivity settings and fields of view.

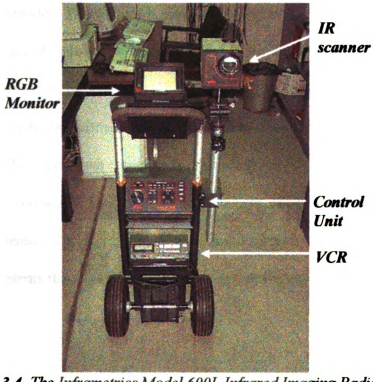

Figure 3.4. *The Inframetrics Model 600L Infrared Imaging Radiometer.*

Temporal Resolution:

The infrared scanner incorporates two independent electromechanical servos (galvanometers) which perform horizontal and vertical scanning. Attached to these servos are scanning mirrors contained in a sealed, evacuated module for increased efficiency. The scanning rate of these mirrors controls the temporal resolution of the system. Horizontal scanning is performed at the very high rate of 7866 Hz in a resonant sinusoidal mode. Vertical scanning is performed in a sawtooth pattern at 60 Hz. These scanning frequencies produce an output consistent with a standard interlaced television format. As a result, in the normal operating mode infrared images of the radiometer's entire field of view can be captured at 30 Hz.

The radiometer is also equipped with a high speed measurement mode known as the fast line scan mode. This feature is designed to capture thermal events along a line with a sampling rate of 7866 Hz. When configured in the fast line scan mode, the vertical scanning galvanometer is stopped near the center of the radiometer's field of view. This allows the horizontal galvanometer to scan the same line continuously. The video processor within the control unit operates in it's normal mode and continues to produce a standard format video signal. The image output, however, appears different, in that it is no longer a two-dimensional image. Instead, each line displayed from top to bottom on the video image represents the same line in space, but at a different point in time.

Temperature Resolution:

The output of the infrared imaging system is a video format with 8 bits of temperature resolution.. The radiometer offers several temperature ranges which control the temperature resolution. When operated in the smallest possible temperature span (5°C), a maximum thermal resolution of 0.03°C is obtained.

Spatial Resolution:

The spatial resolution is a measure of the thermal imaging system's ability to detect and accurately measure the temperature of small objects. An ideal thermal imager would measure the true temperature even when it looks at an object which is very small compared to the whole image. However, for a practical scanner, when the image of a small object projected on the detector surface becomes smaller than the detector, the detector will measure a combination of both the object and its background. Consequently the measured temperature for a very small object is affected by its size. One would think that is would be enough to make sure that the ideally projected image of the object is large enough to fill the whole detector. But the image of the detector is blurred by the optics. Also the detector has a response time that affects the output for small objects.

One way to measure the spatial resolution is by placing a variable slit in front of a large uniform blackbody radiator and to measure the modulation of the output signal as a function of slit width (The Slit Response Function or SRF). The imaging spatial resolution is normally specified by the manufacturer at a slit width that gives a 50% of full modulation response. The 50% SRF value indicates the size of a small object which can be resolved in the image. However, when it comes to temperature measurement a

modulation of 50% is not sufficient. The measurement spatial resolution is defined at a slit width which yields a response which is 95% of full modulation [Halmsten, 1991]

A specialized variable width slit has been created. The width of this slit is controlled using a micro-positioner with a resolution of 1μm. A spatially uniform blackbody heat source is viewed through the slit and used to create a measurable temperature difference.

The radiometer was carefully focused on the jaws of the slit. The best focus is assumed to occur when the edges of the slit become sharp and the maximum throughput from the blackbody simulator is obtained. As the slit width was increased the output of the radiometer was stored on a video cassette recorder. After the jaws of the slit were open to the point where 100% of the radiosity from the blackbody was measured, the test was concluded and the stored data was processed using IPPLUS.

Three SRF tests have been completed. Two tests have been done with a combination of the 3X and close-up lenses. Another test has been completed with no external optics. The test results are shown in Figure 3.5 and Figure 3.6. The imaging spatial resolution (IRS) of the system with the 3X and close-up lenses for both tests is approximately 20μm and the temperature measurement spatial resolution (TMRS) is approximately 67.5μm. These results compare well with the technical specifications given by Inframetrics which state that the TMRS of the system is 100 μm. The IRS for the radiometer with no external optics and with a working distance of 15 cm is 65 μm and the TMRS is 335 μm.

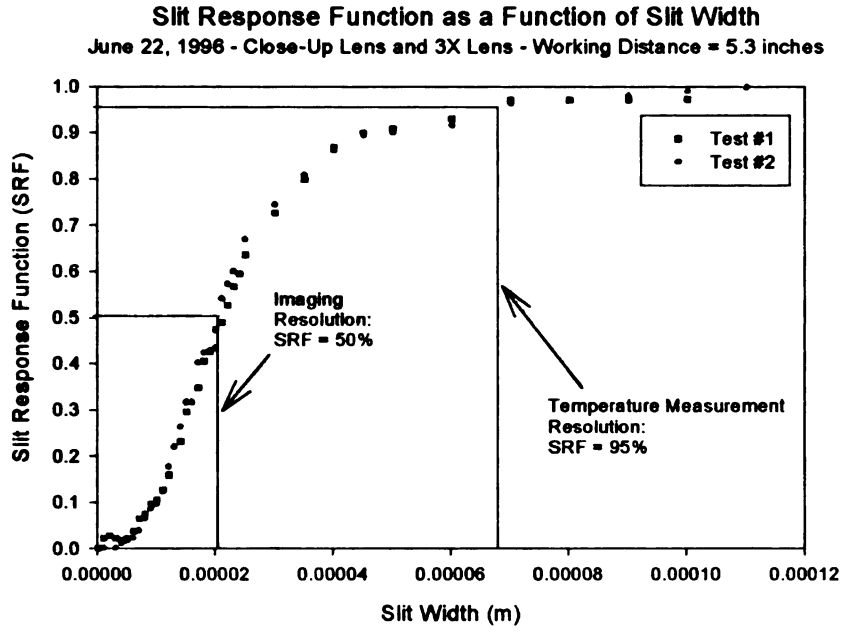

Figure 3.5. *The slit response function for the Inframetrics Radiometer with the Close-up and 3X lenses. These tests show that the imaging spatial resolution is approximately 20 μm and the measurement spatial resolution is approximately 67.5 μm.*

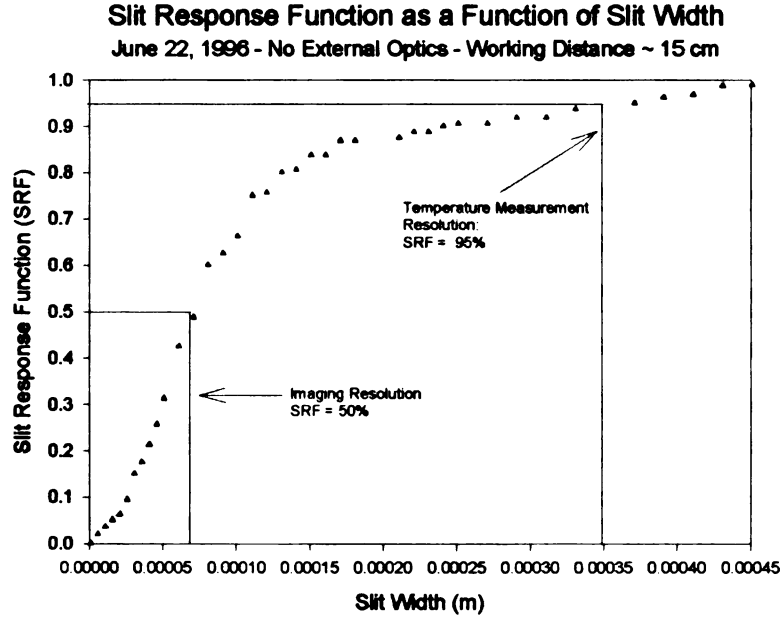

Figure 3.6. *The slit response function for the Inframetrics Radiometer with no external optics. This tests illustrates that at a working distance of 15 cm the imaging spatial resolution is approximately 65 μm and the measurement spatial resolution is approximately 335 μm.*

The simplest way to decrease the measurement errors due to small sized objects is to decrease the distance between the object and the radiometer. This is illustrated by the increase in spatial resolution that occurred due to the addition of external optics. A feature that might seem helpful is the ZOOM function of the radiometer. The zoom function decreases the amplitude of the scanning mirrors which only makes the field of view smaller. However, the instantaneous field of view and the slit response function remain the same as the optical magnification is not changed. Therefore, the zoom function does not improve the spatial resolution.

Image Processing System:

The radiometer dissects the field of view such that the thermal images produced consist 365 horizontal and 280 vertical datum points. Therefore, in each thermal image over 100,000 surface temperature measurement are made. The Image Pro Plus (IPPLUS) image processing system is primarily used to capture and store thermal patterns and access temperatures corresponding to any or all digitized picture elements (pixels) which make up the thermal field.

Temperature measurements are based on the gray scale intensity of each pixel. The temperatures are calculated based on a calibration curve similar to that shown in Figure 3.7. Since the output of the radiometer is an 8 bit format, the digitized gray scale values will range from 0 to 255. Therefore, the temperature range of the radiometer is

broken up into 256 gray discrete gray levels. A detailed discussion of this calibration can be found in Appendix B.

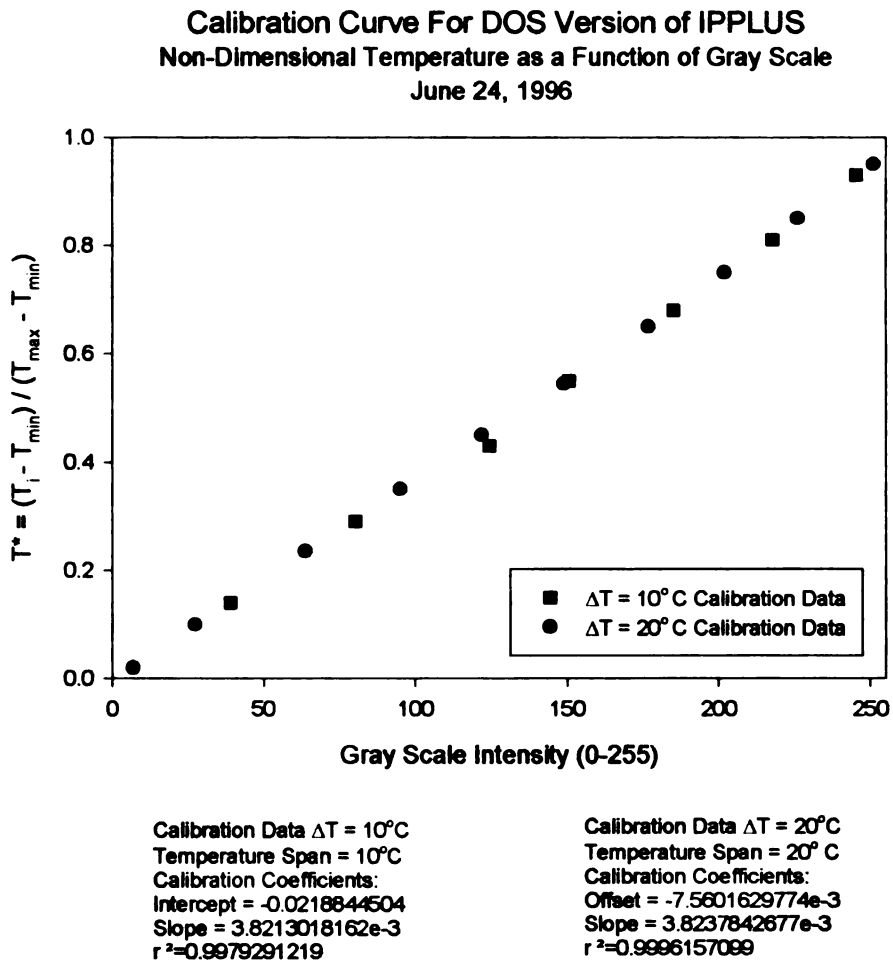

Figure 3.7. *A plot of the non-dimensional temperature as a function of gray scale. This information is used to generate a calibration between gray scale and temperature.*

3.1.2 The EG&G Model J15D12 Infrared Point Detector

The EG&G Mercury Cadmium Telluride (HgCdTe) Model J15D12 point detector, shown in Figure 3.8, can also be used in temperature acquisition. The characteristic time of this device is .5 μsec. As a result of this rapid response, temperature measurements of

one point can be made at 2 MHz. This detector is designed for operation in the 2 to 12 μm wavelength region with a peak response at 11μm.

This photoconductive detector is mounted on a metal dewar and operated at 77 K. The actual detector is comprised of a thin layer (~ 10 to 20 μm) of HgCdTe with metalized contact pads defining the active area. Incident photons with energy greater than the semiconductor band-gap energy, excite electrons into the conduction band, thereby increasing the conductivity of the material [Dereniak and Crowe, 1993].

In order to sense the change in resistivity, a constant bias current is applied across the 0.25mm square detector. The bias current is produced with either a low noise power supply or a 15 volt battery applied across a resistor. As a result of this constant current, the changes in detector resistance cause voltages fluctuations which are applied by the PA-350 preamplifier.

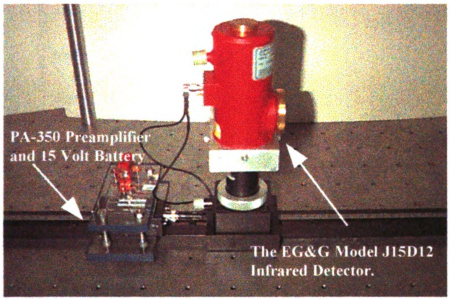

Figure 3.8. *The EG&G Model J15D12 Infrared Detector and PA-350 Preamplifier.*

Initial tests have been completed using this temperature measurement system. The output of PA-350 preamplifier can be displayed on a volt meter or acquired and collected

with a data acquisition system. Prior to such tests, a calibration must be done to find a relationship between the detector's output and the surface temperature. In order to do so, a resistive heater was attached to a aluminum disk. A thermocouple is mounted to the disk for temperature measurements and a thin layer of black paint was added to improve the surface emissivity. The radiation from this disk is focused onto the detector element using two plano-convex lenses. As the power across the heater was gradually increased, the response of thermocouple and infrared detector were recorded simultaneously. The relationship between the response of detector and thermocouple is shown in Figure 3.9.

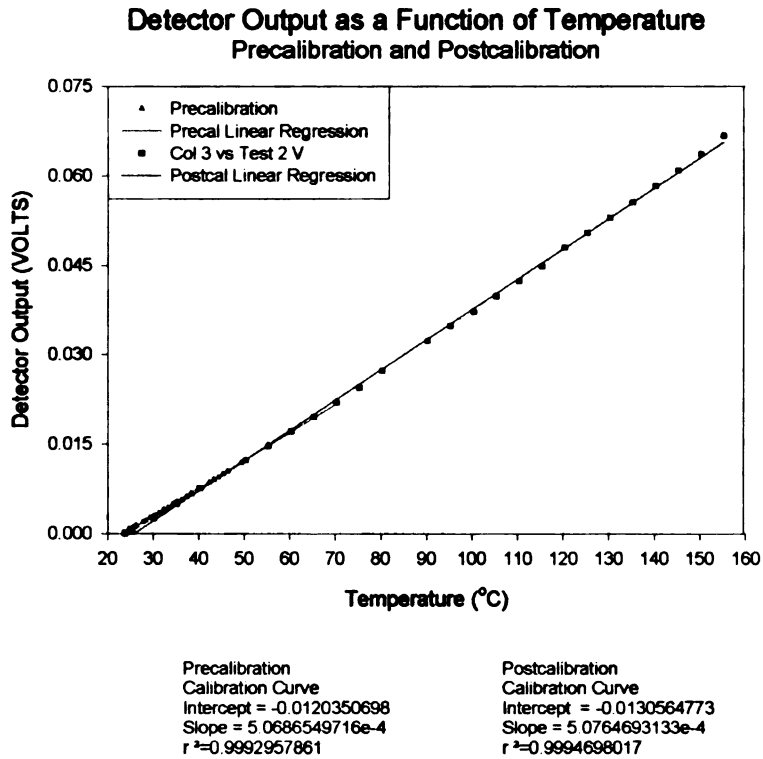

Figure 3.9. *The comparison between response of the EG&G Infrared Detector and temperature measured by the thermocouple.*

Also shown in Figure 3.9, the detector has a linear response to increases in temperature. With knowledge of the response, transient temperature measurements along a surface can be acquired. In this case a round aluminum sample with a diameter 635 mm and a thickness of 100 μm was energized with a Nd:YAG laser. Data was acquired at 10 kHz using a general purpose data acquisition board. The acquisition of data was initiated when the response of a photodetector exceeded a software programmed trigger level. A photograph and a schematic representation of the experimental setup are shown in Figure 3.10. A plot of the typical experimental results are shown in Figure 3.11.

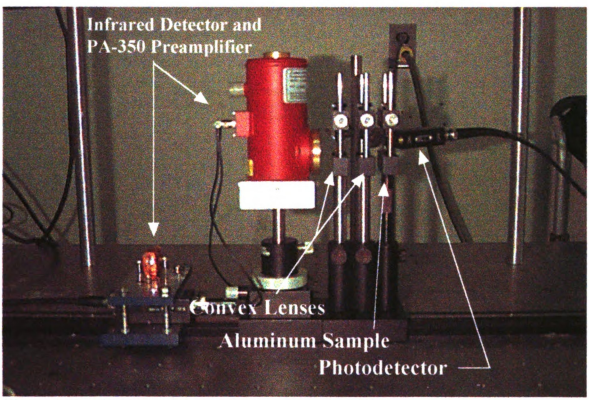

Figure 3.10a. *A picture of the experimental setup used for transient temperature surface measurement*

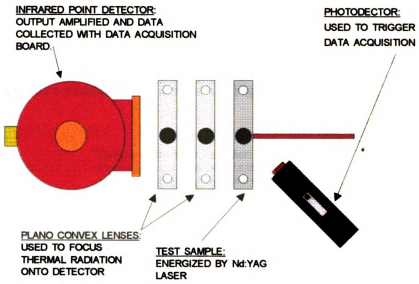

Figure 3.10b. *A schematic representation of the experimental setup used for transient surface measurement.*

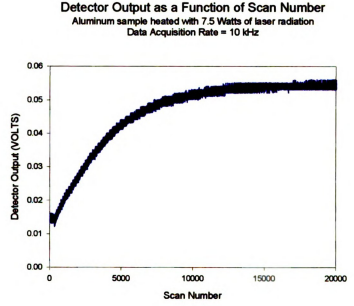

Figure 3.11. *The output of the photodetector as a function of scan number. Since data was collected at 10 kHz, the information in the above plot represents 2 seconds of heating.*

If the calibration data from Figure 3.9 is considered, the voltage output from the detector can be related to the transient temperature measurements. A plot of these transient temperature measurements is shown in Figure 3.12.

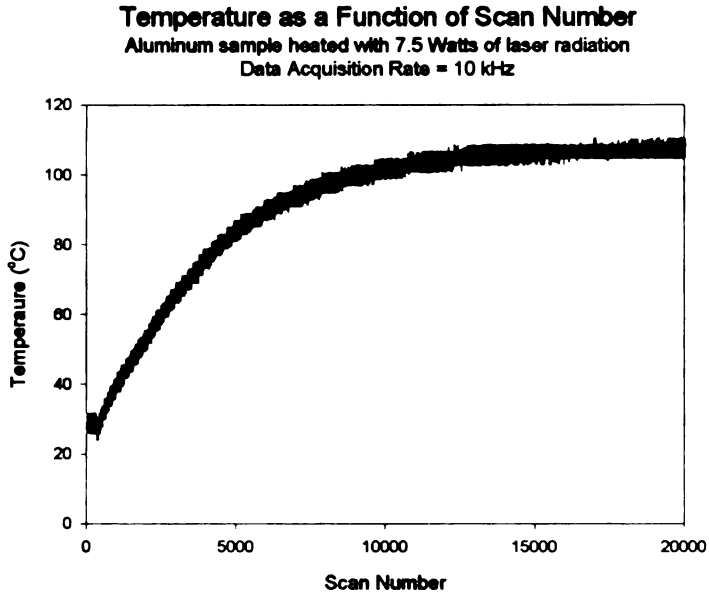

Figure 3.12. *Temperature as a function of scan number. This data was obtained using the voltage to temperature calibration in Figure 3.9.*

3.2 Heating Source

Many types of heat sources are used by researchers interested in thermophysical property estimation in order to perturb the thermal equilibrium of the test specimen. For example, Graebner used resistive heaters in his study of the thermal conductivity parallel to the surface of the film [Graebner, 1992]. These heaters are easy to use and well characterized, but are limited because they do not offer much mechanical flexibility and must be in direct contact with the test specimen. In this study a non-contact heat source offering variability in the distribution of radiation spatially and with time was applied. The

following subsections describe this heating source and some of the instrumentation used to quantify its characteristics.

3.2.1 Excel/Quantronix Model 117E Nd:YAG Laser

As illustrated in the background review portion of Chapter 2 various types of lasers are currently being used by many researchers interested in thermophysical property estimation. The unique properties of laser make them very attractive. Along with their exceptional monochromatic behavior and small amount of beam divergence, in most cases lasers have the ability to deliver large amounts of power in a variety of spatial distributions and with various temporal characteristics. For a more complete discussion pertaining to some of the general properties of laser light, please see Appendix A.

In the development of this general purpose thermophysical property estimation system the Excel/Quantronix Model 117E Nd:YAG laser, shown in Figure 3.13, was chosen as the primary heating source. The flexibility of operational modes offered by this type of laser was a significant reason for its selection. Without the use of external optics this laser produces a beam diameter of approximately 0.7 mm and has the ability to deliver over 15.5 Watts of laser radiation to the surface of a variety of test samples. This large amount of power carried in such a small beam diameter produces a very large power density ($4kW/cm^2$) and may not be desired in all situations. Several techniques can be implemented to reduce the beam intensity.

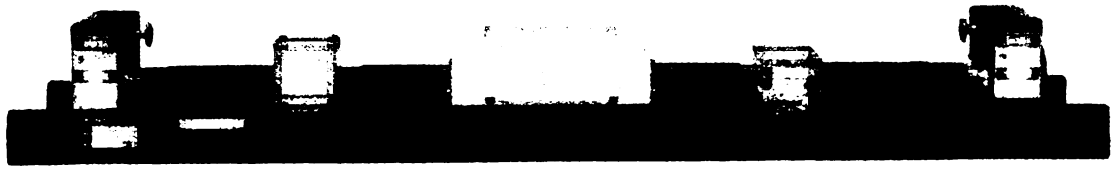

Figure 3.13. Excel/Quantronix Model 117E Nd:YAG laser

One of the simplest methods for reducing the beams intensity is to lower the pumping power of the laser. Although the laser power can be reduced significantly using this approach the beam quality is reduced at lower current levels. For example, with the lamp current at 28.8 amps the thermal axis of the Nd:YAG Laser rod is aligned with mirrors to produce a beam with a Gaussian Distribution (a laser operating in such a manner is often said to be operating in its TEM_{oo} mode). When the lamp current is reduced thermal changes within the lamp housing affect the thermal axis producing a beam of inferior quality. A beam of poor quality may be unstable or have cavities or high order modes within the beam profile. This variation in beam intensity and beam quality as a function of lamp current is illustrated in Figure 3.14.

The data in Figure 3.14(a.) was measured using the Molectron Power/Energy meter. In this case, the laser's power was measured as the lamp current was varied. In Figures 3.14(b.) and 3.14(c.) the beam profile was obtained using a CCD camera in conjunction with the Image Pro Plus (IPPLUS) image processing system. Figure 3.14 (b.) is a characteristic representation of the beam profile when operating the laser with a lamp current near 28.8 amps. At this current the thermal axis of laser is aligned with the mirrors and aperture in such a manner that high quality gaussian shaped beam is established. When the lamp current is significantly reduced or increased from 28.8 amps,

thermal changes within the lamp housing cause the laser's thermal axis to be misaligned. Under these conditions, cavities or modes are developed in the beam profile as illustrated in Figure 3.14(c.).

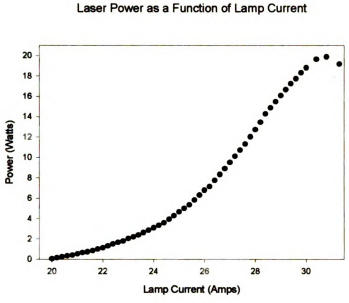

(a.)

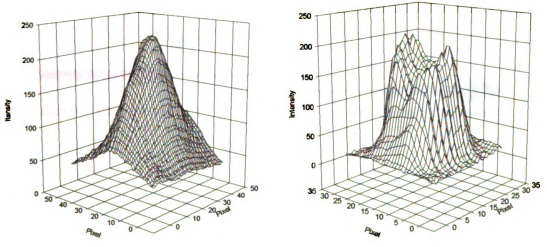

(b.) (c.)

Figure 3.14. *(a.) Laser power as a function of lamp current. (b.) A characteristic representation of the beam profile when operating the laser near 28.8 amps. At this current the thermal axis of the laser is aligned with the mirrors and aperture in such a manner that a high quality gaussian shaped beam is established. (c.) A characteristic representation of the beam profile with the laser's thermal axis misaligned. This distortion in beam quality occurs when operating the laser at low lamp currents.*

Beamsplitters and partial reflectors provide another means for reducing the laser beam intensity. Another method the laser intensity can be reduced is through the use of partial reflectors or beamsplitters. These front surface reflectors, shown in Figure 3.15, offer major reductions in beam intensity and surface qualities that will not significantly distort the beam's intensity profile. These beamsplitters are wavelength (1.064 μm) and polarization (s-polarized) sensitive, When orientated at a 45° angle with respect to the incoming laser, 50% of the beam is reflected and the remaining 50% is transmitted.

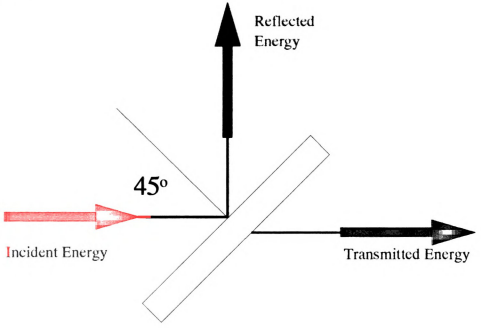

Figure 3.15. *The required alignment of the beamsplitters to obtain a 50% reduction in laser beam intensity.*

The beam's power density can also be reduced or increased by remapping the beam's spatial distribution. This is easily done through the use of external optics. For example, Plano-convex and Plano-concave lenses can be used to create an optical system often called a Galilean Beam expander. As illustrated in Figure 3.16 a plano-concave lens

with a focal length of 25.4mm is used to bend the parallel input rays of the laser away from the optical axis so that they diverge away from one another. At the opposite end a Plano-convex lens with a focal length of 200mm is used to collimate and straighten the diverging rays. When orientated in such a manner, this optical system produces a beam that is magnified 8 times and the power density is reduced 64 times.

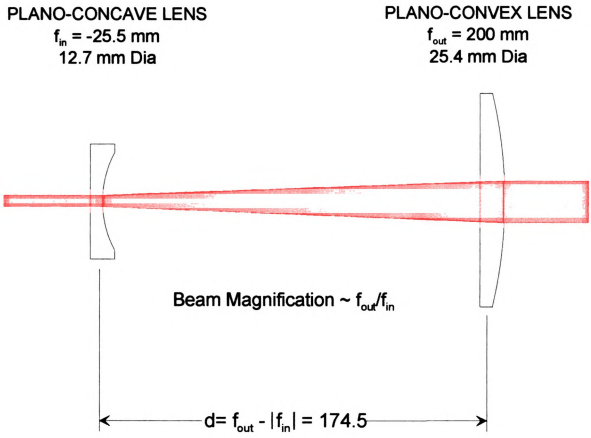

Figure 3.16. *The Galilean Beam Expander. Used in this case to magnify the laser beam's diameter 8 times.*

The addition of a Plano-convex cylindrical lens to the end of the optical train pictured in Figure 3.16 provides another example of how the laser radiation can be redistributed. Depending on the orientation of this lens a horizontal or vertical line is

created at the focal length of the lens. Initial tests with this optical system illustrate that the distribution across the length of this line is relatively constant. In Figure 3.17 a glass test specimen with approximate lateral dimensions of 50.8 mm x 12.70 mm x 1.5875 mm is heated along one edge with the laser passing through this optical system. A short time after heating is initiated (~1 to 2 seconds) several temperature distributions parallel to the heated surface are acquired using the output infrared radiometer. If the distribution of radiation along the generated line is constant the surface temperatures along lines parallel to heated surface would be constant. As shown in Figure 3.18 this is indeed the case.

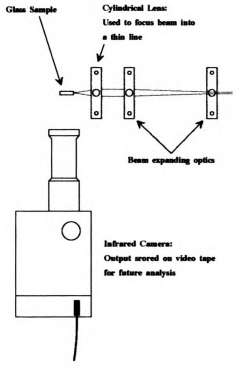

(a.)

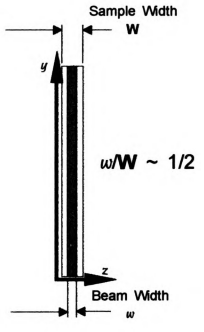

(b.)

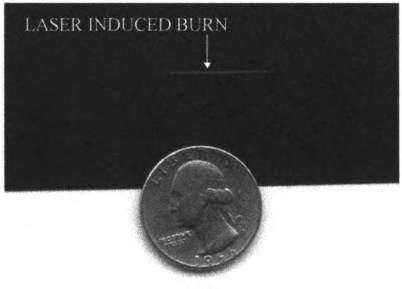

(c.)

Figure 3.17. *(a.)The heating of a test specimen with laser passing through a beam expander and a cylindrical lens. Temperature measurements are made using the Inframetrics Model 600L infrared imaging radiometer. (b.) A schematic representation comparing the sample thickness with the approximate beam thickness. (c.) Thermally sensitive laser paper manufactured by KENTIX used to give a general illustration of the size line generated with this optical configuration.*

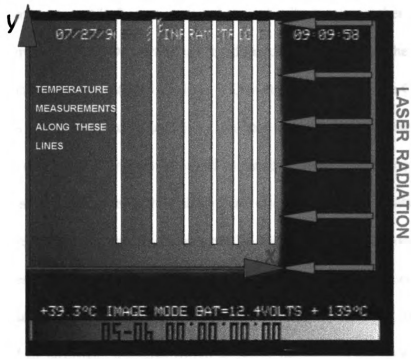

(a.)

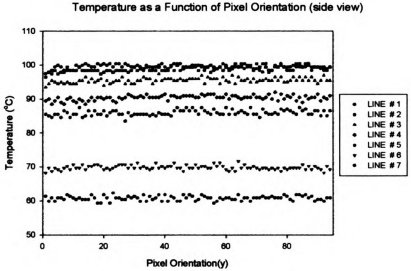

(b.)

Figure 3.18. *(a.) The surface temperature distribution of the test specimen heated along one surface with laser radiation spatially distributed as a line. If the radiation intensity across the length of the line generated is uniform, the surface temperatures parallel to the heated surface should be relatively constant. As shown in (b.) this is indeed the case.*

The variations possible for temporal radiation distribution is another advantage of the Excel/Quantronix laser. Depending on the desired type of heating the laser can be operated in a continuous wave (CW) mode or a Q-switched mode. In the CW mode the laser's output is very stable and its instability has been measured at less than 5% RMS. This CW beam can be mechanically chopped at various frequencies using an external shutter like that shown in Figure 3.19. This Uniblitz electro-mechanical shutter and driver can operate at frequencies up to 100 Hz and can be controlled externally with a standard TTL signal. These signals have been generated with both a function generator and the programmable data acquisition board capable of analog output. The use of this shutter system is limited by electrical problems within the drive mechanism and as a result of the low damage threshold of the shutter.

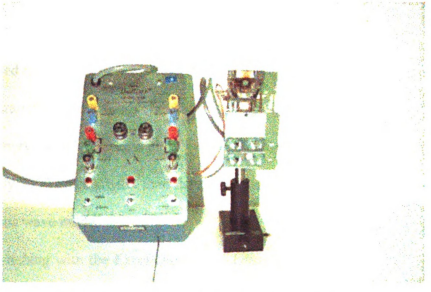

Figure 3.19. *The Uniblitz electro-mechanical shutter and control driver. This shutter system provides a means for mechanically chopping the beam at various frequencies.*

The Q-switched mode offers a very powerful method for controlling the laser intensity with time. Q-switching is a technique for obtaining short, intense bursts of radiation from lasers. In order to understand Q-switching a "Q factor" must be introduced to describe the properties of laser cavity. This Q factor characterizes the ability of the cavity to store radiant energy. A high value of Q means that energy is stored well within the cavity. A low value of Q means that energy present in the cavity will emerge rapidly. For example, if the output mirror in the cavity is highly reflective, Q will be relatively high; if the mirrors are of lower reflectivity, whatever energy is present in the cavity will emerge rapidly through the mirrors, and Q will be low [Ready, 1987].

Consider a situation when the Q factor is high. During this period, lasing action is not permitted and the arc lamp continues to pump optical energy to the laser rod. The laser rod absorbs this optical energy and stores it much like a capacitor stores electrical energy. When the Q-factor is switched to a lower value the stored energy within the rod will be emitted in the form of a short pulse. Depending on the operating conditions of the laser, the duration of the pulse is typically in the 50-500 nanosecond range. Since a large amount of energy is released in a short period of time, the peak power of each pulse is approximately 3000 times greater than the power generated by the laser when operating in the continuous wave mode.

Q-switching with the Excel/Quantronix Laser is controlled by the Model 391 RF (Repetition Frequency) Driver. The Electro-optic Q-switch acts like a high speed shutter within the laser resonator and is used to control the beam emission. The built-in trigger provides operation at Q-switch repetition rates between 100 Hz and 80 kHz. In Figure 3.20 time trace was recorded using the photodetector to illustrate the small bursts of

energy generated by the Q-switch driver operating at 50 kHz. In Figure 3.21 the peak power, pulse width, pulse energy, and average power of these small bursts of energy are quantified in a series of performance curves. The data in Figure 3.20 was measured with a high speed photodetector and the output was displayed on an oscilloscope. The performance curves in Figure 3.21 were measured with the Molectron Power/Energy meter and the high speed photodetector.

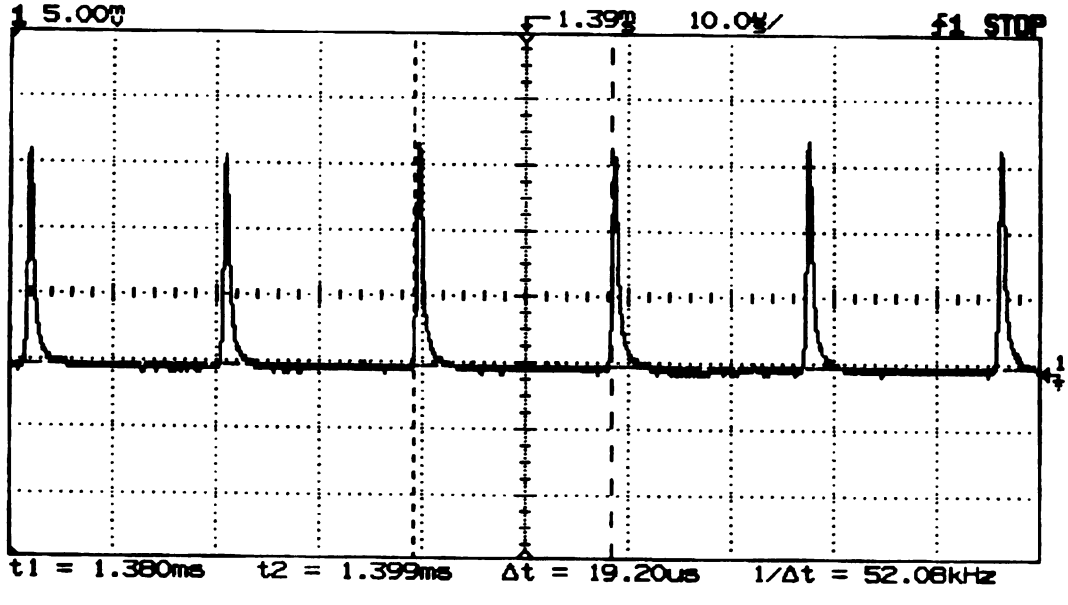

Figure 3.20. *Beam intensity as a function of time for the laser operating in a Q-switch mode with a pulse repetition frequency of 50kHz. This information is acquired with a high speed photodetector with output connected to an oscilloscope.*

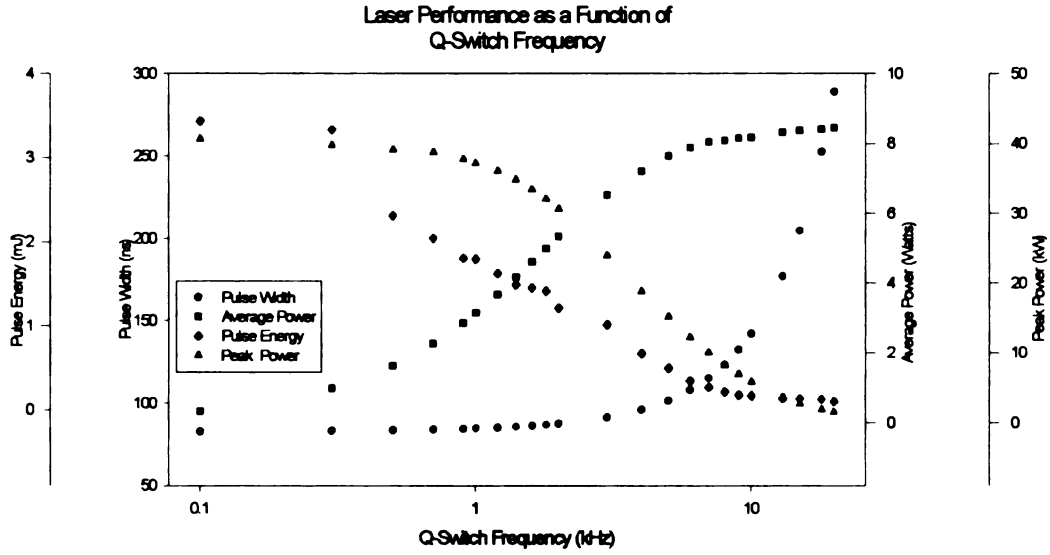

Figure 3.21. *Typical performance curves for the Excel/Quantronix Nd:YAG laser operating with a lamp current of 28.0 amps. This information was acquired with a power/energy and photodector and is meant to represent typical laser performance when operating in Q-switch mode.*

3.2.2 Laser Diagnostic Equipment

Laser beam diagnostics include measurement of energy/power, intensity/beam profile, temporal/time dependence and measurements of beam diameter. These measurements provide a complete understanding of the characteristics of the laser beam and become important when attempting to optimize the laser for a particular application. In the following subsections some of the initial steps towards developing these measurement techniques are discussed. For a more thorough discussion the reader is urged to read Appendix D.

3.2.2.1 Molectron Power/Energy Meter

The microprocessor based EMP1000, shown in Figure 3.22, is a NIST calibrated, single channel instrument capable of measuring energy, power, voltage, and frequency. It

is designed to measure the output of both pulsed and continuous-wave (CW) lasers and it will operate with a variety of power and energy probes.

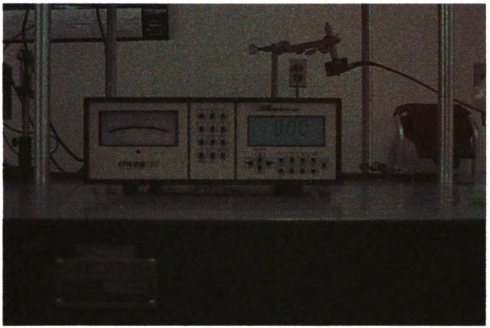

Figure 3.22. *The Molectron EPM1000 Power/Energy Meter*

Two types of probes

A PowerMax thermopile probe, model NO. PM10 shown in Figure 3.23, is used to measure voltage and power. The thermopile probe has an absorber disk deposited on a ring of thermocouples. Incident radiation from the laser being tested heats a spot on the disk, creating a temperature gradient between this region and the edge of the disk; heat sinks maintain the edge of the disk at ambient temperature. The thermocouples convert

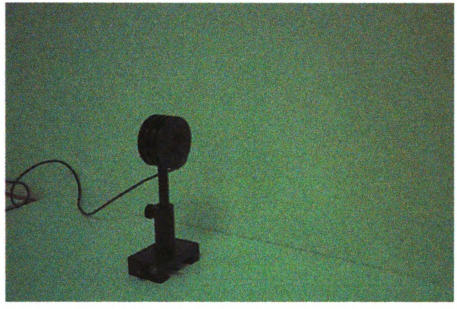

Figure 3.23. *The Molectron PowerMAX PM-10 thermopile probe. Thermopile probes of this kind are primarily used to measure the output of moderate to high power continuous wave (CW) lasers.*

the temperature gradient into an electronic signal that is then read by the meter. This device is best suited for making steady-state measurements and is used to measure primarily the output of moderate- to high power CW lasers throughout the ultraviolet and infrared spectrum.

A pryoelectric probe, model NO. J25-112 shown in Figure 3.24, can be used to make measurements of energy, power, volts and frequency. This detector uses a crystal with a permanent electronic polarization. As the crystal undergoes a

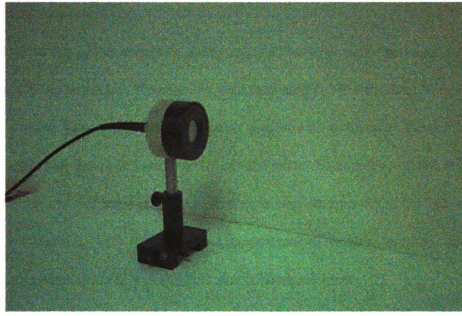

Figure 3.24. *The Molectron pyroelectronic probe. Pyroelectronic probes of this kind are primarily used to measure the output of moderate to high power q-switched or externally chopped lasers.*

temperature change, the electronic polarization changes, generating a transient current that is read by the EPM1000. The current is produced only when the temperature is changing; once equilibrium is reached, no further current is produced. Consequentially, this detector can only measure beams that inherently change with time. Such lasers include pulsed lasers or artificially pulsed (chopped) CW lasers.

Pyroelectric detectors can be used with low- to high- energy pulsed lasers over the entire UV and IR spectral range. Because the response speed of pyroelectric detectors is slow as compared to the pulse length of most lasers, this type of detector is not useful for performing highly accurate characterization of laser pulse shape. It is, however, quite accurate for determining integrated pulse energy and peak power.

Measurement Errors

Both of the probes translate energy into an electrical signal and each has different factors that affect accuracy, repeatability, and traceability. The thermopile meter detects heat. As a result, any source of heat , whether it results from the beam being measured, or the heat generated from the background, can influence the accuracy of the measurement process. Errors can occur if there are extraneous heat sources in the field of view of the detector, if something directly changes the temperature of the measurement head itself, or if something affects the ability of the heat sink to dissipate heat.

The human body typically radiates about 100 Watts of power, which is well within the measurement capabilities of the detector. Therefore a body or hand in the field of view of the detector during measurement can influence the results. Peripheral electronic equipment, such as power supplies or oscilloscopes are sources of heat and are often present on the optic table. They should be removed from the field of view of the sensor head. If need be however, the contribution of constant heat sources can be calculated and removed from the instrument readings.

The sensor head should not be subjected to outside heat sources that could affect the temperature differential between the beam and the heat sink. For example, a hand placed on the sensor housing can influence measurements. Placing the measurement head on the cool optical table and putting it back in place for measurement before it has had a chance to equilibrate can also introduce errors

Location of the beam on the detector can have a significant effect on the measurement results. To achieve accuracy and repeatability to better than a fraction of a

percent, it is necessary to center the beam on the detector surface. Aligning the beam in this manner allows for the most even flow through the device.

For pyroelectric detectors, the most common source of error is damage to the detector. Once the device has been damaged, it can no longer be relied on for accurate temperature measurements. Under normal operating conditions the beam produced from the Excel/Quantronix Model 117E Nd:YAG laser does not exceed the damage threshold of the energy meter. Optics can used to focus the beam to a diameter as small as its transverse wavelength. When operating in this mode the power density increases and damage to the detector can result.

Example Measurements

As stated earlier the PowerMax thermopile detector is best suited for measurement of CW lasers while the pyroelectronic detector can be used to measured Q-switched and pulsed lasers. There are two separate electrical connections between the sensor heads and EPM1000. The thermopile detector is connected to the 25 pin "smart probe connector" and the pyroelectronic detector is connected to a BNC connector labeled "pulse in." The EPM1000 automatically senses which of the two probes is present during power up. For example, if the thermopile is connected to the smart probe connection during the power up cycle the EPM1000 is ready to display output in voltage or power of a CW laser.

Some of the basic tests that have been conducted as part of this thesis included measuring the power output as a function of lamp current and the characteristic performance curves as shown previously in Figure 3.14 and Figure 3.21 respectively. In

conducting these tests the beam is aligned such that it strikes the center absorber disk and the operating conditions of the laser are varied. The output of the probes at various currents and Q-switch frequencies can be recorded manually or with an external computer using the BNC output connection or the RS-232 serial port on the back panel of the EPM1000.

In order to take advantage of the output features of the EPM1000 a data acquisition and control program was written using LabVIEW. This program, shown in Figure 3.25, gives the user a choice of computer interface options. If the BNC OUTPUT button is selected the program acts simply as a data acquisition program. The output of the EPM1000 ranges between 0 and 2 VDC and is updated at a rate of 3 Hz. In this case, the meaning of this output depends on the configuration of the EPM1000. For example, if the EPM1000 is configured to measure power in the range of 0 to 30 Watts, a one volt signal from the BNC OUTPUT corresponds to a laser power of 15 Watts. If the operating configuration of the meter matches the conditions on the front panel of the LabVIEW program, the program will automatically convert the response to match the true meaning of the detector's output.

If higher data acquisition rates are desired, the SERIAL communication switch on the LabVIEW program should be depressed before the program is activated. In this case, a 9 pin serial cable is connected from the back panel of the EPM1000 to the serial port residing in the host Gateway 486-66 computer. Operating the LabVIEW program with the RS-232 connection gives the user complete control of front panel options from a remote location, allows for variations in the communication parameters(such as baud rate and output format), and allows for the data to be updated at a relatively high rate of 100 Hz.

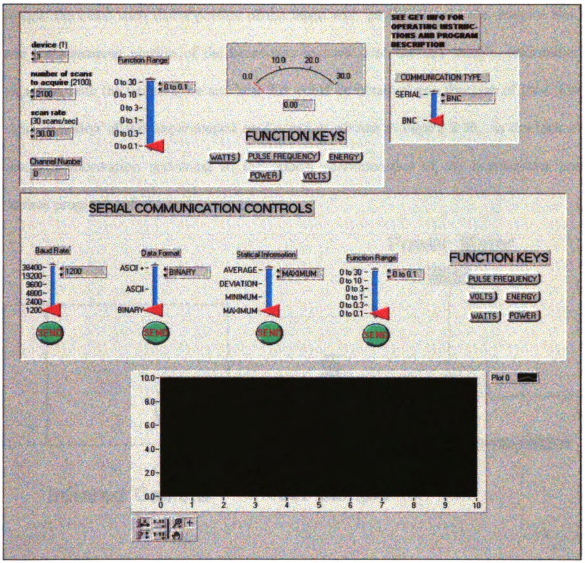

Figure 3.25 *LabVIEW Data Acquisition and Control program for EPM1000 Power/Energy Meter. This program allows for communication through an analog BNC connection or through a RS-232 Serial Port.*

This program was developed to provide a means for acquiring information about the laser's performance. For example, this program could be used to monitor the stability of the laser over a given period of time. The program could also be used to monitor the laser's power as it was being used to heat a surface. In this case, if a beamsplitter was used

to split the beam such that a portion of the beam was projected onto the detector head and the remaining portion of the beam was focused onto the test sample, information regarding both the temperature and heat flux could be obtained as a function of time. The main limitation of this experimental configuration, shown in Figure 3.26, is the lack of accurate information pertaining to the optical characteristics of the beamsplitter and surface properties of the test specimen.

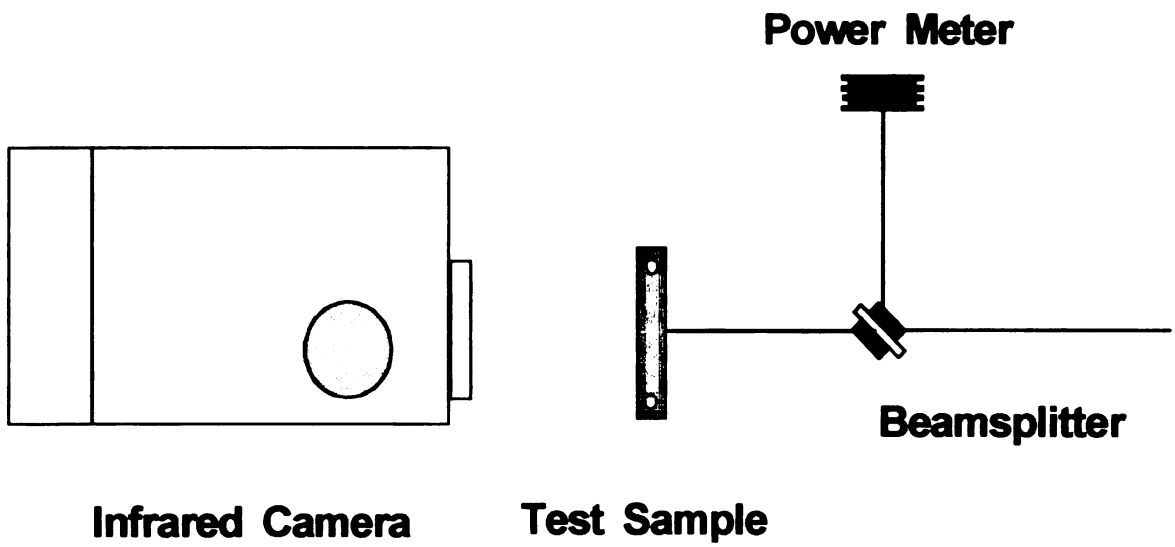

Figure 3.26. *The beamsplitter method of obtaining simultaneous heat flux and temperature information.*

3.3.2.2 ThorLab High Speed Photodetector

ThorLAB's DET2-SI high speed photodector, shown in Figure 3.27, consists of a photo diode and internal 22.5 V battery enclosed in a rugged aluminum housing. A 8-32 tapped hole is provided on the base of the housing for easy mounting. The detector

covers a spectral range of 350 to 1100nm with rise times below 1ns. The specifications of this device are shown in Table 3.1

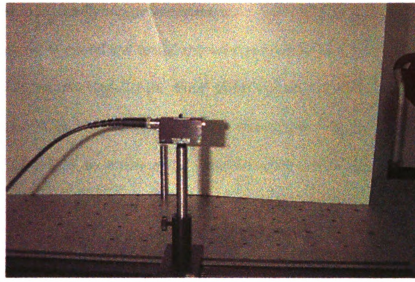

Figure 3.27. *The ThorLAB high speed photodetector.*

Detector:	Silicon PIN	**Housing:**	Black Anodized Alum.
Spectral Response:	350 - 1100nm	**Size:**	0.75"x1.3"x2"
Peak Wavelength:	920nm ± 50nm	**Output:**	BNC , DC-Coupled
Rise/Fall Time:	≤1ns	**Bias:**	22.5 V Battery
Diode Capacitance:	1.8 pF	**Mounting:**	8-32 Tapped Hole
NEP:	5×10^{-14} W/(Hz$^{-1/2}$)	**Diode Socket:**	TO-5 Anode Marked
Dark Current	2.5 nA	**Damage Threshold:**	0.5 J /cm^2 (10 ns pulse)
Active Area	Active Area	**Linearity Limit:**	1 mW

Table 3.1. *Specifications of the ThorLAB DET2-SI high speed photodector.*

The fast response time of this device and its high damage threshold make it a versatile instrument in a laser environment. For example, the output of this device is currently used to externally trigger instrumentation, LabVIEW data acquisition programs, and to measure the temporal and spatial characteristics of the laser beam. .

The BNC output signal is the direct photo current out of the photo diode anode and is a function of the incident light power and wavelength. The sensitivity, S(λ), can be read from Figure 3.28 to estimate the photo current to be expected based on the wavelength of the laser of interest. (Nd:YAG - Wavelength = 1064 nm).

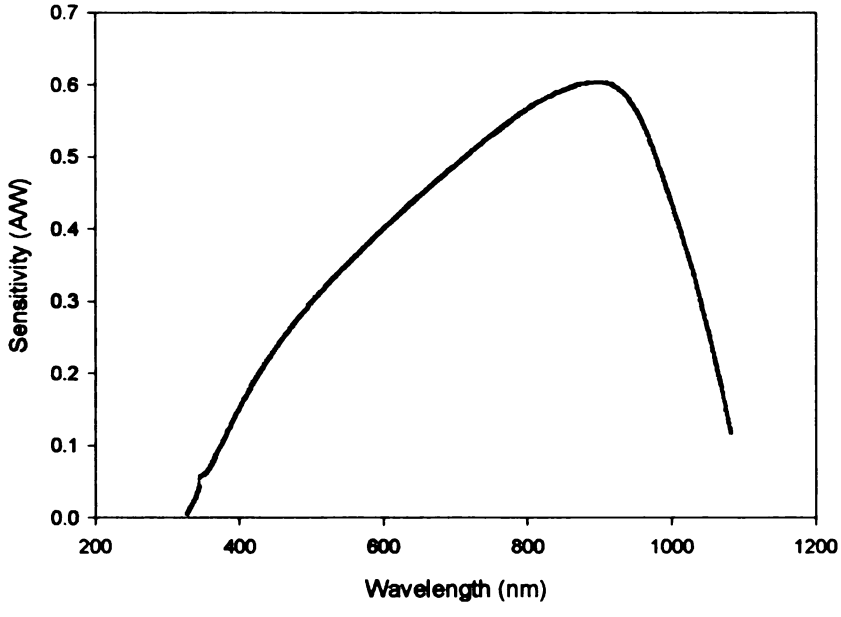

Figure 3.28. *Photodetector sensitivity as a function of wavelength.*

This photo current is converted to a voltage by adding a external load resistance, R_{LOAD}, as shown in Figure 3.29.

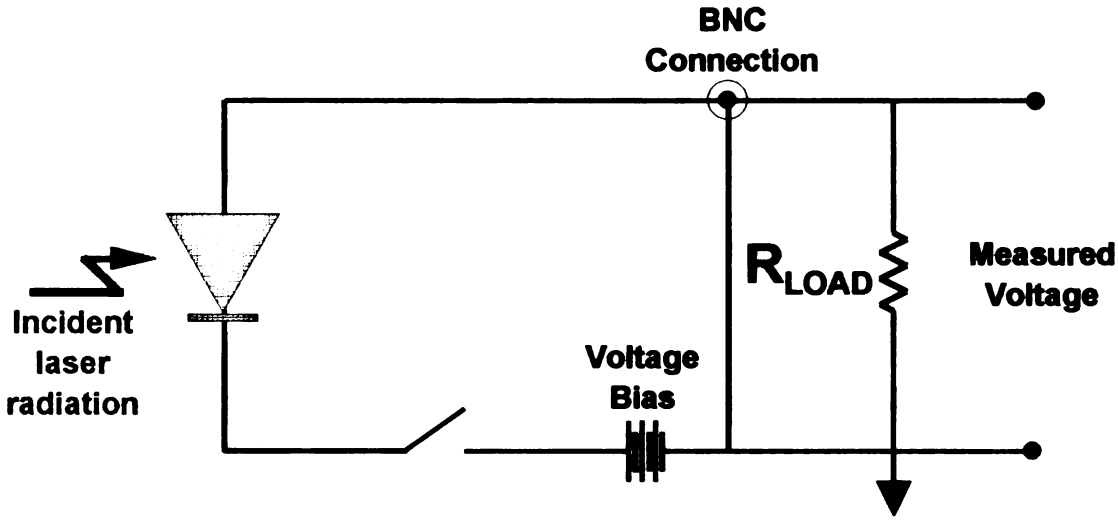

Figure 3.29. *Illustration of the external load used to convert the photo current into a voltage.*

The output voltage of the detector is derived as:

$$V_o = P * S(\lambda) * R_{LOAD} \tag{3.1}$$

The bandwidth, f_{BW}, and the rise time, T_R are determined from the diode capacitance, C_j, and the load resistance, R_{LOAD}:

$$f_{bw} = 1/(2\pi * R_{LOAD} * C_j), \quad T_R = 0.35/f_{bw} \tag{3.2}$$

3.3.2.3Beam Profiling

An intense study concerning beam profiling techniques is included in Appendix D.

3.4 Data Acquisition and Instrument Control

The fundamental task of a data acquisition (DAQ) system is the measurement or generation of physical signals. The typical components of a DAQ system include transducers, signal conditioning accessories (if necessary), data acquisition boards, application software, and a PC with a processing speed sufficient for the application.

For the most part, transducers sense physical phenomena and convert them into electrical signals such as voltage or current. Signal conditioning accessories may be necessary to amplify, isolate, and filter low-level signals allowing for accurate and safe measurements. If the signal is conditioned properly plug-in data acquisition boards can be used to digitize the signal. A data acquisition board can also be used to generate control signals. Application software simplifies the programming necessary for DAQ, allows for data analysis, and data presentation. The PC in the DAQ system determines the overall processing speed of the application. Therefore, applications requiring real-time processing of high frequency signals need a high speed processor possibly with an accompanying coprocessor.

In the following subsections the major components of the newly developed data acquisition system are discussed.

3.4.1 LabVIEW

Software plays a vital role in developing automated data acquisition and instrument control systems. The selected software must span a broad range of functionality, from device drivers for controlling specific hardware interfaces to application software

packages for developing complete systems. With this in mind, LabVIEW was chosen as the software development system.

As shown previously in Figure 3.25, LabVIEW contains the necessary tools for data acquisition and control, data analysis and data presentation, resulting in an integrated system for developing instrumentation software.

LabVIEW is a graphical programming language which includes libraries of functions and development tools designed specifically for data acquisition and instrument control. LabVIEW programs are called Virtual Instruments (VI's) because their appearance and operation imitate actual instruments. However, the flow and structure are analogous to the functions of other conventional programming languages.

There are basically two components to a LabVIEW program. The user interface of a VI is called the front panel. The front panel can contain knobs, push buttons, graphs and other control and indicator functions. The VI receives its instructions from a block diagram. This block diagram is basically a wire diagram of a pictorial solution to a programming problem. Within the block diagram a variety of tools are available in the form of subVIs. The tools within these subVIs may include the function calls necessary for communication with plug-in data acquisition boards or algorithms previously created by the user or by the manufacturer. These subVIs allow for modular programming and as a result complicated tasks can be divided into many simpler subtasks.

3.4.2 ATMIO-16F Multipurpose Data Acquisition Board

The high performance AT-MIO16F-5 data acquisition board has been used as a primary source for general data acquisition and instrument control for this application. The

AT-MIO16F-5, with its multifunction analog, digital and timing I/O can be used in many applications for automation of machine and process control, level monitoring and control, instrumentation, electronic testing, and various other functions. The multichannel analog input can be used for transient analysis or data logging. The two analog output channels can be used for such functions as machine and process control and analog function generation. The eight TTL compatible digital I/O lines can be used for such functions as machine and process control, intermachine communication, and relay switching control [Johnson, 1993]. The three 16-bit counter/timers can be used for such functions as pulse or clock generation, timed control of laboratory equipment, and frequency, event, and pulse width generation.

More specifically, the AT-MIO-16F board allows for 16 single ended or 8 differential ended inputs. The board's analog to digital conversion (ADC) has a 12 bit resolution and a 5 μsec conversion speed. Both low-level and high-level signals can be measured with this board using the software-programmable gain amplifier to apply gains of 0.5, 1, 2, 5,10, 20, 50. National Instruments ensures full accuracy at all gain setting even at the maximum sampling rate of 200 ksamples/sec. The AT-MIO16F-5 has a 2048 sample deep first-in-first out (FIFO) buffer for storing ADC results before transferring the data to the computer memory through interrupts or DMA. The FIFO helps prevent problems associated with so processor speed or data loss during data transfer delays such as those that occur due to interrupt latencies.

3.4.3 EISA-A2000 High Speed Data Acquisition Board

The EISA-A2000 board can be used to digitize signals resulting from high speed events and is used when the data acquisition capabilities of the AT-MIO-16F are not sufficient. It was incorporated into this system to be used with the EG&G IR detector for through thickness flash experiments. The EISA-A2000 can be used in the laboratory for instrumentation waveform recording, and electronic test and measurement applications. The fast, 12 bit resolution analog input makes the board useful for high-performance signal analysis, transient analysis, pulse parameter measurement, and data logging. The multichannel simultaneous ADC sampling is ideal for position and phase analysis of multiple signals. Functions such as analog and digital triggering, pretrigger and posttrigger modes, programmable AC/DC coupling are easily implemented through the use of LabVIEW VI's. Input to the various channels are made through a BNC adapter located on the rear panel of the host Gateway 486-66 computer.

More specifically this data acquisition board contains a 1Msamples/sec, 12 bit resolution analog to digital expansion board for an EISA bus computer. The board has four analog input channels, each with its own sample and hold circuitry. The board can sample one channel at 1Msamples/sec, two channels simultaneously at 500 ksamples/sec, and four channels at 250 ksamples/sec. Data acquisition from the input channels can be started from software, digital triggers, or analog triggers.

As mentioned LabVIEW is used to configure the EISA-A2000 for A/D conversion. By default the board is set to acquire data in an AC coupled mode. In this

mode the input channel range is ±5 V peak AC with ± 25 VDC offset. When configured to acquire data in the DC coupled mode the input channel range of the board is ± 5 V DC.

In order to work as an effective tool for data acquisition the EISA-A2000 is equipped with several trigger modes. In the pretrigger mode the EISA-A2000 acquires a specified number of scans before and after it receives the trigger condition. In posttrigger mode, the board acquires a specified number of scans after the trigger. In the posttrigger mode with delay, the EISA-A2000 waits to acquire scans until a specified time interval elapses after the trigger condition.

These trigger modes have two sources - analog and digital. The analog trigger can be received from any one of the input channels or the ATRIG input on the I/O connector. Analog trigger circuitry causes a trigger when selected input channel reach a preprogrammed slope and level. A leading or trailing edge digital trigger can be received from the DTRIG I/O connector input. In most situations a rising edge in the response of the photodetector was used to trigger data acquisition.

3.5 Miscellaneous Experimental Equipment

3.5.1 FOR.A Video Timer

The VTG-33 video timer, shown in Figure 3.30, is an all-electronic compact unit which superimposes digital indications of time and date on standard RS-170 video events. The crystal controlled IC circuitry provides a reliable and accurate time base indications with a temporal resolution of 0.01 of a second.

This timer has an advantage over the unit (FOR.A 212) used in the past because its remote capabilities allow for external triggering. A TTL low signal, shown in Figure 3.31,

supplied to the remote control connector on the rear panel can be used as a trigger. The connection pinouts for this for this external trigger are shown in Figure 3.32.

Figure 3.30. *The FOR.A VTG33 Video Timer.*

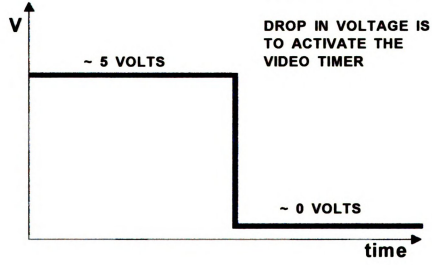

Figure 3.31. *An example of the TTL signal. This signal is used to remotely start the VTG 33 video timer.*

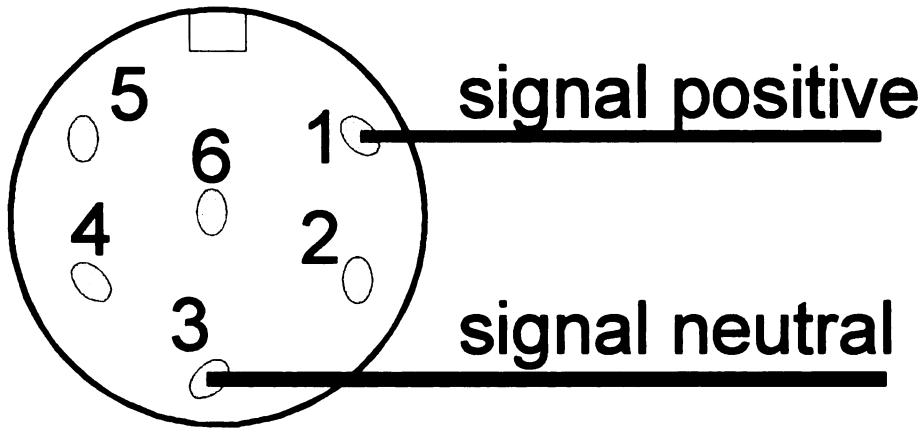

Figure 3.32. *The wiring connections for external triggering of video timer.*

In this work the video timer was used to superimpose time indications onto the output of the radiometer. The timing allowed for the temperature distributions to be sampled at known times. The remote triggering capability offered by this unit was desirable because it allowed for an accurate means to initiate timing.

Chapter 4

Description of Mathematical Model

Along with well understood experimental components and measurement techniques, inverse heat conduction and parameter estimation rely on the development of accurate experimental models. A heat transfer model, previously developed by J.V. Beck and F Breidenich in 1994, is used to describe samples used in the present experimental setup such that the thermal behavior of the experiment can be predicted analytically. Without such a model, the desired thermal properties can not be estimated and without an accurate description from the model, any results are meaningless. Therefore, although this description of the mathematical model is not original, it is included in this work for completeness. Since there is a certain amount of error and uncertainty associated with each experiment, the mathematical model can also be used to determine if a certain

experiment can be successful. This chapter is dedicated to a discussion of the experimental model developed for estimating the thermal diffusivity parallel to the surface of the material of interest. This one dimensional radial heat flow model describes the temperature distribution for transient and quasi steady state time periods.

4.1 Mathematical Model

Conductive heat transfer can be described by the transport of energy in a medium as the result of a temperature gradient. In nonmetallic solids, the physical mechanism for this transport is the random activity between atoms and molecules. In a solid body with a temperature gradient, Fourier's Law is used to relate the heat flux (q) to the temperature (T)

$$q(r,T) = -k(r,T)\nabla T(r,T) \tag{4.1}$$

where the k [W/m K] is the effective thermal conductivity of the material, the temperature gradient ∇T [c/m] is a vector normal to the isothermal surface and the heat flux vector is the heat flow per unit time and unit area. The minus sign is inserted in accordance with the second law of thermodynamics. For example, if heat flows in a positive direction, the temperature must decrease in that direction. For an isotropic , circular body, the two components of q in the r and z direction are given by:

$$q_r = -k_r \frac{\partial T}{\partial r}; q_z = -k_z \frac{\partial T}{\partial z} \tag{4.2}$$

Using the conservation of energy and assuming that heat conduction is restricted to the radial direction, the one dimensional heat conduction equation can be derived as

$$\frac{1}{r}\frac{\partial}{\partial r}\left(r\frac{\partial T}{\partial r}\right)+\frac{q(r)}{k_r\delta}=\frac{1}{\alpha_r}\frac{\partial T}{\partial t} \tag{4.3}$$

The assumption of one dimensional heat flow seems to be valid for thin films as they are relatively isothermal in the z direction during heating. Due to the present temperature levels and the high thermal conductivity of the test specimens, the established model assumes that there are negligible convective and radiative losses from the specimen to the surroundings.

The first term in equation (4.3) describes the net conductive heat flux into the control volume, the second term is the rate of effective internal heat generation within the heated area and the right hand side of the equation represents the energy storage rate. In the quasi-steady state, the energy storage rate is a constant and equation (4.3) will be used in this case to derive a closed form algebraic expression for one of the two quasi-steady state terms. The heat flux q (r) is q_o for 0<r<a and zero is the area a<r<b, see Figure 4.1.

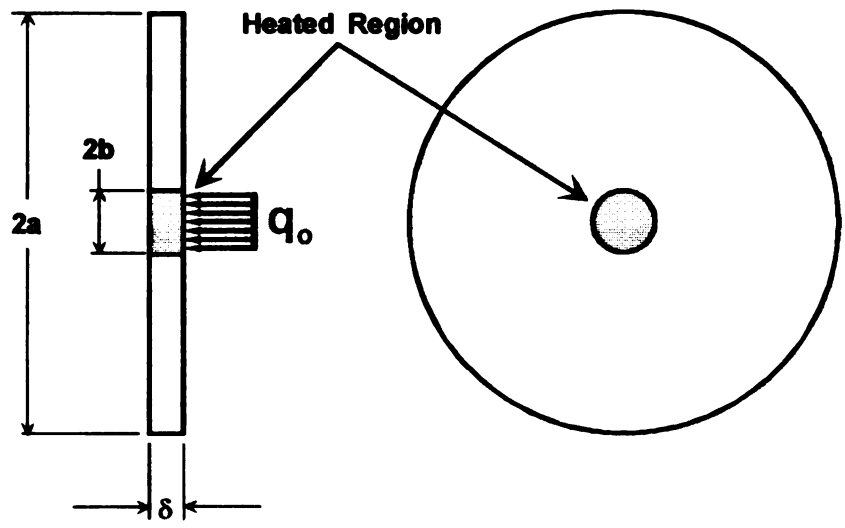

Figure 4.1 Schematic representation of the test specimen.

The Green's function solution for one dimensional radial heat flow in a circular disk with a natural boundary condition in the center and an insulated boundary condition at the edge (r=b) is [Beck *et al* 1992]:

$$T(r,t)=\frac{\alpha_r}{k_r}\int_{\tau=0}^{t}\int_{r'=0}^{b} g(r',\tau)G_{R02}(r,t|r',\tau)2\pi r'\,dr'\,d\tau + T_i \qquad (4.4)$$

This formulation assumes that there are no convective or radiative losses and that the source term $g(r',\tau) = q/\delta$ [W/m^3] is the continuous heat flux generated by a laser in the area ($0<r<a$) of the sample, where δ is the thickness of the sample. The Green's function for the R02 case is

$$G_{R02}(r,t|,r',\tau)=\frac{1}{\pi b^2}\left[1+\sum_{m=1}^{\infty} e^{-\beta m^{\alpha} r(t-\tau)/b^2}\,\frac{J_o(\beta_m r/b)J_o(\beta_m r'/b)}{J_o^2(\beta_m)}\right] \qquad (4.5)$$

where $J_o(x)$ is the Bessel function of the first kind of order zero and evaluated at x and β_m's are the eigenvalues of the eigencondition, $J_1(\beta_m) = 0$. The following paragraphs describe the solution of equation (4.4) for times in transient and quasi-steady state. Since values of the dimensionless time ($\alpha t/b^2$) tend to be greater than 0.5 for all considered materials at respective heating times, the main solution of interest in expected to be the quasi-steady state, that is, a linearly increasing temperature with time. Thus, the solutions of equation (4.5) can be expressed as a sum of the four following terms:

$$T(r,t)=T_{QS1}(t)+T_{QS2}(r)+T_{TR}(r,t)+T_i \qquad (4.6)$$

where $T_{QS1}(t)$ is the first quasi-steady state term from the constant in equation (4.5), $T_{QS2}(r)$ is the second quasi-steady state term from the infinite series in equation (4.5), $T_{TR}(r,t)$ is the transient state term from the infinite series and T_i is the initial temperature as

shown in equation (4.4). Here, $T_{QS1}(t)$ describes the linear dependence between temperature and time and $T_{QS2}(r)$ contains the information about the spatial temperature distribution during the quasi-steady state period.

Integrating the constant 1 in equation (4.5) and assuming that the heat flux, q, is the constant and uniform term q_o in the region 0<r<a and zero in the region a<r<b, see Figure 4.1. Under this assumption the quasi-steady state term becomes:

$$T_{QS1}(t)=\frac{q_o\alpha_r t a^2}{\delta k_r b^2} \tag{4.7}$$

The second quasi-steady state term can be derived by substituting the infinite series into equation (4.4), leading to an infinite sum that then would have to be integrated. On the other hand a solution for $T_{QS2}(r)$ can be found by substituting equation (4.6) and equation (4.7) into equation (4.3) for both regions 0<r<a and a<r<b respectively. This leads to a closed form algebraic expression for $T_{QS2}(r)$. The transient term, $T_{TR}(r,t)$ disappears for the quasi-steady state solution. In order to make the solution more computationally efficient, the latter method is used. The term on the right side is a constant determined from equation (3.7):

$$C=\frac{1}{\alpha_r}\frac{\partial T_{QS1}(r)}{\partial t}=\frac{q_o a^2}{\delta k_r b^2} \tag{4.8}$$

since $\partial T_{QS2}(r) / \partial t=0$ and $\partial T_{TR}(r,t) / \partial t$ are neglected for the quasi-steady state. Solving the differential equation (4.3) for 0<r<a, the general solution is obtained

$$T_{QS2}(r)=\frac{1}{4}\left(C-\frac{q_o}{k_r\delta}\right)\left(r^2-a^2\right)+D_1\ln(r)+D_2, \qquad 0<r<a \tag{4.9}$$

Using the boundary conditions at r = 0 of

$$T_{QS2} \text{ is finite as } r \to 0 \tag{4.10}$$

Yielding D1 = 0. Assume for a moment that the temperature at r = a is T_a:

$$T_{QS2} = T_a \tag{4.11}$$

Then the solution for 0<r<a is:

$$T_{QS2}(r) = \frac{1}{4}\left(C - \frac{q_o}{k_r \delta}\right)\left(r^2 - a^2\right) + T_a, \qquad 0 < r < a \tag{4.12}$$

For the region a<r<b, the volumetric energy generation term in equation (4.3) is zero. Thus, the general solution for the differential equation is given by

$$T_{QS2}(r) = \frac{1}{4}Cr^2 + D_3 \ln r + D_4 \tag{4.13}$$

Using the two boundary conditions

$$T_{QS2}(a) = T_a \tag{4.14}$$

and (4.14)

$$\left.\frac{dT_{QS2}(r)}{dr}\right|_{r=b} = 0 \tag{4.15}$$

the second quasi steady state term and for the non-heated region then becomes

$$T_{QS2}(r)=C\left[\frac{1}{4}\left(r^2-a^2\right)+\frac{1}{2}b^2\ln\left(\frac{a}{r}\right)\right]+T_a \qquad a<r<b \tag{4.16}$$

Equation (4.12) and (4.16) still contain the unknown T_a. The equation for heat flow continuity at boundary r=a for both solution, $T_{QS2}(0<r<a)$ and $T_{QS1}(a<r<b)$, equation (3.17), can be used to determine C

$$\frac{\partial T_{QS2}(0<r<a)}{\partial r}\Big|_{a-}=\frac{\partial T_{QS2}(a<r<b)}{\partial r}\Big|_{a+} \tag{4.17}$$

which was already known from equation (3.18). Hence the heat flux continuity condition at the interface is satisfied.

$$C=\frac{q_o a^2}{k_r \delta b^2} \tag{4.18}$$

The task now is to determine T_a. At time zero the average temperature for $T_{QS2}(r)$ is zero or

$$\int_{r=0}^{b} T_{QS2}(r)2\pi r\,dr=0, \qquad t=0 \tag{4.19}$$

The quasi - steady temperature distribution integrated across the heated (0<r<a) and non heated (a<r<b) areas add up to equal zero. Integrating the expression for $T_{QS2}(r)$ from r=0 to a and from r=a to b respectively gives:

$$\int_{r=0}^{a} T_{QS2}(0<r<a)2\pi r dr+\int_{r=a}^{b} T_{QS2}(a<r<b)2\pi r dr=0 \tag{4.20}$$

Solving for T_a yields

$$T_a = \frac{a^4}{8b^2}\left(C - \frac{q_0}{k_r \delta}\right) - \frac{3Cb^2}{8} - \frac{Ca^4}{8b^2} + \frac{Cb^2}{2}\left(\ln(b) - \ln(a)\right) + \frac{Ca^2}{2} \qquad (4.21)$$

Since the experimental design is such that only temperature data in the non-heated region is used for the estimation of α_r, the solution $T_{QS}(a<r<b)$ is the only one that needs to be derived. Temperature measurements from the region $0<r<b$ are omitted, because the spatial power distribution of the heat source is not constant as assumed in the derivation of the mathematical model. Hence, substituting equation (4.18) and (4.21) into (4.16) the second term for the quasi-steady state temperature distribution for the non heated region becomes

$$T_{QS2}(r) = \frac{q_o a^2}{k_r \delta}\left[\frac{a^2}{4b^2}\left(\frac{r^2}{a^2} + \frac{1}{2}\right) + \frac{1}{2}\left(\ln\left(\frac{b}{r}\right) - \frac{3}{4}\right)\right], \qquad a < r < b \qquad (4.22)$$

Now, a term for the last unknown, the temperature distribution for transient times T_{TR} has to be determined. The infinite series in equation (4.5) has to to be integrated, leading to a solution for $T_S = T_{QS}(r) + T_{TR}(r,t)$. Already knowing the expression for $T_{QS2}(r)$, only the term for $T_{TR}(r,t)$ is still of interest

$$T_s = \frac{\alpha_r q_o a}{k_r \delta \pi b^2} \int_{\tau=0}^{t} \int_{r'=0}^{a} \sum_{m=1}^{\infty} e^{-\beta^2 m^2 \alpha_r (t-\tau)/b^2} \frac{J_o(\beta_m r/b) J_o(\beta_m r'/b)}{J_o^2(\beta_m)} 2\pi r' dr' d\tau \quad (4.23)$$

Integration over r', using the substitution $x=\beta_m r'/b$ equation (4.23) then reduces to

$$T_s = \frac{2\alpha_r q_o a}{k_r \delta b} \int_{\tau=0}^{t} \sum_{m=1}^{\infty} e^{-\beta^2 m^2 \alpha_r (t-\tau)/b^2} \frac{J_o\left(\beta_m \frac{r}{b}\right) J_1\left(\beta_m \frac{a}{b}\right)}{J_o^2(\beta_m)} d\tau \quad (4.24)$$

Integrating equation (4.24) over time, the term

$$T_s = \frac{2q_o ab}{k_r \delta} \sum_{m=1}^{\infty} \frac{J_1\left(\beta_m \frac{a}{b}\right) J_o\left(\beta_m \frac{r}{b}\right)}{\beta_m^3 J_0^2(\beta_m)} \left[1 - e^{-\frac{\beta_m \alpha_r t}{b^2}}\right] \quad (4.25)$$

is obtained. The constant part (independent of time) in the eqn. (4.25) is equal to the closed form algebraic expression $T_{QS2}(r)$ (4.22) and therefore the exponential term must be equal to $T_{TR}(r,t)$

$$T_{TR}(r,T) = -\frac{2q_o ab}{k_r \delta} \sum_{m=1}^{\infty} \frac{J_1\left(\beta_m \frac{a}{b}\right) J_o\left(\beta_m \frac{r}{b}\right)}{\beta_m^3 J_o^2(\beta_m)} \left[e^{-\frac{\beta_m^2 \alpha_r t}{b^2}}\right] \quad (4.26)$$

An analysis of eqn. (4.26) at various times using the physical properties and dimensions of the copper, iron, and diamond samples shows that the ratio of $T_{TR}(r,t)/T(r,t)$ is smaller than 1.0 percent. This result is expected since the characteristic sampling time for each of the samples was selected based and their thermophysical properties such that the dimensionless time ($\alpha t/b^2$) was greater than 0.5. Based on this analysis, the transient

part of the solution is neglected, leading to the quasi-steady state solution for the temperature distribution in the a<r<b region,

$$T(r,T)=\frac{qa^2}{k\delta}\left[\frac{\alpha t}{b^2}+\frac{a^2}{4b^2}\left(\frac{r^2}{a^2}+\frac{1}{2}\right)+\frac{1}{2}\left(\ln\left(\frac{b}{r}\right)-\frac{3}{4}\right)\right]+T_i \qquad a<r<b \quad (4.27)$$

4.2 Parameter Estimation

The ability to acquire temperature distributions along the surface of a sample and predict this behavior with a mathematical model provides a great deal of data and insight into the thermal behavior of the material. A third tool must be utilized to analyze this information and estimate the desired thermophysical properties. This tool is parameter estimation. As a discipline, parameter estimation provides the necessary algorithms to estimate the constants that appear in mathematical models such as that in equation (4.27). The present problem is an inverse problem because not all the constants in the mathematical model are known. Using parameter estimation, these unknown constants are estimated based on the temperature distribution. In this case, a nonlinear sequential parameter estimation program called NLIN [Beck, 1994] is used to estimate the thermal diffusivity, β_2, and the values for the laser effect term, β_1, and the initial temperature, β_3.

NLIN uses the method of least squares

$$S = \sum_{j=1}^{N} [Y_j - T_j]^2 \tag{4.28}$$

where N is the number of data points, Y_j is the measured temperature and T_j is the calculated temperature represented by (4.27). A simplified version of this equation is repeated here for convenience,

$$T_j = \beta_1 \left[\frac{\beta_2 t}{b^2} + \frac{a^2}{4b^2}\left(\frac{r^2}{a^2} + \frac{1}{2}\right) + \frac{1}{2}\left(\ln\left(\frac{b}{r}\right) - \frac{3}{4}\right)\right] + \beta_3 \tag{4.29}$$

where $\beta_1 = qa^2/k_r\delta$, $\beta_2 = \alpha_r$, and $\beta_3 = T_{initial}$. Using the method of least squares the NLIN program simultaneously estimates β_1, β_2, and β_3 to calculate T_j such that the error in S is minimized. In order to minimize the error in S, NLIN uses the following system of equations

$$\frac{\partial S}{\partial \beta_1} = 2\sum_{j=1}^{N}\left[Y_j - T_j\right]\frac{\partial T_j}{\partial \beta_1} \tag{4.30}$$

$$\frac{\partial S}{\partial \beta_2} = 2\sum_{j=1}^{N}\left[Y_j - T_j\right]\frac{\partial T_j}{\partial \beta_2} \tag{4.31}$$

$$\frac{\partial S}{\partial \beta_3} = 2\sum_{j=1}^{N}\left[Y_j - T_j\right]\frac{\partial T_j}{\partial \beta_3} \tag{4.32}$$

NLIN not only fits the mathematical model to the experimental data and sequentially estimates the desired parameters, but it also calculates the experimental residuals. These residuals are the differences between the measured and calculated temperatures $[Y_j-T_j]$ and when analyzed provide information about the error within the experiment. A hard copy of the NLIN program can be found in Appendix H. An NLIN output file from an experiment conducted on a CVD diamond film is given in Appendix I.

Chapter 5

Procedures and Results for One Dimensional Radial Experiments

This chapter presents the experimental procedures and results for the measurement of the thermal diffusivity of three different materials: iron, copper, and CVD diamond film. The following subsections describe the steps involved in sample preparation, experimental setup, the procedures necessary for measuring the surface temperatures, and the experimental uncertainty involved in the estimation of the thermal diffusivity.

5.1 Sample Description and Preparation

Infrared temperature measurement systems respond to the sum of the radiation emitted, reflected, and transmitted by and/or through the surface of interest. As a result, inherent problems arise with IR systems when attempting to acquire accurate temperature measurements of surfaces with variations in emissivity, high reflectivity and high transmissivity. For example, in Figure 5.1(a.) a boron doped diamond film on a silicon

substrate is placed in the field of view of the IR camera. The surface of this specimen is such that a uniform surface emissivity could be assumed and the specimen is non-transparent in the visible spectrum. Although this diamond-silicon composite is relatively thick (~300μm), it is transparent in 8 μm to 12 μm range. As shown in Figure 5.1(b.) a small radiating body (heated resisitor) was placed behind the specimen and caused an apparent temperature difference across the surface of the sample. One of the common methods used to eliminate problems like this and others resulting from variations in surface emissivity and high reflectivity is to coat the sample with a thin coat of high emissivity material.

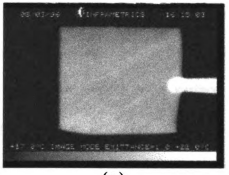

(a.)

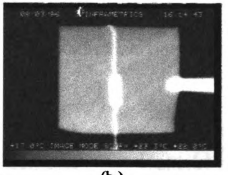

(b.)

Figure 5.1 (a.) *A diamond film on silicon substrate placed in the field of view of the Inframetrics Model 600L radiometer.* ***(b.)****A radiating bodies placed behind the sample illustrating the effects of measuring the surface temperature of high transmissivity materials.*

In this present work the thermal diffusivities of copper, iron and CVD diamond films are measured. The copper and iron samples were purchased from the Goodfellow Corporation and are guaranteed to have a purity of 99.999% of 99.79%, respectively. The samples, shown in Figure 3.2, have a constant thickness of 500μm and a diameter of 5.08 cm. The surfaces of these samples are semi-polished and therefore have a high reflectivity. This high reflectivity causes temperature measurement problems because background sources operating at high temperature, such as power supplies or oscilloscopes, may produce an artifactual apparent temperature differences across the surface of a reflective test sample. Another problem arises because this high reflectivity is associated with a low absorbtivity. Therefore, if it is of interest to maximize and/or quantify the amount of laser radiation deposited onto the surface of the test specimen a thin high absorbtivity material must be applied to the surface of the sample. In order to eliminate these potential problems, a thin coat of high temperature resistant, high emissivity black paint was added to each surface of the test samples. The emissvity of this black paint was experimentally determined to be 0.96.

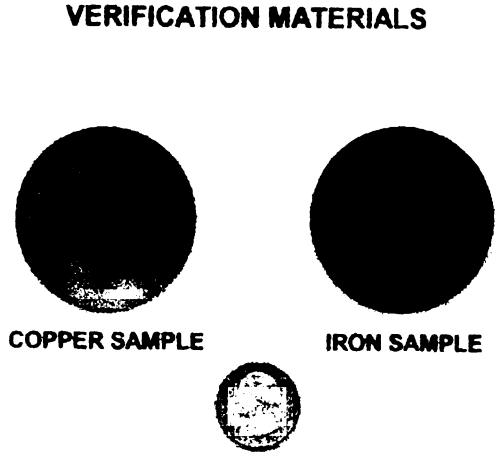

Figure 5.2. *The copper (left) and the iron (right) samples used in this experiment. Each of the samples are 5.08 cm in diameter and have a thickness of 500μm.*

Three freestanding CVD diamond films, created using a microwave plasma deposition process and shown in Figure 5.3, were studied in this experiment. These films, referred to as sample AT#4, ST#120, and ST#192, have average thicknesses of 370 μm, 370 μm, and 240 μm respectively (thickness variations are less than 15%), and diameters of 5.08 cm. The surfaces of the samples are drastically different. The substrate or bottom surface, where the crystalline growth was initiated, is smooth and highly reflective. The growth or top surface is coarse and not very reflective. This rough surface appears to be such that a uniform surface emissivity could not be assumed. Tests similar to that shown in Figure 5.1 illustrate that the three specimen do not transmit radiation in 8 to 12 μm range. As with the copper and iron samples the potential measurement problems were eliminated by adding a thin layer of black paint to each surface of the diamond samples.

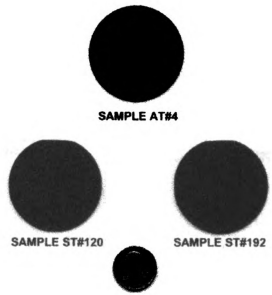

Figure 5.3. *The three CVD diamond films measured in this study. Each of the samples have a diameter of 5.08 cm. The average thicknesses of sample AT#4, ST#192, and ST#120 are 370μm, 370 μm, and 240 μm respectively.*

5.2 Experiment Setup and Measurement Techniques

The experimental setup contains seven components: 1.) The Inframetrics Model 600L Infrared Imaging Radiometer, 2.) a Excel/Quantronix Model 117E Nd:YAG Laser, 3.) a Thorlab's high speed silicon photodetector, 4.) a PC based data acquisition system, 5.) FOR.A VTG33 Video Timer, 4.) a JVC video cassette recorder, and 7.) an image processing system. A diagram of the data experimental setup is shown in Figure 5.4.

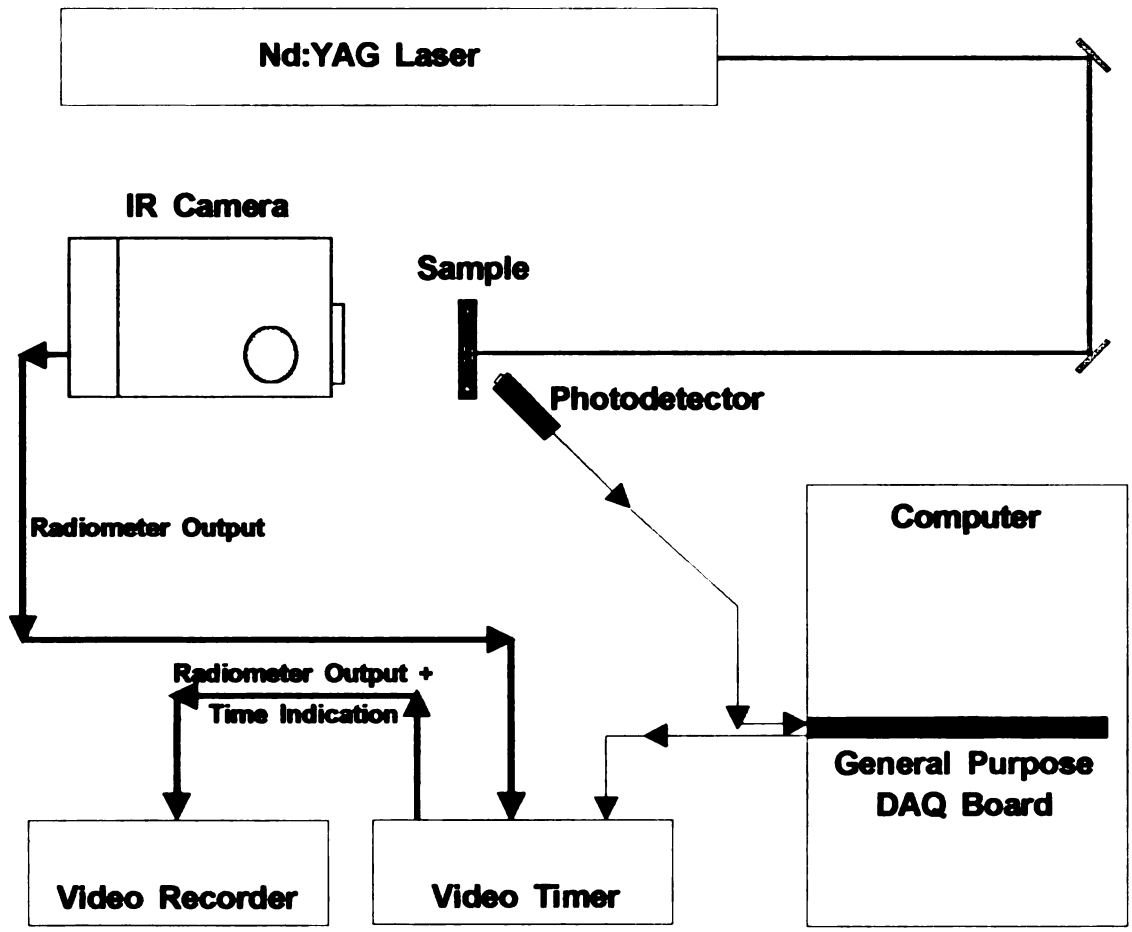

Figure 5.4. *Schematic representation of the experimental setup used for measuring the parallel thermal diffusivity of several thin circular test samples.*

The theory and specifications of the major components are described in Chapter 3 and will not be repeated here. Instead, this section is devoted to a discussion on the specific operating conditions and setup operations required for data acquisition.

The placement of the radiometer with respect to the sample is important. The optical axis of the radiometer's lens system must be centered on back of test specimen. Poor alignment will cause spatial distortions and will effect the precision to which the radial locations of individual temperature measurements are known. The distance of between the radiometer and the test specimen is minimized. This acts to increase the spatial resolution of the system and yields the maximum amount of temperature information.

After the specimen and radiometer are in place, the radiometer settings are adjusted and the system is prepared for data acquisition. Based on previous experimental tests, the emissivity was of the black paint was determined to be approximately 0.96. The camera's thermal sensitivity was maximized by operating the radiometer in the smallest possible temperature range. The temperature range setting in most cases was 10°C and is dependent on the thermal behavior of the sample and the specific test conditions. The image averaging mode of the radiometer was activated and four images were averaged in real time. Image averaging is an attractive feature for two reasons. First, the signal-to-noise ratio is increased by a factor of two and second the amount of data is compressed by a factor of four.

The output of the radiometer is in RS-170 video format. As a result, the output is passed through a standard video timer and digital indications of time and date are superimposed onto each frame . In this format, the output could analyzed in real-time

using a general purpose image processing system or stored on conventional video recording equipment for future analysis.

The heating source for these experiments was the Nd:YAG laser. The laser was operated in it continuous wave (CW) mode with various power levels depending on the thermal physical properties of the test specimen. For example, the iron samples dissipate heat much more slowly than the diamond samples. As a result, low power levels cause significant temperature increases in the center portion of these samples. As previously mentioned, the temperature setting on the radiometer controls the thermal resolution of the measured data. Since it is desirable to minimize the temperature resolution, the laser power must be attenuated so saturation does not occur during the time period in which data acquisition occurs. In general, the approximate power levels used to energize the iron, copper, and diamond samples are 750 mW, 3.5 W, and 3.0 W respectively.

The alignment of the beam with respect to the center of the test specimen is another key portion to the experimental setup. The mathematical model relies on the fact that the heat source is concentrated on the center of the sample. Misalignment could produce a non-symmetric temperature distribution or other erroneous results. This alignment can be achieved in two ways. Course adjustments in alignment can be achieved by physically moving the beam to different locations on the specimen. This is done by adjusting the external mirrors which are used to deliver the beam to the optical table. Fine adjustments are made by translating the sample and the radiometer to various locations using an X-Y positioner manufactured by ORIEL (model #14901). This positioner, shown in Figure 5.5, can be transferred along an optical rail and allows for micro-positioning of the specimen.

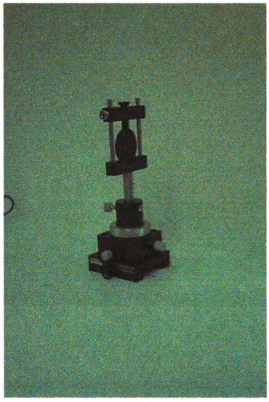

Figure 5.5. *The ORIEL X-Y positioner. This device can be moved to various locations along the optical rail and allows for micro-positioning of specimen for beam alignment.*

In both cases, the alignment can verified using the output from the radiometer in conjunction with the IPPLUS image processing system. A sample with proper and improper laser beam alignment are shown in Figures 5.6 and 5.7 respectively.

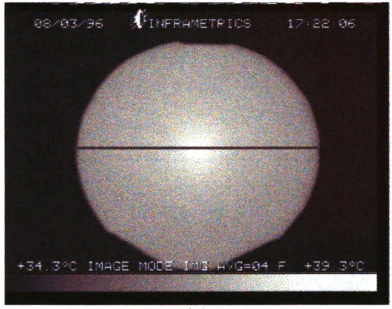

(a.)

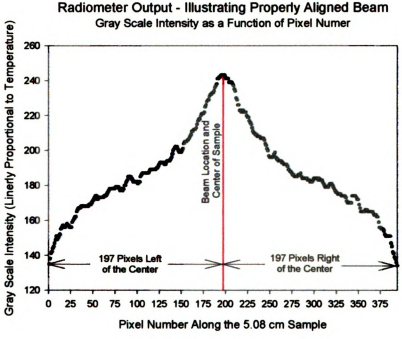

(b.)

Figure 5.6. *The output of the radiometer is used in conjunction with the IPPLUS image processing system to verify that the laser is properly aligned in the center of the test specimen. Note the symmetry in gray level (temperature) distribution.*

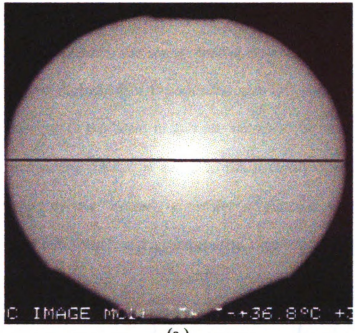

(a.)

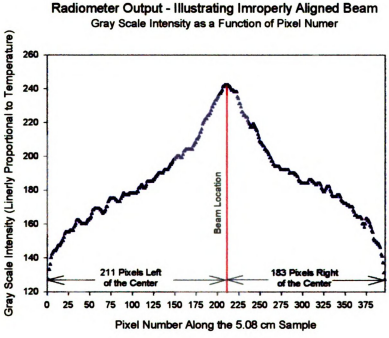

(b.)

Figure 5.7. *The output of the radiometer is used in conjunction with the IPPLUS image processing system to illustrate that the beam is improperly aligned. Note the asymmetry in gray level (temperature) distribution.*

With the beam properly aligned and the radiometer prepared to acquire data, the photodetector must be positioned, the timing control system must be established. As shown in Figure 5.8, the photodetector is positioned such that beam reflections from the sample and the presence of the beam in general, causes an increase in the detector's output. A 1 MΩ terminating resistor is added to the photodetector circuit. Even with relatively low amounts of laser intensity a resistor of this size yields an appreciable detector response (~ 3 to 6 volts), and a characteristic time less than 4.0 μs.

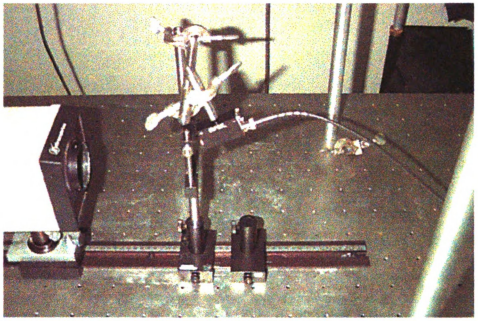

Figure 5.8. *The positioning of the photodetector with respect to the test sample.*

The output of the photodector is connected to the one of the analog input channels on the AT-MIO-16F data acquisition board. A LabVIEW VI, shown in Figure 5.9, is used to monitor the response of the detector. When the detector output increases beyond a preprogrammed voltage level, a TTL low signal is delivered from the data acquisition board to the FOR.A video timer. This signal externally triggers the video timer and allows for accurate digital indications of time to be superimposed onto the radiometer's RS-170

formatted output. The specific operating instructions for this program and the proper connections to the data acquisition board are discussed in detail in Appendix F.

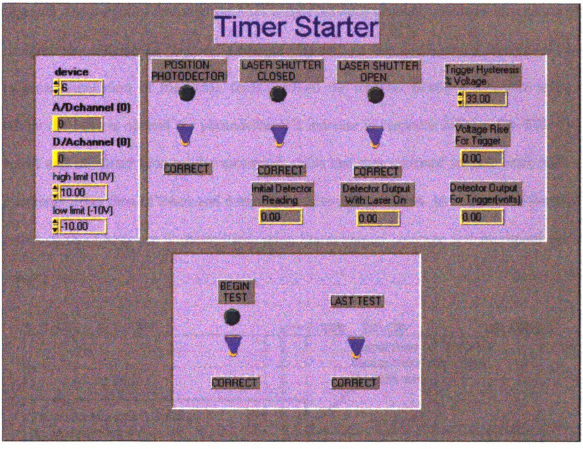

Figure 5.9. *The front panel of a LabVIEW VI which is used to monitor the response of the photodetector. When the program senses that the detector response has exceeded a preprogrammed trigger level it initiates a data acquisition board to send a TTL low signal to external connections on the rear panel of the video timer.*

With any program in which timing issues are important, the execution time must be measured. In this case, it is important to quantify the length of time necessary for the LabVIEW program to recognize that there is an increase in photodetector response beyond the preprogrammed trigger level, and respond by transferring a TTL low signal from the DAQ board to the external connection on the rear panel of the video timer.

The delay time is measured by operating aligning the photodector and operating the LabVIEW program as if an experiment was actually being conducted. In this case, however, the output of the photodetector is split between channel 1 an input channel on an oscilloscope and analog sent to a second channel on the oscilloscope instead of the external connection of the video timer. When the internal electro-mechanical shutter within the laser is opened the photodetector's increase in response initiates the TTL low signal and the delay time can be measured. This test was repeated several times with a maximum delay time of 24ms and a minimum delay time of 16ms. In Figure 5.10 the time traces of three tests are illustrated indicating the minimum, average and maximum delay times.

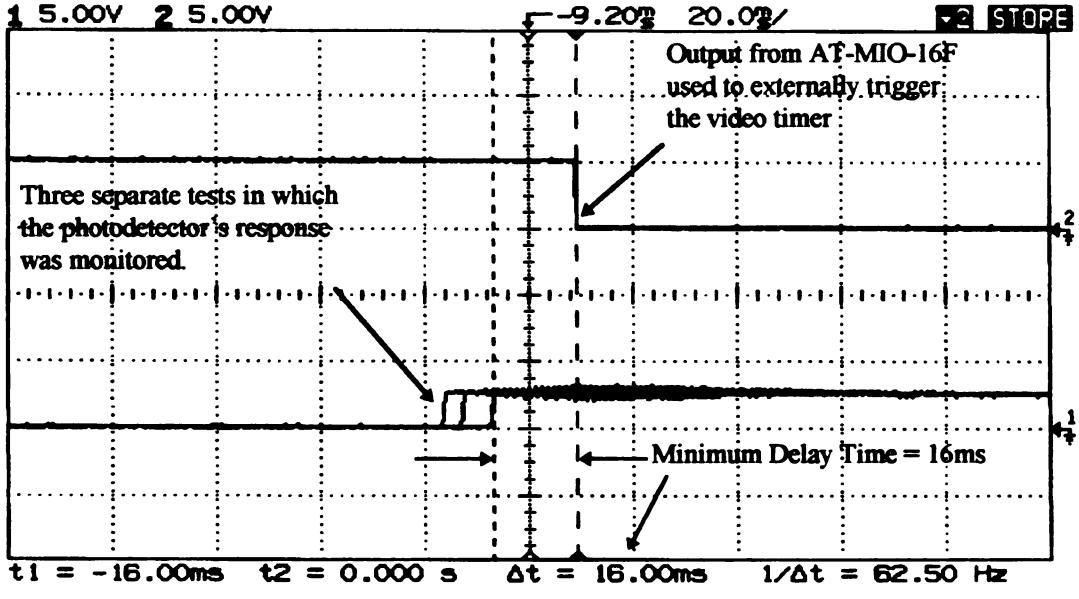

Figure 5.10. *The response of the photodetector and data acquisition board used to measure the execution time of the LabVIEW VI in Figure 5.9. This VI is responsible for externally triggering the video timer.*

The response time of the video timer after a TTL low signal is received is on the order of nanoseconds [personal communication with FOR.A Corporation representatives].

Therefore, the most significant portion of the delay between photodetector's response and the onset of timing is associated with program's execution time. Even though this delay is quite substantial, the 16 to 24 ms execution time does not cause problems because the frame rate of the radiometer output is 33ms.

Now that the timing circuitry, radiometer and laser system are ready the actual testing can begin. The procedure for acquiring temperature data with the infrared radiometer can be divided into three main process: 1) capturing the thermal fields of the sample on video tape while the sample is being energized, 2) using the image processor to select images for the desired heating times and save the data to files, and 3) extracting the surface temperatures for a desired area of the sample from the intensity-data files created by the image processor.

As the sample is being energized by the laser the temperature changes with time are captured and stored on video tape. Once the resulting thermal history of the sample is stored on video tape, thermal images for three selected times during the quasi-steady state heating period were captured using the IPPLUS image processing system.

The frozen images were analyzed using the line profile function in the IPPLUS analysis toolbox. Line profile analysis allows the user to collect actual intensity or gray scale values along lines with various lengths and in various orientations. This information can then be saved to a floppy disk or to the computer's hard drive. In these tests, the positioning of this line is quite important. As shown in Figure 5.11, this line is positioned horizontally across the center of the specimen and at a length corresponding to its diameter.

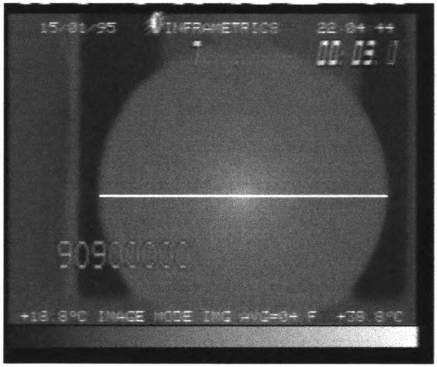

(a.)

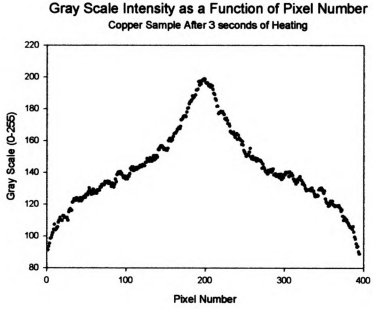

(b.)

Figure 5.11. *(a.) A thermal image of a 5.08 cm diameter copper disk at 3.00 seconds. The horizontal line across the center of the specimen represents the line profile function from the IPPLUS intensity analysis toolbox.* (b.) *The output of the line profile function. Gray scale intensity as a function of pixel number.*

As mentioned in Chapter 3.1.1 and in Appendix B, a calibration can be used to convert the gray scale distributions in Figure 5.11(b.) into the temperature distributions in Figure 5.12. This information is combined with temperature data from other heating times and placed into an input file for the nonlinear sequential estimation program, NLIN. An input file containing this temperature information is shown in Appendix G. It is this input file that NLIN uses to find an estimate of the thermal diffusivity.

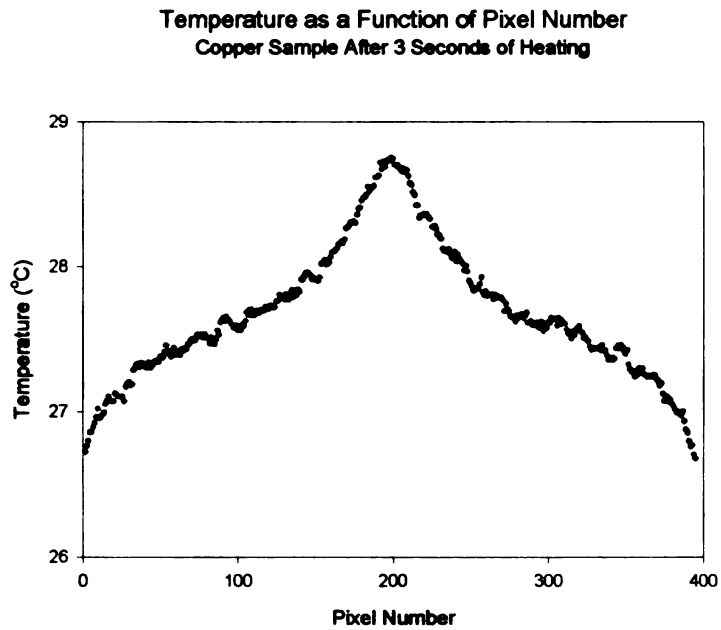

Figure 5.12. *Temperature as a Function Pixel Number. This temperature distribution was obtained using a calibration relating temperature and gray scale.*

5.3 Experimental Results for Verification Materials

The copper and iron samples are measured in this study to verify the general test procedures. The thermal properties of high purity copper and iron materials are well defined in a National Bureau of Standards Journal entitled "The Thermal Conductivity of

Selected Materials." In this journal, Powell, Ho, an Liley state that the thermal conductivites of high purity copper and iron at 300K are 397 W/mK and 80 W/mK respectively. These recommended values are thought to be accurate to within ±3 percent at room temperature. The values of the thermal diffusivities were extracted from the thermal conductivites using the published ρC_p values (Copper $\rho C_p = 3.349 \times 10^6$ J/m^{3}K , Iron $\rho C_p = 3.517 \times 10^6$ J/m^{3}K)[Incropera and Dewitt, 1991]. Based on this calculation, thermal diffusivities of the copper and iron were determined to be 115.94×10^{-6} m^2/s and 22.74×10^{-6} m^2/s respectively.

5.3.1 Experimental Results for Copper

Several tests were conducted on the copper sample. Variations in these tests were used to see how effects such as natural convection and radiometer spatial resolution influenced the experimental results. In the following paragraphs, a description of the experimental results for a typical test is given and is followed by a summary of the results for the copper sample.

The measured transient temperature distributions along a horizontal line across the center of the copper sample after 3.0, 5.0, and 7.0 seconds of heating are shown in Figure 5.13. These times were selected to satisfy the quasi-steady state heating assumption. Since the temperature data for the heated area ($0<r<a$), were not used in the development of the mathematical model, the temperature distributions for the corresponding locations are not represented in Figure 5.13. As illustrated by the linear temperature increases with time at specific radial locations, these measured temperatures are characteristic of the quasi-steady state heating period. The program NLIN uses these measured temperature

distributions along with the mathematical model in equation 4.30 to determine the calculated temperatures. These calculated distributions are also plotted in Figure 5.13 as green symbols. The curves for both measured and calculated temperature data, consist of 876 temperature values obtained at three different times and at 292 different radial positions across the diameter of the disk.

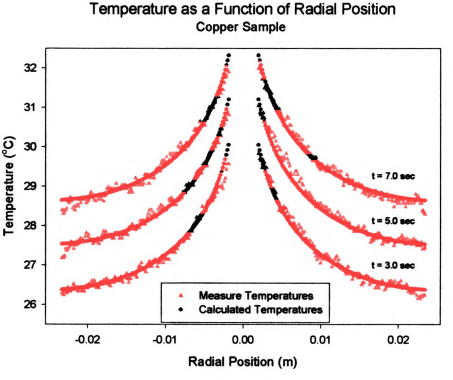

Figure 5.13. *Measured and calculated temperature distributions along a horizontal line across the center of the copper sample. This is sample has a diameter of 5.08 cm and a thickness of 500μm.*

The spatial distribution of the residuals for the three selected times are shown in Figure 5.14. The residuals represent the differences between the temperatures measured by the radiometer and the temperatures calculated NLIN. For this particular experiment,

the standard deviation of the residuals is 0.125°C compared to a temperature rise of 4.0°C across the diameter of the disk.

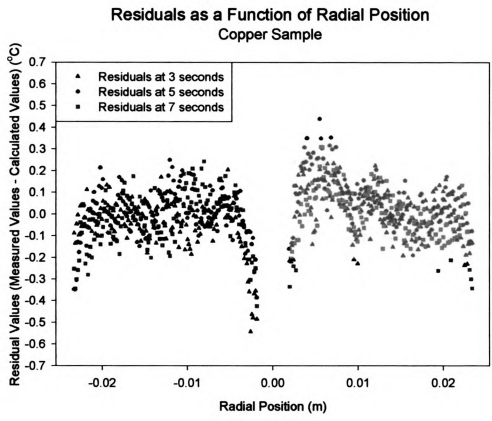

Figure 5.14. *The distribution of residuals across the diameter of the copper disk.*

The residual pattern along the majority of the disk's diameter is random. Such patterns are characteristic of random rather than systematic errors. However, near the center and along the edges of the test sample a trend does seem to exist. In these regions the measured temperatures are consistently lower than the calculated temperatures provided by the mathematical model (i.e. negative residuals). Trends such this result from poor spatial resolution and will discussed further later in this chapter.

In general, Figure 5.15 illustrates the trend of sequential estimation. In this case of the thermal diffusivity is estimated using NLIN. NLIN begins to estimate the desired parameters based on initial guesses and one data observation. Then, another observation is added to the previous set of data and the estimation process is repeated before the next observation is added. The estimated values of parameters are very uncertain during the first 100 observations. However, as the number of observations are increased, the value for the estimated parameter stabilizes. This stabilization in the estimated parameter is a characteristic of sequential estimation and indicates that the observations accurately fit the proposed model.

More specifically, in the case of this test, the 876 radial temperature measurement in Figure 5.13 are the observations. In Figure 5.15 the first 292 data points represent the sequential estimates based on the temperature distribution at 3.0 seconds. The estimates between 292 and 583 illustrate how the parameter changes as a result of adding the information from the temperature distribution at 5.0 seconds. The estimates of 584 and 876 are the result of adding the temperature information captured at 7.0 seconds. At this point, the estimated values are stable and the data is in good agreement with the thermal model.

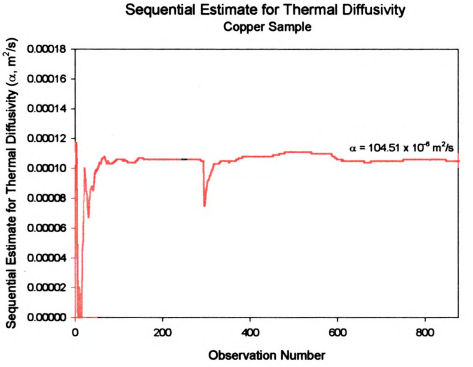

Figure 5.15. *Sequential Estimation for the thermal diffusivity for the copper disk using the non-linear sequential estimation program, NLIN.*

After a series of 42 tests conducted on the copper the average thermal diffusivity was determined to be 100.297 x 10^{-6} m^2/s with a standard deviation of 2.91x10^{-6} m^2/s (coefficient of variation of 0.029). This value is 13.5 % less than the published value reported by Powell, Ho, and Liley in their thermophysical property reference manual. A plot illustrating the magnitude of the difference between the experimentally determined and published thermal diffusivity is shown in Figure 5.16. A numerical listing of the estimated values is presented in Appendix J.

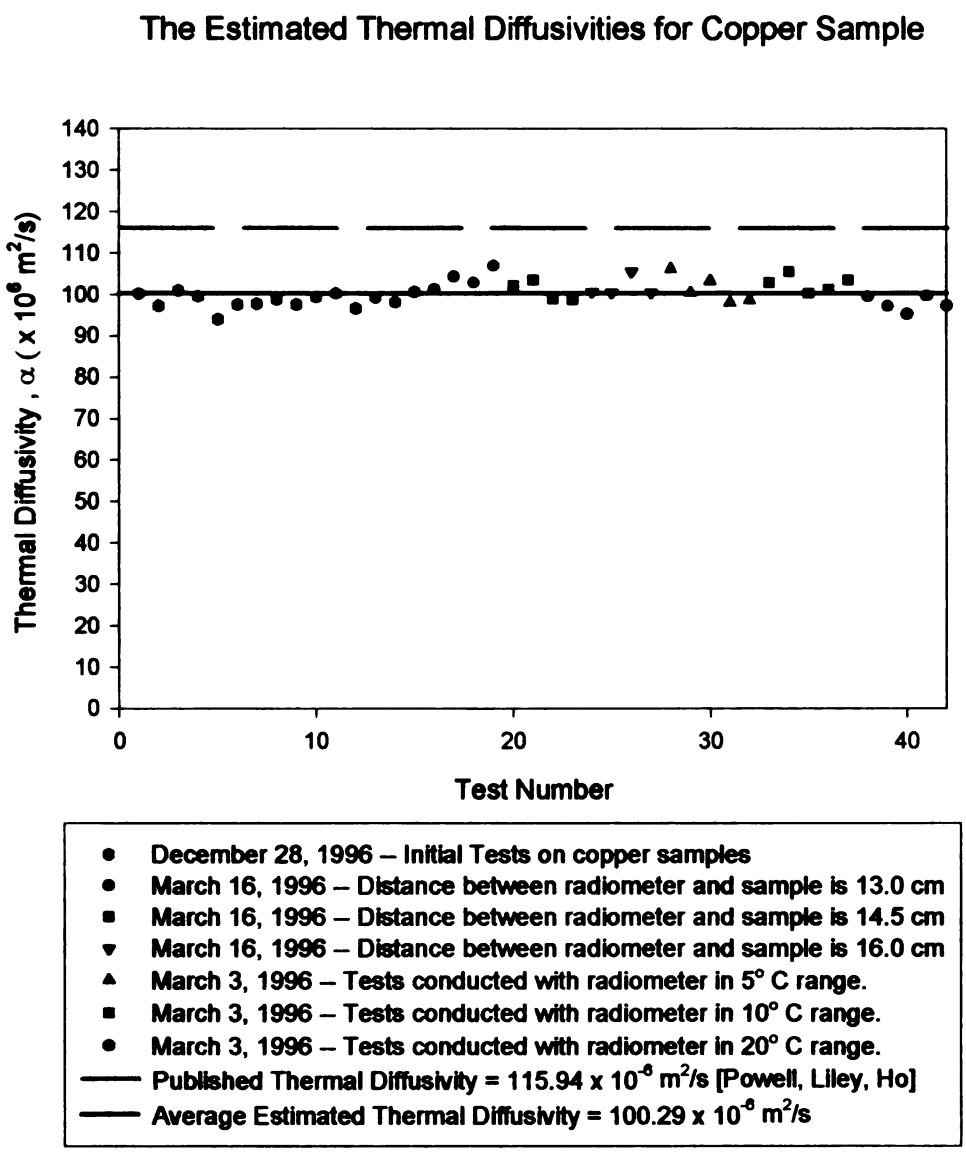

Figure 5.16. *A comparison between the estimated thermal diffusivities and the published values.*

5.3.2 Experimental Results for Iron

The thermal diffusivity of iron is approximately 6 times less than copper. The quasi-steady state heating assumption is valid when the dimensionless time, $\alpha t^2/b$, is greater than 0.5. Knowing this, and with knowledge of the published thermal diffusivity, the first sampling time should occur after 15 seconds of heating. As shown in Figure 5.17, the selected sampling times for this experiment were 20.0, 30.0, and 40.0 seconds.

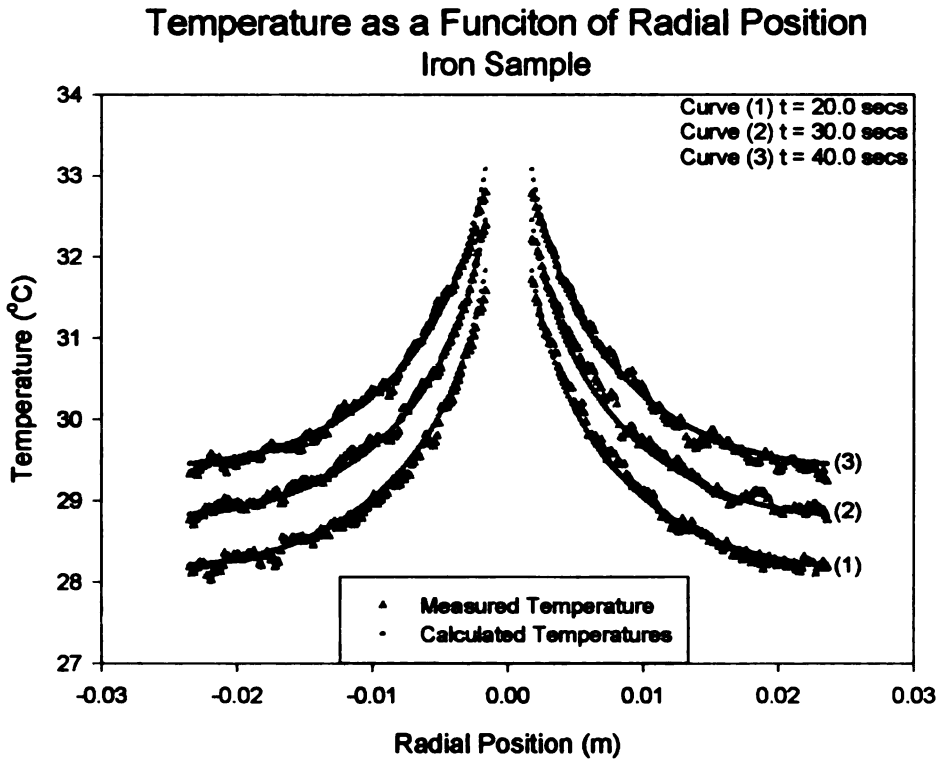

Figure 5.17. *Measured and calculated temperature distributions along a horizontal line across the center of the iron sample. This is sample has a diameter of 5.08 cm and a thickness of 100 μm.*

A significant difference between the iron and copper tests was the magnitude of the heat flux. Under ideal conditions, it is best to operate the radiometer in the lowest possible temperature span settings. This acts to minimize the temperature resolution, and

maximize the thermal sensitivity of the measurements. Since iron does not conduct heat as well as copper, the temperature increases near the center of the specimen are such that the instrument becomes saturated in low temperature span settings. This problem can be eliminated by attenuating the laser such that the power input is reduced. In the case of the iron sample, approximately 730 mW of laser radiation was used to heat the sample during the 40 second period. This was reduced from 3.5 W used to energize the copper sample during the 7.0 second heating time.

The spatial distribution of the residual values for this particular test is shown in Figure 5.18. The standard deviation of the residual values is 0.0944, and the pattern is characteristic of typical gaussian error distribution. As with the copper sample the errors

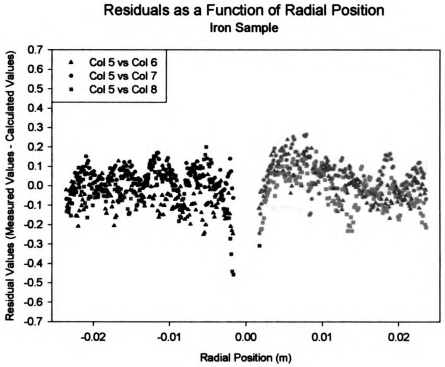

Figure 5.18. *The distribution of residuals across the diameter of the iron disk.*

seem to be randomly distributed along most of the diameter, but there is a systematic behavior near the center and along the edges of the sample.

The low residuals in this experiment are associated with a good fit between the measured data and the mathematical model. This can be visualized in the sequential estimate. As shown in Figure 5.19, the estimate for the thermal diffusivity is relatively constant, even when a small number of observations are considered. In this case the estimate for α_r was 13.98 x 10^{-6} m^2/s.

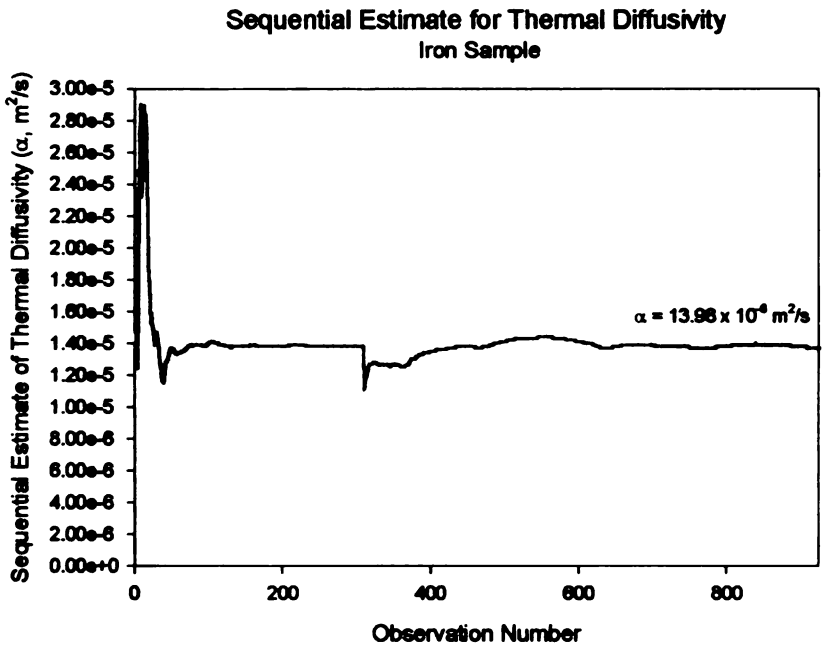

Figure 5.19. Sequential Estimation for the thermal diffusivity for the copper disk using the non-linear sequential estimation program, NLIN.

The average thermal diffusivity for 15 experimental tests on the iron sample is 12.64 x 10^{-6} m^2/s with a standard deviation of 1.34 x 10^{-6} m^2/s (coefficient of variation of 0.10163). This value is 44.4 % less than the published value given by value given by Powell, Ho, and Liley in their thermophysical property reference manual. A plot

illustrating the magnitude of the difference between the experimentally determined and published thermal diffusivity is shown in Figure 5.20.

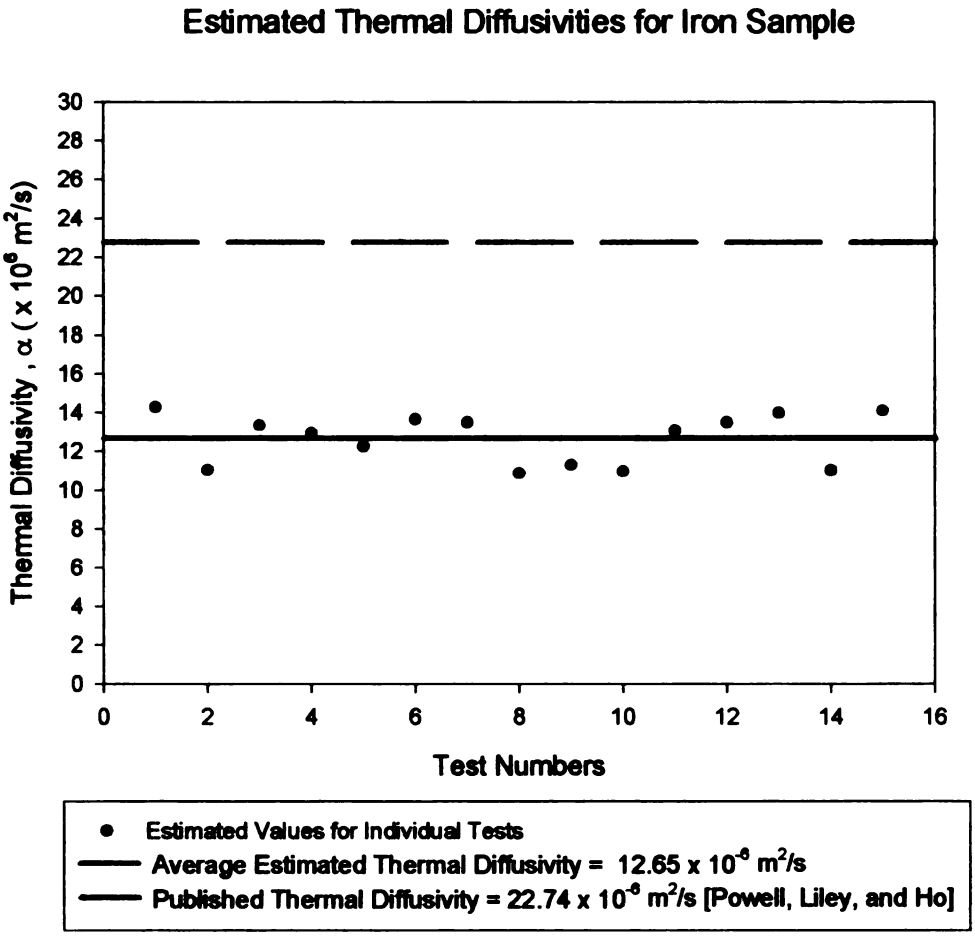

Figure 5.20. *A comparison between the estimated thermal diffusivities for iron and the published values.*

5.4 Experimental Results for CVD Diamond Film

The CVD diamond samples were expected to higher thermal diffusivities than the verification materials. Therefore, the gradients across the sample were low whereas the absolute temperature rise with time was quite high. The laser had to be operated at

power levels which would provide significant temperature differences between the center and outer edges of the sample. Without such gradients, the signal to noise ratio of the IR camera was not large enough to provide reliable results.

Since convection was neglected in the derivation of the mathematical model, high temperature differences between the sample and the surroundings had to be avoided. Evaluation of the heat flow through the sample due to conduction and heat losses due to convection for different temperature difference levels showed that for the diamond specimen an average temperature difference of 15 °C should not be exceeded. In this case, heat loses due to convection amount to approximately 1% of the heat conduction term. This problem can be totally eliminated if the temperature data is sampled at smaller times. The high expected thermal diffusivity of these films allow for the dimensionless time to be greater than 0.5 at times as early as 1.0 seconds. Therefore, in order to minimize the effects of convection, while maximizing the temperature gradient within the sample, the temperature distributions are sampled at 1.0, 2.0, and 3.0 seconds. These temperature distributions are shown in Figure 5.21.

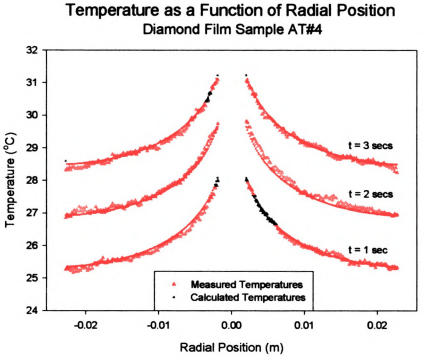

Figure 5.21. *The measured and calculated temperature distributions with the C.V.D. diamond film sample AT#4.*

The spatial distribution of the residuals is shown in Figure 5.22. Similar to the patterns in the verification materials, the residuals for this test are uniformly distributed about zero over the majority of the disk. The standard deviation of these residual values is 0.0827°C compared to a relative temperature difference of 2°C across the surface of the sample.

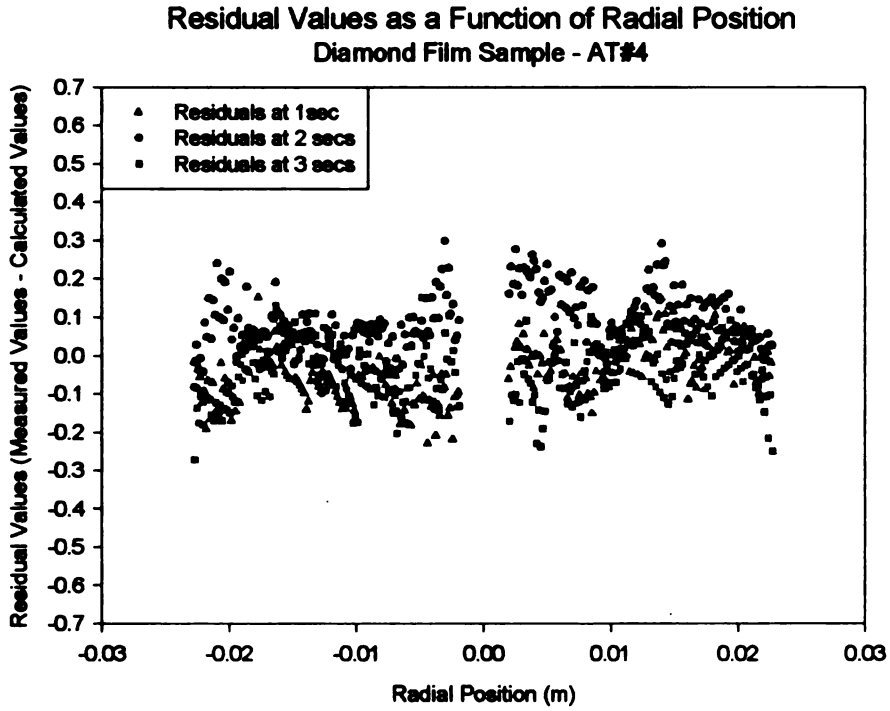

Figure 5.22. *The distribution of residuals across the diameter of the CVD diamond film.*

Figure 5.23 illustrates the sequential estimation for the thermal diffusivity. This estimate has a fairly constant value even when a small number of observations are considered. Similar to the tests with the verification materials, this stability in the estimation proves that the measured temperature distributions are accurately modeled by the mathematical model. In this case, the thermal diffusivity of diamond sample AT#4 was determined to be 387.26 x 10^{-6} m^2/s.

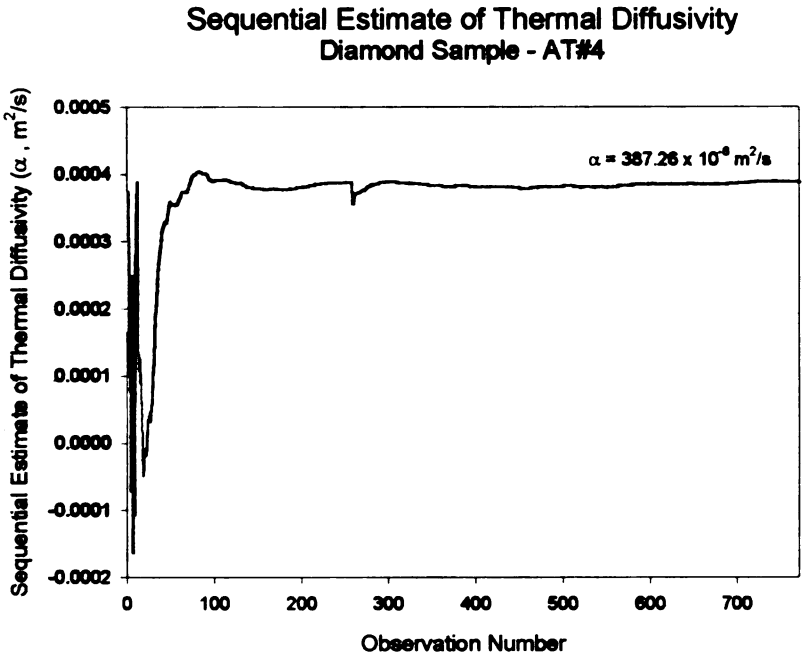

***Figure 5.23.**. Sequential Estimation for the thermal diffusivity for the iron sample using the non-linear sequential estimation program, NLIN.*

The reproducibility of the above test was verified by repeating the same test several times. In this study, 14 tests were conducted on the diamond film sample AT#4, 13 tests on sample ST#192, and 13 tests on sample ST#120. The averages and standard deviations of these tests are 417.50 $m^2/s \pm 23.211 \times 10^{-6}$ m^2/s, 475.29 $\pm$ 19.86 $\times 10^{-6}$ m^2/s, and 401.45 $\pm$ 16.07 $\times 10^{-6}$ m^2/s respectively. The variations of these tests are shown in Figure 5.24 (a.), (b.), and (c.).

Estimated Thermal Diffusivities for Diamond Sample AT#4

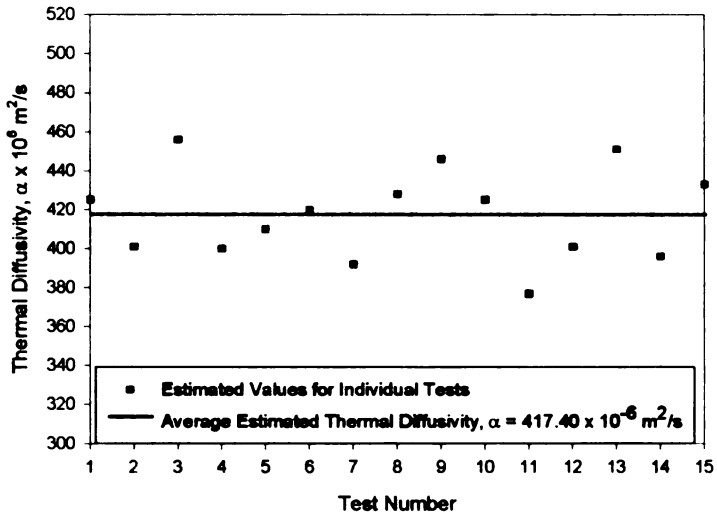

(a.)

Estimated Thermal Diffusivity for Diamond Sample ST#192

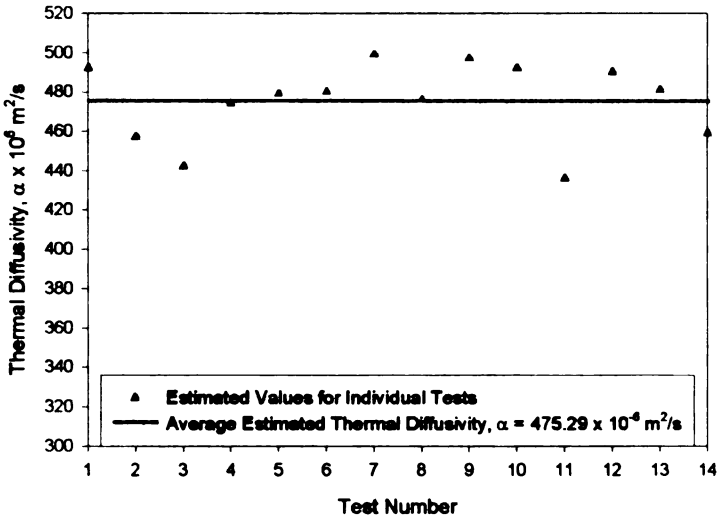

(b.)

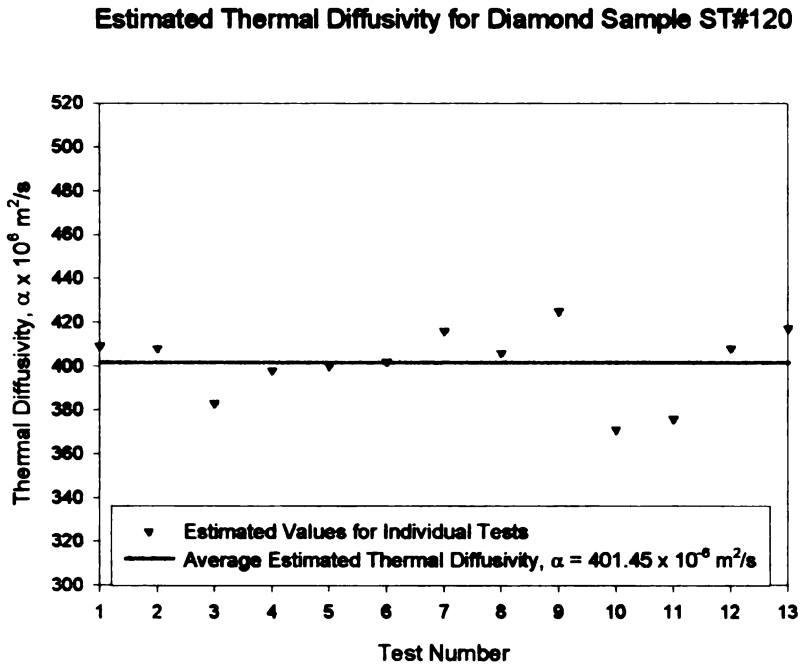

(c.)

Figure 5.24. *The experimental results for CVD diamond film.* ***(a.)*** *Sample AT#4,* ***(b.)*** *Sample ST#192,* ***(c.)*** *Sample ST#120.*

If the estimated thermal diffusivities are multiplied by the measured value of ρC_p [ρC_p = 1.8981 x 10^6 J/m^3 °C (Graebner, 1996)] the thermal conductivity of each of this sample can be calculated. The calculated thermal diffusivities for sample AT#4, ST#192, and ST#120 are 791.5077 W/mK, 902.14 W/mK, and 761.99 W/mK respectively. These estimated thermal conductivities are plotted as a function of thickness and compared estimates by other researchers in Figure 5.25.

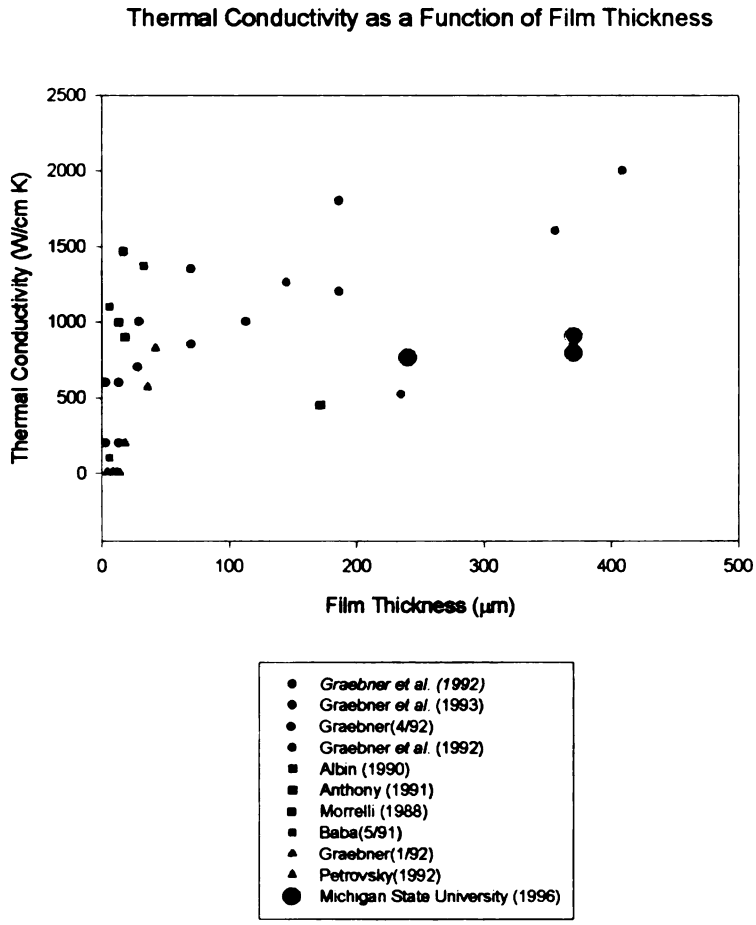

***Figure 5.25** A plot of the estimated thermal conductivity as a function of film thickness. This plot illustrates how the estimate at Michigan State University compare to estimates from other research groups.*

5.4.1. Non-Uniform Thermal Properties of CVD Diamond Film

CVD diamond film grows in a columnar structure with a grain size which starts out very small and typically increases with increasing film thickness as grains with certain orientations dominate [Graebner et al, 1992]. A schematic representation of a diamond film's cross section in Figure 5.26 illustrates this columnar microstructure where the grain size increases with the height above the substrate surface. This current technique involves measuring the thermal conductivity according to the thermal transport in the plane of the

film. To the extent that the heat heat-carrying phonons are scattered at grain boundaries, a thermal conductivity gradient is expected. For example, in recent years J.E. Graebner has done a significant amount of work determining the sources of thermal resistance and measuring the local thermal conductivity of CVD diamond film as a function of height above the substrate surface [Graebner et al, 1992].

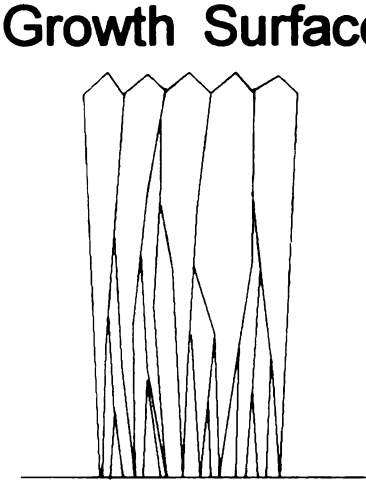

Figure 5.26. *A schematic representation of the cross section of the CVD diamond film. This representation illustrates the columnar microstructure responsible for the increasing grain size with distance for the substrate surface. [Graebner et al, 1992]*

According to the results of Graebner, the thermal transport along the growth surface is different than that of the substrate surface. The developed mathematical model assumes that the temperature through the thickness of the film is uniform. In order to test the model the test procedure in Section 5.4 was repeated for individual tests with the substrate and growth surfaces facing the radiometer.. With the test specimen in these orientations and the other experimental conditions constant, the temperature distributions during the quasi-steady state heating period were acquired. These temperature

distributions, shown in Figure 5.27, illustrate that there is not a significant difference in thermal transport between the two conditions.

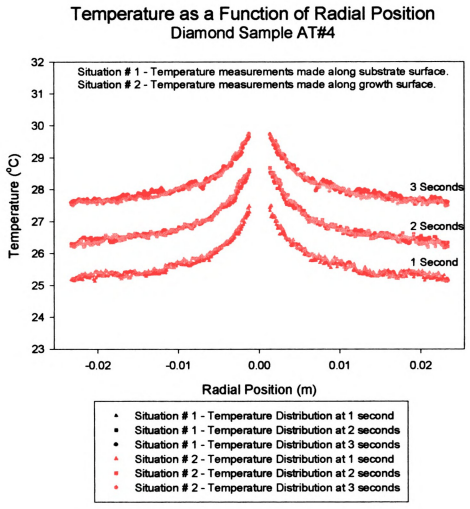

Figure 5.27. *The transient temperature distributions for two tests conducted on diamond film sample AT#4. This figure illustrates that using this measurement procedure, the microstructural characteristics of the growth and substrate surfaces do not contribute appreciable differences in thermal transport.*

As with the temperature distributions, little difference was found in the estimated thermal diffusivity. Hence, the estimated thermal diffusivity using this measurement technique seems to be insensitive to the sample's orientation and any possible variations in

the thru-thickness direction. In 1991, Lu and Swan used their converging wave technique and also found insignificant differences between the results when measuring the temperature along the substrate and growth surfaces.

5.5 Experimental Uncertainty

The experimental uncertainty is a measure of the accuracy of the method used in determining the thermal diffusivity and accounts for uncertainties in quantities such as temperature and radial position. It acts as a global uncertainty which is driven by the precision with which all of the experimental parameters can be measured [Herr, 1993]. The uncertainty in the measurement of the thermal diffusivity is determined from the expression,

$$w_\alpha = \left[\left(\frac{\partial \alpha}{\partial T} \Delta T \right)^2 + \left(\frac{\partial \alpha}{\partial r} \Delta r \right)^2 + \left(\frac{\partial \alpha}{\partial t} \Delta t \right)^2 + \left(\frac{\partial \alpha}{\partial \beta_1} \Delta \beta_1 \right)^2 + \left(\frac{\partial a}{\partial a} \Delta a \right)^2 + \left(\frac{\partial b}{\partial b} \Delta b \right)^2 \right]^{1/2} \quad (5.1)$$

where the terms $\partial\alpha/\partial\xi$ are the sensitivity coefficients determined from equation 4.27 and the $\Delta\xi$ terms are the estimated errors in the measurements. The experimental uncertainty is calculated for the conditions employed when measuring the properties of the CVD diamond film. The experimental parameters, their uncertainties and their corresponding contributions to the uncertainty of the thermal diffusivity are present in Table 5.1.

Experimental Parameter (ξ)	Estimated Uncertainty in Parameter ($\Delta\xi$)	Contribution to the uncertainty in the thermal diffusivity (m^2/s)
a = 0.0005 m Heating Diameter	Constant with no uncertainty	0
b = 0.0254 m Sample Diameter	Constant with no uncertainty	0
β_1 Laser Effect Term	Estimated Value	0
β_3 Initial Temperature	Estimated Value	0
r = 0.0254 m Radial Location	Δr = 0.000282 m	3.2258×10^{-6} m^2/s
t = 2.0 s Time Indication	Δt = 0.0303 s	5.0545×10^{-6} m^2/s
T(r,t) = 30 °C Radial Temperatures	$\Delta T(r,t)$ = 0.11°C	35.48×10^{-6} m^2/s

Table 5.1 *Experimental Parameters, their estimated uncertainties and the corresponding contributions to the uncertainty of the thermal diffusivity.*

The experimental parameters, "a" and "b", correspond to the diameter of the heated region and the sample diameter respectively. These parameters are constants which are entered directly into the input file of the NLIN program and are ignored in this uncertainty analysis. The parameters β_1 and β_3 are estimated along with the thermal diffusivity and uncertainties in these values are ignored. The uncertainty in "r" results from improper radiometer and sample alignment causing spatial distortions and was determined to be 0.000282 m. Improper alignment causes errors in the assignment of radial position to individual temperature measurements. This value was selected to represent a worse case scenario in which the assigned radial position was off by 2 pixels (i.e. 0.0508 m sample dissected into 360 datum points, each pixel represents 0.000141 m). The uncertainty in "t" is related to the timing resolution of the video timer and the

delay associated with the LabVIEW program used to externally initiate timing. Since the frame rate of the radiometer's output is 30 Hz, the uncertainty in "t" results from the delay in the LabVIEW program causing the timer's initiation to be delayed by one frame. Under this worst case scenario, the uncertainty in "t" is 0.0303 seconds. The uncertainty in the radial temperature measurements relies on the accuracy of the radiometer. The radiometer's accuracy was determined by analyzing a isothermal and constant temperature disk. In this study, temperatures fluctuations in time at specific locations were measured. A typical plot of the temperature at one point as a function of time is shown in Figure 5.28. From a series of seven similar tests these fluctuations produced an average standard deviation of 0.11 °C. It is this value that is chosen to represent the accuracy of the radiometer. Based on these initial tests, it is believed that these fluctuations are a strong function of the operating conditions of the radiometer (i.e. the radiometer's temperature range and image average settings).

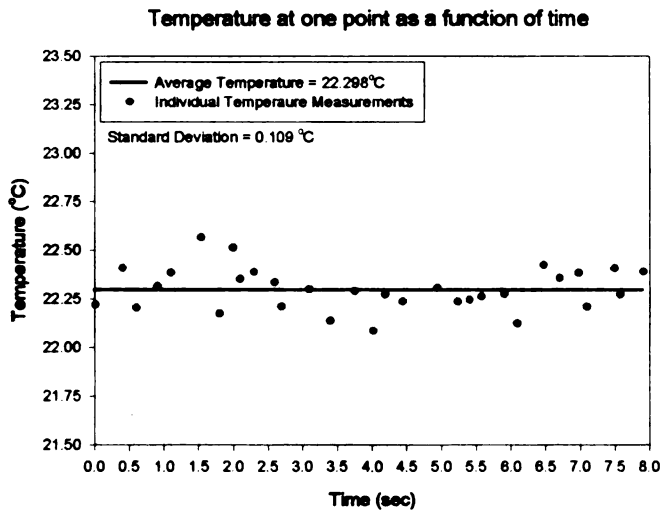

Figure 5.28. *Temperature fluctuations at one specific location on a isothermal and constant temperature sample as a function of time. The standard deviation of these fluctuations are used to represent the accuracy of the radiometer.*

By substituting the values presented in Table 5.1 into equation 5.1 the calculated experimental uncertainty for the in plane thermal diffusivity of CVD diamond was determined to be $\pm 17.47 \times 10^{-6}$ m^2/s. Since this value is approximately equal to the average standard deviation of the experimental results ($\sigma_{avgerage} = 19.71 \times 10^{-6}$ m^2/s) , it can be assumed that the errors in the measured experimental parameters are accurately modeled. The major contribution to the calculated uncertainty resulted from errors in temperature measurement.

The difference between the experimental uncertainty and the calculated uncertainty for both the copper and iron samples were significantly different. The major difference in the uncertainty model between the tests conducted on the diamond, iron and copper samples results from the times at which the data was sampled. As the heating time is increased, the effect of errors in the measured temperatures decreases while the effect of errors resulting from misrepresented radial positions are magnified. In this case, the calculated uncertainty for the copper and iron tests were determined to be 13.90×10^{-6} m^2/s and 15.87×10^{-6} m^2/s respectively. Although these uncertainties are significantly higher than the experimental uncertainty, it is interesting to note that the calculated uncertainties closely approximate the measured uncertainty if errors in radial location are ignored.

5.6 Discussion of Experimental Results

The experimental results using this measurement technique are not very encouraging. Based on the tests conducted on the copper and iron verification samples, it is clear that the current procedure underestimates the thermal diffusivity.

The magnitude of the discrepancy seems to vary based on the thermal properties of the test specimen. For the copper sample, there is a 15.2 % difference between the experimental determined thermal diffusivity and the published value. This difference between estimated thermal diffusivity and the published value is 44.4% on tests conducted on the iron sample. The physical dimensions of the two samples are identical and the experimental techniques vary only as a result of the material's thermal diffusivity. In order for the data to be sampled during the quasi-steady heating period, for example, the sampling times and the amount of applied heat flux must be changed based on the test material.

The estimation process is driven by the measured temperatures. The accuracy of the estimation depends on how accurately these temperatures are measured. It was determined during this research that this accuracy is hindered by systematic errors caused by the spatial resolution of the radiometer. This systematic error causes the data to be "blurred or averaged " about a specific region.

This averaging phenomenon can be illustrated by examining the infrared image in Figure 5.29. In this Figure, a test specimen with two thin fins attached to a flat surface is placed in the field of view of the radiometer. The background temperature on the left hand side of the infrared image corresponds to the ambient conditions within the laboratory. To illustrate this blurring function, an ice bath was placed on the right hand

side of the infrared image reducing the background temperature. Although the two fins are the exactly the same size, the addition of the ice bath causes an apparent difference in their dimensions.

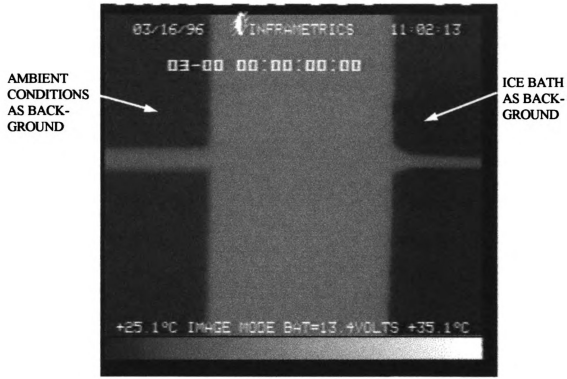

Figure 5.29. *An infrared image of a flat test specimen with two thin fin attached to the surface. This image is used to illustrate the blurring or averaging phenomenon that causes systematic errors in the measured temperatures*

More significantly, for the thermally diffusivity tests recently conducted, the averaging phenomenon causes an apparent temperature difference between the two fins as shown in Figure 5.30. Using the test configuration described above, the temperature distribution along the centerline of fins is obtained and the influence of the fins can be visualized.

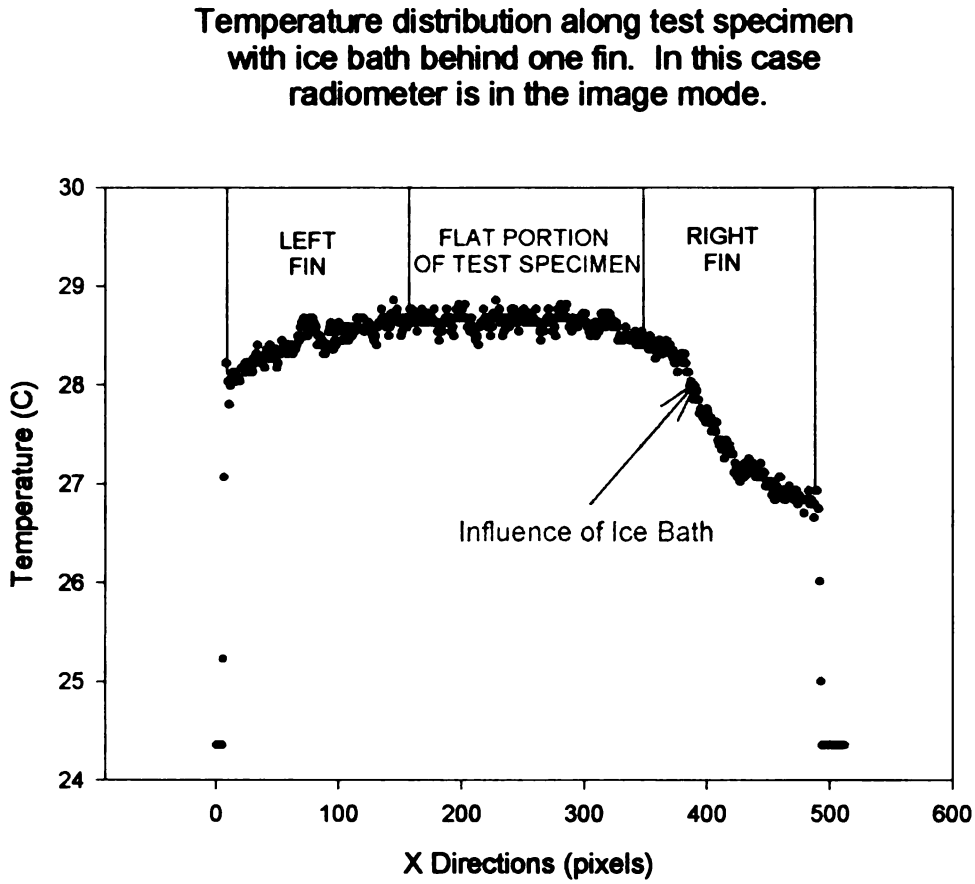

Figure 5.30. *An illustration of the apparent temperature difference caused by the additional of the icebath to the background of the right hand side of the infrared image.*

Problems such as those in Figures 5.29 and 5.30 are caused by the radiometer's spatial resolution. These problems also help to explain the discrepancies between the estimated and published thermal diffusivities. It is clear that the averaging phenomenon causes apparent temperature differences when the temperature of the surrounding area is significantly different from the measured location. Although the surrounding areas on the test sample are not significantly different than those at the measured location for the

thermal diffusivity tests, they still have an influence. The influence of the surrounding areas become more significant as the temperature gradient along the diameter of the sample increases. Based on this argument it seems logical that the temperature measurement errors would have a larger influence on the estimated thermal diffusivity for samples with smaller thermal diffusivities.

In estimating the thermal diffusivity we depend on the imaging system to have a very small spatial measurement resolution. The radiometer's spatial resolution and the tests conducted to measure it are discussed in detail in chapter 3.1.1. For example, in the current experiments a 2 inch diameter sample is positioned such that the entire radiometer field of view is used. In this case, the radiometer is not configured with external optics and positioned at a working distance approximately 15 cm from the sample. As the test is being conducted the image is broken into many discrete points. These discrete points are often called datum points or instantaneous field of views (detector size projected on the object). Each datum represents a location and local image intensity and is considered a pixel. In one horizontal line scan there are 364 pixel locations. Therefore, for the 2 inch sample a measurement spatial resolution of 140 μm is required. As shown in Figure 3.6, the slit response function for this resolution is approximately 70%. As a result, the required resolution is such that details can be discerned, but accurate temperature measurements can not be inferred.

Chapter 6

Summary and Conclusions

The goal of this research was divided into two main objectives. The first objective was to develop the capabilities of an experimental system that could be used to measure the thermophysical properties of CVD diamond film. The second objective was to demonstrate the use of this utility. In this case, the newly developed experimental techniques were combined with existing analytical tools to determine the thermal diffusivity of copper, iron, and diamond samples. Although this research is driven the measurement of CVD diamond film, the copper and iron samples were measured validate the experimental procedures.

The developed experimental system consists of a Nd:YAG laser, two infrared temperature measurement systems, a data acquisition and instrument control system, and

laser diagnostic equipment. Together this system provides an optical, non-contact, and non-destructive means of heating and temperature measurement.

As the heating source the Nd:YAG laser offers a great deal flexibility. Without the use of external optics, this laser produces a beam 0.7 mm in diameter with a maximum power of 15.5 Watts (power density ~ 4kW/cm^2) The laser's power can be attenuated optically using beamsplitters. These beamsplitters offer a 50% reduction in beam intensity when orientated at a 45° angle incident to the incoming laser beam. Therefore, if both beamsplitters are used the laser's power can be reduce by 75%. Further optical attenuation can be achieved through the use of neutral density filters. When using these neutral density filters, however, care must be taken since they have a low and unknown damage threshold.

Major reductions in laser power can also be achieved by adjusting the lamp current. This method is not recommended since large reductions in lamp current (i.e. greater that ~ 2-3 amps) cause thermal changes with the lamp housing and often cause deterioration in the beam quality (i.e. cause high order modes in the beam profile or reductions in beam stability).

The spatial distribution of radiation is easily modified through the use of optical components. Although the available optics only allow us to expand the beam, form a line of uniform radiation, or focus the radiation to a point, the possible spatial distributions are only limited by the imagination of the user.

Two methods are available for controlling the temporal distribution of radiation. Internal Q-Switching allows for short, high intensity bursts of energy to be deposited along the surface at rates between 100 Hz and 80kHz. Externally, the beam can be

chopped at rates as high a 100 Hz using the Uniblitz shutter system. The use of this shutter is limited by electrical problems within the drive control and because of the low damage threshold of the shutter.

In order to gain a thorough understanding of the characteristics of the laser beam and optimize the laser for a particular application, laser beam diagnostic tools were developed. These newly developed tools allow for the measurement of the beam's diameter, energy, power, profile, and temporal dependence.

Temperature measurements can be made with two infrared measurement systems. These systems offer a great deal of temperature information in time and/or space. The Inframetric's thermal imaging system has the ability to capture entire thermal events at 30 Hz or temperature distributions along one line at 8 kHz. The EG&G infrared point detector has the ability to make temperature measurements of one point at 2 MHz.

Regardless of the measurement technique the data has to be processed. The output of the thermal imaging system is a standard 8-bit video output, and for the first time it was demonstrated that a general image processing system (IPPLUS) could be used to analyze the data.

Similar to other transducers, the output of the point detector is a voltage. This output can be recorded using the newly developed data acquisition and instrument control system. This system contains two data acquisition boards programmed with LabVIEW. The AT-MIO16F board has multifunctional analog, digital and timing I/O capabilities, and allows for data at 8 differential input channels to be collected at a maximum rate of 200kHz . The EISA-A2000 board can be used to digitize signals resulting from high speed events and is used when the data acquisition capabilities of the AT-MIO-16F are not

sufficient. The board can sample one channel at 1 MHz, two channels simultaneously at 500 kHz, and four channels at 250 kHz.

After the experimental components were characterized the utility of the system was demonstrated. In these experiments, temperature measurements were made with the infrared imaging system and the circular samples were energized in the center with the Nd:YAG laser. The IPPLUS image processing system was used to capture thermal events at times consistent with the quasi-steady state heating period. The temperature distribution across the center of the sample was located and extracted with the image processing system. This information was then used along with the non-linear sequential estimation program, NLIN, to estimate the thermal diffusivity.

The test results on the copper and iron samples were quite discouraging. The average experimentally determined thermal diffusivity and standard deviation for the copper and iron samples are listed in Table 6.1. When compared to the published values, it is clear that this experimental technique has tendency to underestimate the thermal diffusivity.

Sample Material	Number of tests	Average Estimated α [m^2/s]	Standard Deviations [m^2/s]	Published α[m^2/s]	Percent Difference
Copper	42	100.297×10^{-6}	2.91×10^{-6}	115.94×10^{-6}	13.5 %
Iron	15	12.64×10^{-6}	1.34×10^{-6}	22.74×10^{-6}	44.4 %

Table 6.1. *The estimated thermal diffusivity for experimental tests conducted on copper and iron samples.*

As for CVD diamond, the average experimentally determined thermal diffusivity and standard deviation for three samples are listed in Table 6.2.

Diamond Sample	Average Sample Thickness (μm)	Number of tests	Average Estimated α [m^2/s]	Standard Deviations [m^2/s]
AT#4	370	14	417.50×10^{-6}	23.211×10^{-6}
ST#192	370	13	475.29×10^{-6}	19.86×10^{-6}
ST#120	240	13	401.45×10^{-6}	16.07×10^{-6}

Table 6.2. *The estimated thermal diffusivities for experimental tests conducted on three CVD diamond samples.*

If the estimated thermal diffusivity values are combined with published density and specific heat values the thermal conductivity can be extracted [Graebner, 1996]. Based on this calculation, the thermal conductivity values are 791.5077 W/mK, 902.14 W/mK, and 761.99 W/mK. A plot of these values as a function of thickness is shown in Figure 6.1. Examination of this plot illustrates that these estimates seem to be lower than the established trend. The most direct comparison between these estimates can be made wth the results of Graebner. In this 1992 test, Graebner, Jin, Herb, Kammlott, and Gardinier determined that the thermal conductivity of a 355 μm thick diamond sample was approximately 1500 W/mK. Although the absolute accuracy of the Graebner estimate is unknown, it seems to verify that our experimental technique may underestimate the thermal diffusivity for CVD diamond films.

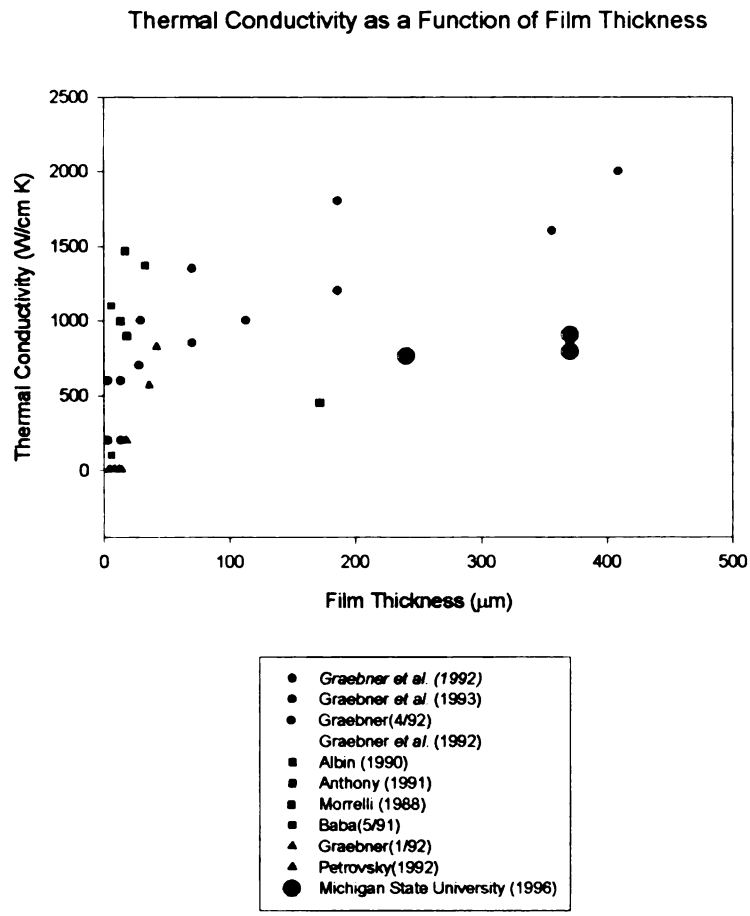

Figure 6.1. *Thermal diffusivity as a function of film thickness. This plot illustrates how the estimates at Michigan State University compare to the estimates made by other research groups.*

List of References

Annamalai, N.K., Sawyer, J., Karulkar, P., Masyara, W., and Landstrass, M., "Silicon-on-Diamond Field-Effect Devices," Proceedings of the 3rd IUMRS International Conference on Advanced Materials, Toyko, Japan, August 1993

Albin, S., Winfree, W.P., and Crews, B. Scott, "Thermal Diffusivity of Diamond Films Using a Pulsed Laser Technique.", J. Electrochem. Soc., Vol. 137, 1990, No. 6.

Baba, K., Aikawa, Y., and Shohata, N., "Thermal Conductivity of Diamond Films" J. Appl. Phys. Vol. 69, 1991, No. 12.

Beck, J.V. "Parameter Estimation Concepts and Modeling: Flash Diffusivity Application." June 1996

Beck, J.V., and Arnold, K.J., Parameter Estimation in Engineering and Science, John Wiley and Sons, 1977.

Burleigh, D.D., Kuhns, D.R., Cowell, S.D., and Engel, J.E., "Thermographic nondestructive testing of honeycomb composite structural parts of the Atlas space launch vehicles." Thermosense SPIE Volume 2245, pp. 152-163, June 1994.

Dereniak, E.L., Crowe, D.G., Optical Radiation Detectors, John Wiley and Sons, 1993

Graebner, J.E., Jin, S. Kammlott, G.W., Bacon. B., Seibles, L. and Banholzer, W.,"Anisotropic Thermal Conductivity in Chemical Vapor Deposited Diamond.", J Appl Phys., Vol 72, 1992, No. 11

Graebner, J.E., Jin, S. Kammlott, G.W., Herb, J.A., and Gardinier, C.F., "Uncertainty High Thermal conductivity in Diamond Films.", Appl Phys. Lett., Vol.. 60, 1992, No. 13.

Graebner, J.E., Jin, S. Kammlott, G.W., Herb, J.A., and Gardinier, C.F., "Large Anisotropic Thermal Conductivity in Synthetic Diamond Films.", Letters to Nature, Vol. 359, 1992, p. 401.

Graebner, J.E., Mucha, J.A., Siebles, L., and Kammlott, G.W., "The Thermal Conductivity of Chemical-Vapor-Deposited Diamond Films on Silicon.", J. Appl. Phys., Vol. 71, 1992, No. 7.

Graebner J.E., Reiss, M.E., Seibles, L., Hartnett, T.M., Miller, R.P., Robinson, C.J., "Phonon scattering in chemical-vapor-deposited diamond", The American Physical Society, Vol. 50, 1994, No. 6.

Graebner J.E., "Measurements of the Specific Heat and Mass Density in CVD Diamond" Diamond and Related Materials , April 12, 1996

Halmsten, P., and R. Houis, "High resolution thermal scanning for hot strip mills." Thermosense SPIE Volume 1313, pp. 322-331, June 1990.

Hamrelius, T.E., "Accurate temperature measurement in thermography. An overview of relevant features, parameters and definitions." Thermosense SPIE Volume 1467, pp. 448-457, June 1991.

Hecht, Jeff, The Laser Guidebook, 2nd Edition, Tab Books, Blue Ridge Summit, PA (1992).

Hey, Tony and Patrick Walters, The Quantum Universe, Cambridge University Press, Cambridge, UK (1987).

Holst, Gerald C., Testing and Evaluation of Infrared Imaging Systems, JCD Publishing Co., Maitland, FL, 1993.

Incropera, F.P., and DeWitt, D.P., Introduction to Heat Transfer, 2nd edition, John Wiley and Sons, 1990.

Jenkins, Francis and Harvey White, Fundamentals of Optics, 4th Edition, McGraw-Hill, New York , NY (1976).

Koechner, Walter, Solid State Laser Engineering, 3rd Edition, Springer-Verlag, New York, NY (1992).

Morelli, D.T., Beetz, C.P., and Perry, T.A., "Thermal Conductivity of Synthetic Diamond Films", The American Institute of Physics, Vol. 60, No. 6, September, 1988.

Powell, R.W., Ho, C.Y., Liley, P.E. , "Thermal Conductivity of Selected Materials", NSRDS-NBS 8, November 25, 1966

Puram C.K., "Measurement of steady and unsteady temperatures using infrared thermography.", Fundamental Experimental Measurements in Heat Transfer ASME1991, HTD-Vol. 179.

Shelmire, Gary, "How to make accurate laser output measurements," Laser Focus World, April 1993

Siegman, A.E., Sasnett, M.W., Johnston, T.F., "Choice of Clip Levels for Beam Width Measurements Using Knife Edge Techniques." IEEE Journal of Quantum Electronics, Vol. 27, No. 4, April 1991

Vorobei, V.V., "Thermoelastic Problems for Monodirectional Fiber Composites Exposed to Pulse Thermal Action.", Soviet Applied Mechanics, Vol. 22, 1986.

Wilson, J. and J.F.B. Hawkes, Optoelectronics: An Introduction, 2nd Edition, Prentice Hall, New York, NY (1989).

Wright, R.E., Chirh K. Puram, and Kamran Darabeigi, "Desirable features of an infrared imaging system for aerodynamic research." Thermosense SPIE Volume 1682, pp. 315-324, June 1992

Zhu, W., Stoner, R., Williams, B.E., and Glass, J.T., "Growth and Characterization of Diamond Films on Nondiamond Substrates for Electronic Applications.", Proceedings of IEEE, Vol. 79, No. 5, May 1991.

APPENDIX A - LASER THEORY

The physical mechanisms of light emission are subtle and complex. Factors such as the chemical makeup of the light-emitting material, its physical state (solid, gas, plasma), the manner of excitation, temperature and even pressure can affect the kind of light created by incandescent lamps and gas discharges. These effects, however, only hint at the forms of light emission.

Attempts to understand laser emission lead to Plank's radiation law and the dawn of quantum theory. Albert Einstein, who never fully accepted the philosophical implications of quantum theory, conceived two of its most fundamental concepts: the photon (1905) and stimulated emission (1917). Both concepts were crucial to the invention of the laser.

Niels Bohr, the "ardent champion" of quantum theory, constructed the first quantum model of an atom in 1913. Using this model he was able to accurately predict the emission-line frequencies of atomic hydrogen. Soon afterward, Arnold Sommerfeld, Wolfgang Pauli and others made important refinement to the existing model which led to a more complete explanation of line spectra and established a physical foundation for the periodic table of elements.

With further investigation in the 1920's, the Bohr model began to gain a firm theoretical footing. "This help came in the form of Louis de Broglie's particle waves, Werner Heisenberg's matrix mechanics, Schrodinger's wave equation, and Born's probability of wave packets." It took just three decades for quantum theory to become a

new and successful explanation of matter and light. Today, quantum mechanics plays a leading role in our present understanding of the universe.

The Bohr-Sommerfeld model, which consists of negatively charged electrons orbiting around a positively charged nucleus along specific paths called orbitals. The position of these discrete orbitals depend on a complex set of conditions, such as the number of electrons surrounding the nucleus, the number of protons in the nucleus, the electron spin, the presence of nearby atoms, and the existence of electronic and magnetic fields.

Each orbital defines a unique, stationary energy state within the atom. When all of the electrons occupy orbitals that have the lowest potential energies, the atom is said to be in its ground state. At absolute zero all atoms are in their ground state. Electrons can be excited into higher-energy orbitals by absorbing energy in many ways. Some of these methods include the vibrations of elevated temperatures, by collisions with other atoms or free electrons, via chemical reactions with other atoms, or through the absorption of photons.

When electrons are excited into higher orbitals by the absorption of photons for example, they will almost immediately decay back to the ground state. The process usually takes only about 10 ns and happens spontaneously. Spontaneous decay often leads to spontaneous emission of photons with exactly the same frequency as the photons that excited the electrons in the first place. Light created in this way radiates from the atoms in random direction but at well - defined wavelengths called emission lines. These emission lines will intensify as more electrons are pumped into higher orbitals.

In atomic hydrogen, the set of absorption and emission lines that originate and terminate in the ground state (n=1) define the Lyman series of energy transitions (see Figure A1). In this figure arrowheads pointing in both directions indicate that these energy transitions are "two way streets," resulting in either resonance absorption or resonance radiation. When electrons are excited to n=3 or higher orbitals, more than one downward transition is possible. For example, from n=3 the electron could drop straight back to the ground state or go first to n=2 and then to the ground state. Depending on which path is taken, three different photons could result. The more direct route to the ground state generates a single photon with an energy of 12.1 eV, whereas the indirect route might produce two photons in succession: one with 1.88 eV of energy and a second with 10.2 eV.

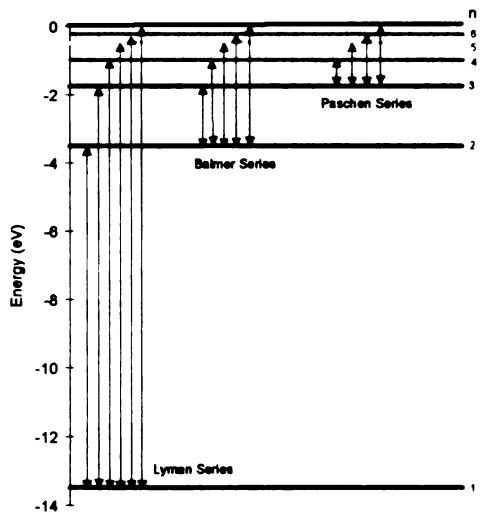

Figure A1. *An energy - level diagram of atomic hydrogen. This figure illustrates the energy transitions that terminate at levels designated by principal quantum numbers, n=1(ground state), n=2, n=3. Upward arrows specify absorption, downward arrows indicate emission. Atomic hydrogen is one of the simplest models, in more complex models levels can split into many sublevels or even continuous bands of allowable energies.* Lasers: Theory and Practice *by J. Hawkes and I. Latimer - 1995]*

The indirect emission process describes a kind of fluorescence in which the energy absorbed by an atom is quickly reradiated at longer wavelengths. The 1.88-eV photon creates the red H_α emission line at 656.3 nm. This line is one of a group of transitions called the Balmer series. As the number of orbiting electrons grows through the ranks of the periodic table, so does the intricacy of the orbital transitions.

In any atom, however, some transitions are more likely than others. There are well-established selection rules in quantum mechanics that predict the probable occurrence of a given transition in various circumstances. This is important to know because the likelihood of a transition ultimately determines the strength of an absorption or emission line. Moreover an excited atom sometimes can find itself trapped in an energy state from which a downward transition is unlikely. The atom can linger in this metastable state for microseconds or even milliseconds before decaying to a lower energy level.

The existence of metastable states can upset the thermodynamic equilibrium that normally prevails in atomic systems. If enough electrons get hung up in a metastable state, the population of atoms in this state could exceed the population of atoms in a lower energy state. If this happens, the atoms are said to be in a condition of population inversion. Population inversion is a state which is thermodynamically unstable. Population Inversion is illustrated in Figure A2.

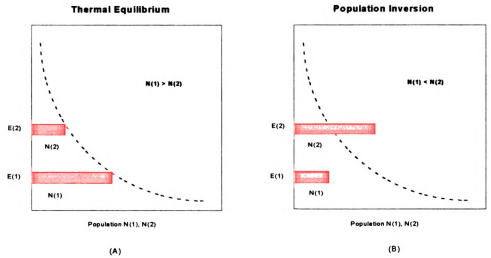

Figure A2. *Populations of a two-energy system (A) in thermal equilibrium and (B) after a population inversion has been produced. [Lasers: Principles and Applications by J. Wilson and J Hawkes - 1987]*

Population inversion is an avalanche waiting to happen. When more energy is stored within the atoms at a higher state than at a lower one, the capacity of gain exists. In fact, lasers depend on population inversion for their gain. All that is needed is some kind of stimulus to set the downward transition in motion. It was Einstein who uncovered the stimulus for lasers some 40 years before Schawlow and Townes described how it could be put to use. Before Einstein offered a powerful thermodynamic argument for stimulated emission, stimulated absorption and spontaneous emission were the only modes known for energy transitions within an atom.

Unlike spontaneous emission, in which an electron randomly decays to a lower energy level and gives off a photon in the process, stimulated emission is neither spontaneous nor random (See Figure A3). With stimulated emission an electron is

induced to decay by a photon that has the same energy as the transition energy of the electron. When the electron encounters such a photon, it immediately decays and generates another photon with exactly the same energy as the photon that triggered the downward transition. As a result, not only do the two photons have the same energy, frequency, and wavelength, they are headed in the same direction and have the same polarization and phase.

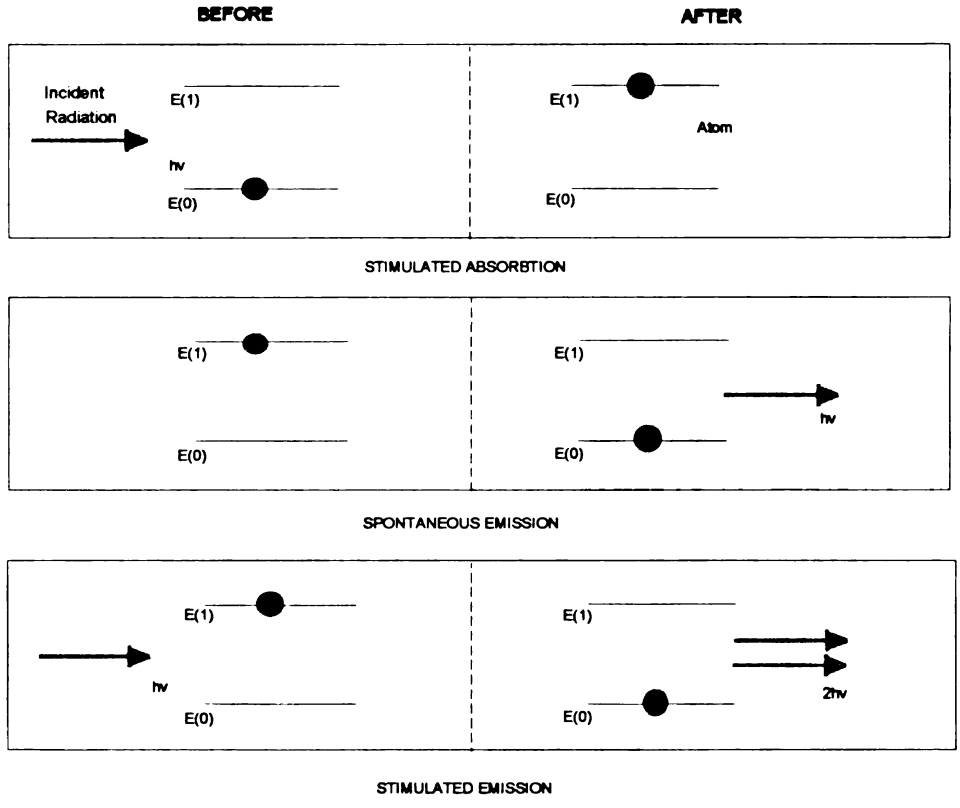

Figure A3. Stimulated absorption of a photon destroys the photon (top) , Spontaneous emission creates a random photon (middle), and stimulated emission creates a photon identical to the stimulating photon(bottom). [Optoelectronics: An Introduction by J. Hawkes and J. Wilson - 1989].

With the concept of stimulated emission, a simple sketch of how a laser functions at the quantum level can be developed. The first step is to attain a population inversion in the atoms of the laser medium. This requires enough energy to pump more atoms into the

metastable state than there are in the lower energy state. Once this population inversion is obtained the spontaneous decay of electrons from the metastable level will create photons with just the right energy to cause an avalanche of stimulated emission.

Within the laser medium there is a mixture of spontaneous and stimulated emission, but it is not a laser in the customary sense of the word because light radiates in all directions. Nevertheless, the medium will have a small gain while the population inversion persists, and the radiation will have laser like qualities. But if the radiation can be partly contained with optics (usually two mirrors in various configurations), then the stimulated emission will be extracted from the medium much more efficiently. One of the most common ways to contain this radiation is to place the laser medium inside a Fabry-Perot interferometer (see Figure A4).

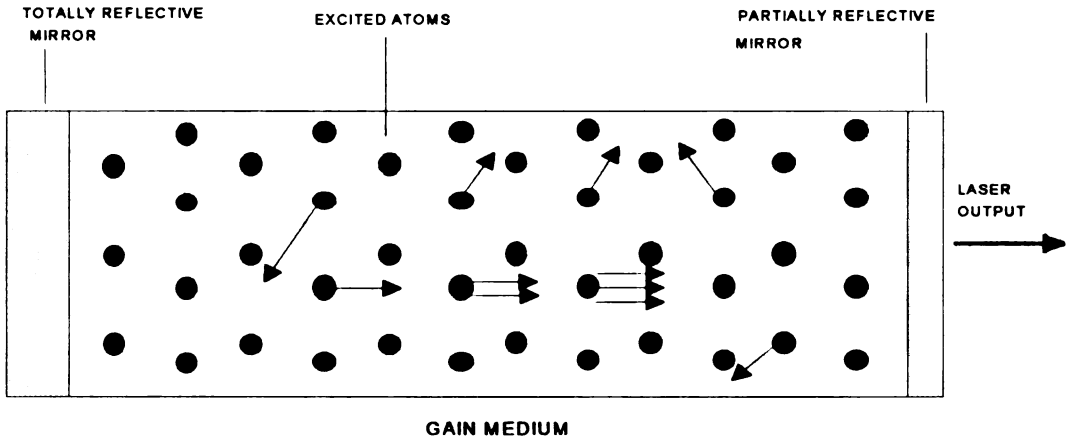

Figure A4. Placing a laser medium in an optical cavity formed by two parallel mirrors effectively stretches the medium to many to times its actual length and creates a feedback environment for efficient amplification of the simulated emission.

The Fabry-Perot consists of two parallel mirrors placed some distance apart. Some of the light trapped inside this optical cavity will experience multiple reflections as it bounces back and forth between the mirrors. In this condition the light is said to be resonant with the cavity.

This resonant condition transforms the interferometer into a highly selective filter. At resonant wavelengths, the reflectivity inside the cavity can be very high, creating an excellent feedback environment for the laser gain medium. Because a portion of the spontaneous and stimulated light inside the cavity passes back and forth through the medium, the medium is effectively stretched many times its actual length. And with each pass, more photons are stimulated into existence.

If the population inversion is high enough to overcome all the energy loss inside the cavity, the so-called threshold condition will be met and lasing will begin. To allow light out of the laser cavity, one mirror is usually made partially reflective. Because laser light consists mostly of the stimulated emission generated with each pass through the gain medium, it is coherent and highly directional.

Unlike the light from a conventional source, such as incandescent lamps or gas discharges, laser light is exceptionally monochromatic (possessing only one color, or more specifically, a specific wavelength in the electromagnetic spectrum). A Nd:YAG laser, for example, is about 10 million times more monochromatic than a common lamp. And because lasers are amplified light sources, their intensities can reach levels many orders of magnitude greater than the sun.

The light from most lasers also diverges very slowly as it propagates through space, a result of its monochromaticity and the multipass cavity design. The real difference between laser light and other forms of radiation is the high degree of phase correlation across the wavefront and in time (This is defined as spatial and temporal coherence, respectively). This means the crests and troughs of the individual wave trains stay in step with each other across the beam and for an extended interval of time.

These unique properties make the laser an indispensable tool for a variety of applications. Some of the most successful laser designs are the result of some of the research conducted by Maiman and Schawalow in the 1960's. v Some of the most successful lasers include gas lasers such as HeNe, CO_2, argon-ion, and HeCd; solid-state lasers such as rudy, Nd:YAG, and Nd:YLF, tunable solid-state lasers such as Ti:sapphire and alexandrite: semiconductor lasers as AlGaAs, InAlGaAs, DFBs, VCSELs, and quantumwells; and liquid dye lasers.

For an example of simulated emission the HeNe laser can be examined. The laser medium consists of a narrow discharge tube filled with a helium-neon gas mixture (A typical ratio for the mixture is 10 helium atoms for every neon atom.). As with standard neon tubes commonly seen in store windows, an electrical discharge excites the gases. Basically, however, the similarity between this advertising mechanism and the laser ends there. In the laser much of the energy of the free electrons created by the electronic discharge is absorbed by the more numerous helium atoms. This is illustrated in Figure

A5.

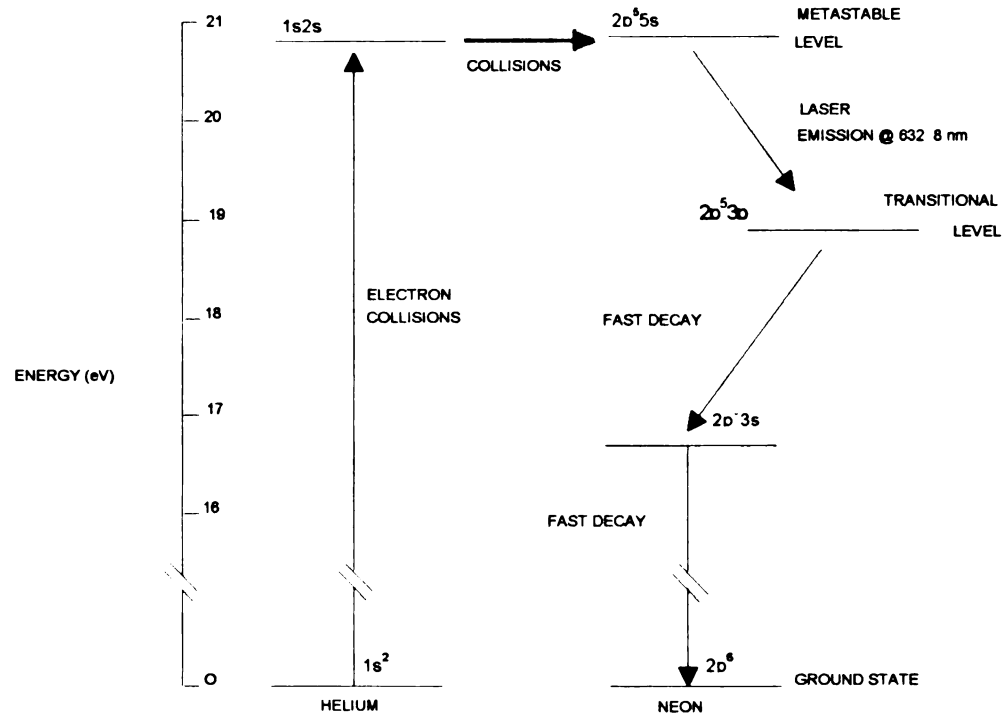

Figure A5. *Simplified energy-level diagram of a HeHe laser operating at 632.8 nm.*

These collisions increase the energy of the helium atoms and pump them into the metastable energy state (1s2s). The energy of this state happens to be identical to a metastable state of neon ($2p^5 5s$). Through collisions between the excited helium atoms and the ground state neon atoms, the helium gives up its energy to the neon, raising it to a metastable state. From this long-lived($\approx$100 ns) energy state, stimulated transitions to a short-lived($\approx$10ns) lower energy state ($2p^5 3p$) will generate laser light at 632.8 nm once sufficient population inversion is achieved between the two states. Neon atoms, the lower energy state, called terminal laser level, quickly decay to an even lower energy state

($2p^5 3s$), from which they quickly decay back to ground state. At this point the process can start all over.

The HeNe laser illustrates one way to create laser light. There are dozens of other methods. Whatever the approach, however, the basic prerequisites for laser light are the presence of metastable states, some mechanism for pumping atoms into the metastable state, a population inversion of atoms in the metastable state, stimulated emission, and some kind of optical feedback to enhance the stimulated emission and control its output. "Without all five of these conditions, a laser would be just another flashlight and electro-optics would be just another branch of optics."

APPENDIX B

Calibration of IPPLUS for Infrared Temperature Measurements

This appendix discusses the steps involved in obtaining a calibration between the IPPLUS image processing system and the Inframetrics thermal imaging system.

EXPERIMENTAL EQUIPMENT

1. A thin (1/8") Aluminum disc 2 inches in diameter
2. Minco disc heater 2" inches in diameter
3. Omega-High Thermal Conductivity Paste
4. Radiometer and Control Unit
5. Video Recorder
6. DC Power Supply
7. IPPLUS image processing system

EXPERIMENTAL PREPARATION

1. Aluminum disc is painted with black paint to improve emissive properties.
2. Minco heater is attached to disc using paste.

EXPERIMENTAL SETUP

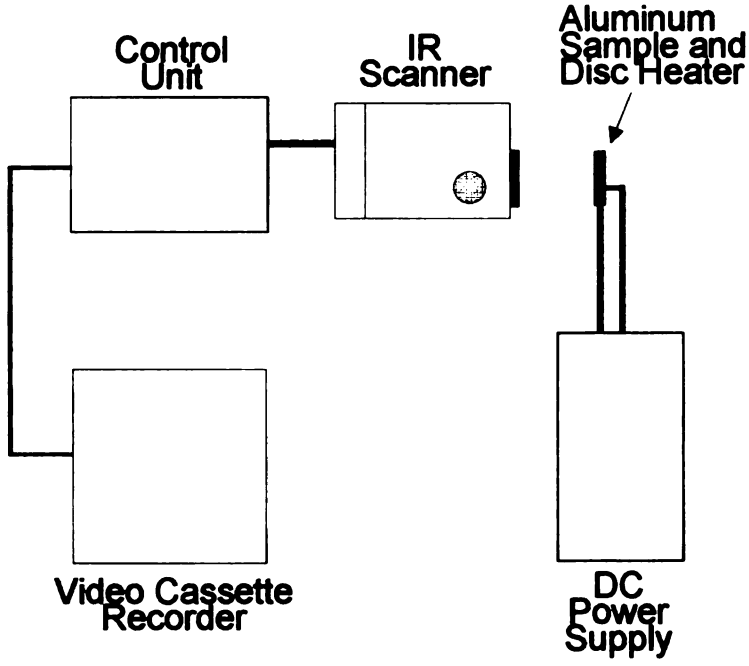

Figure B1. *Experimental Setup*

EXPERIMENTAL PROCEDURE

1. In calibrating the system the radiometer was operated in the point mode. As shown in Figure B2, the crosshairs were placed near the center of the disk and the cursor temperature in the text line was used in the calibration.

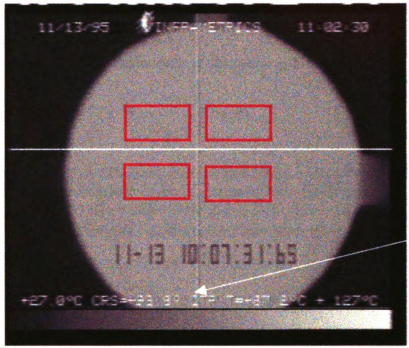

Figure B2. *Camera operated in the point mode. The temperature at the location of the "cross hairs" is indicated in the text line along the bottom of the image.*

2. In the first calibration test the temperature span was set to five degrees and the range was adjusted so the entire field of view was dark. Therefore, initially the temperature of the disk was below the range of the radiometer.
3. Then as the voltage supplied to the heater was slowly increased the output of the radiometer was stored on video cassette. The test continued until the disk temperature exceeded the radiometer's temperature range.
4. The recorded data was then analyzed using the IPPLUS image processing system. As the temperature of the disk slowly increased, thermal fields as shown in Figure B2 were randomly captured.
5. Using the line profile or bit map analysis function of IPPLUS the gray scale intensities of four regions, indicated in Figure B2 with red rectangles, were average and compared with the cursor temperature. If this is done several times throughout the temperature range, a plot of temperature versus gray scale can be developed. Since the output of the radiometer is a standard 8 bit video format, the gray scale intensities

will range between 0 and 255. Therefore, regardless of the temperature setting the output of the radiometer is divided into 256 discrete levels. This being the case, the slope of a gray scale to temperature calibration curve with radiometer in the 20 temperature range is different than the slope of the of a gray scale to temperature calibration curve with the radiometer temperature range at 5 degrees. These differences in slope can be eliminated if the gray scale is plotted as a function of non-dimensional temperature.

6. A non-dimensional temperature was determined based on the minimum and maximum temperature for the particular temperature span setting. For example, in Figure B2

   the minimum temperature T_L=27.0°C
   the maximum temperature T_H=127°C
   and the temperature at the location of the cursor is T = 98°C.

$$\theta = \frac{T - T_L}{T_H - T_L} = .71 \qquad \text{(B.1)}$$

7. This non-dimensional temperature is then plotted as a function of the gray scale intensity and a linear regression can be performed on the data to find a relationship between gray scale and temperature. This plot is illustrated in Figure B3.
8. Steps 1 through 7 are repeated with the temperature span set at 10°C, 20°C, 50°C, and 100°C.

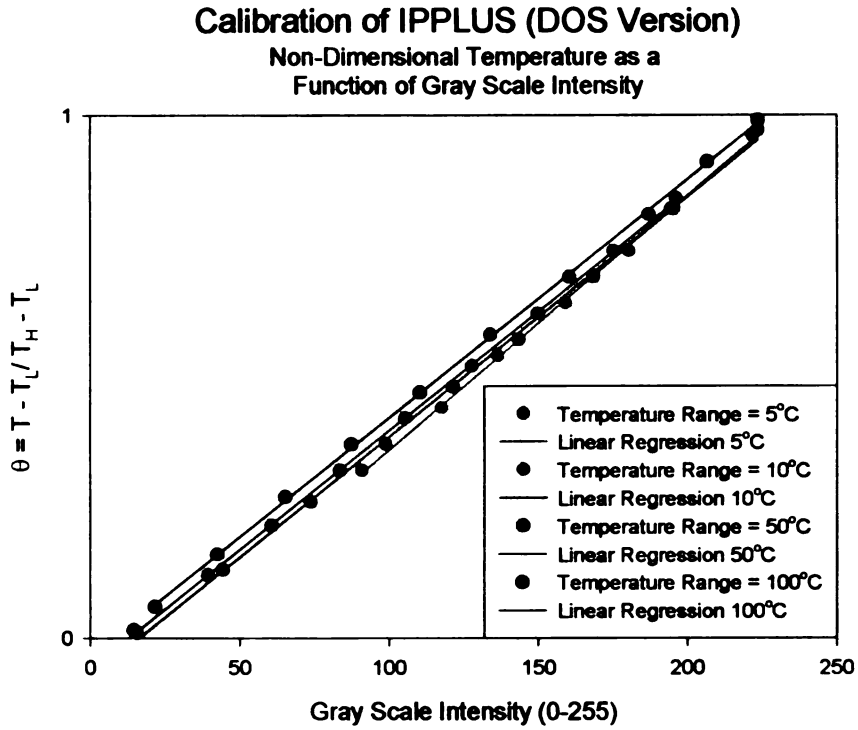

Figure B3. *Non-dimensional temperature as function of gray scale intensity.*

DISCUSSION OF RESULTS

Calibrations such as those in Figure B3 illustrate that the gray scale output of the radiometer is linearly related to temperature. It is interesting that the calibration curve does not cross through the origin and causes an offset in the relationship between gray scale and temperature. This offset is a characteristic of the radiometer's output.

Normally, a black image will have a gray scale intensity of 0, while a white image will have a gray scale value of 255. Although the output of the radiometer varies between "black or cold" and "white or hot", these images do not produce typical gray scale values. For example, pixels which are below the temperature range of the

radiometer appear "black". Normally, the gray intensity of these pixels would be zero. However, the "black" pixels produced by the radiometer are digitized to values higher than zero. Therefore, since the "black" values produced by the radiometer are not truly black an offset exist.

APPENDIX C

SPATIAL CALIBRATION OF IPPLUS FOR
INFRARED TEMPERATURE MEASUREMENT

Often it will be important to illustrate the temperature variations along a surface as a function of position. This appendix presents an example of how a spatial calibration using IPPLUS can be used to provide this information.

In this test, a small piece of braided composite material was heated along one edge with a Nd:YAG laser as shown in Figure C1. As the sample was being engerized, temperature measurements were made with the infrared camera. Due to the small sample

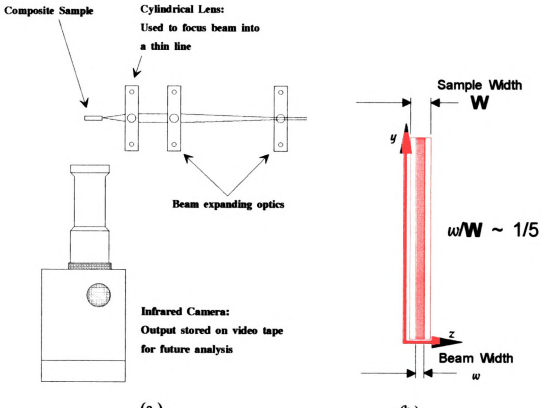

Figure C1. *(a) The test setup used to heat a small braided composite sample. (b.) A schematic representation of the heated region.*

size the 3X telescopic and the 6" close-up lenses were used to increase the spatial resolution. A typical thermal image developed under these heating conditions is shown in Figure C2.

Figure C2. *The output of the Inframetrics Radiometer illustrating the surface variations across the test sample.*

Specific areas of interest within this thermal image can be analyzed using IPPLUS. For example, a bitmap analysis can be conducted on the area within the red rectangle in Figure C2. This produces a two dimensional array of gray scale values as a function of X and Y pixel orientation.

The above information becomes more valuable if temperature variations can be represented as a function of geometric position. This can be accomplished be positioning an object of known length in the radiometer's field of view. In this case, an aluminum ruler was used to provide a reference length. As shown in Figure C3, the emissivity variations between the ruler's aluminum surface and the black scale indications cause apparent temperature differences.

These apparent temperature differences are used to spatially calibrate the system. For example, the line profile function of IPPLUS (represented by the red line in Figure C3) can be used to determine how many pixels correspond to a certain length. This information yields the pixel width in horizontal direction and similar steps can be repeated to find the pixel width in the vertical direction.

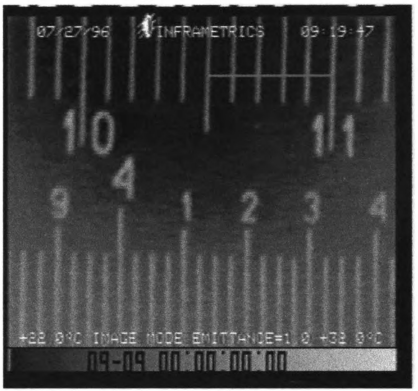

Figure C3. *A ruler imaged with the Inframetrics radiometer used for a horizontal calibration. In this case, the line profile function (represented by the red line) is used to determine to the number of pixels in a given length.*

A LabVIEW program, shown in Figure C4, has been created to use this information and spatially calibrate the output of the radiometer. This program allows the user to enter parameters pertaining to a temperature to gray scale calibration and the information necessary for the determination of the horizontal and vertical pixel widths. This program also transforms the data from the two-dimensional gray scale array, generated with IPPLUS, into a X-Y-Z listing as shown in Figure C5. Data in this format is easily analyzed and plotted using software packages such as SigmaPLOT, TableCurve3D, and Tecplot.

As an example of this utility, a bitmap analysis was performed on the rectangular region in Figure C2. The data was calibrated with the LabVIEW program and plotted using Tecplot. This pseudo-colored plot is illustrated in Figure C6.

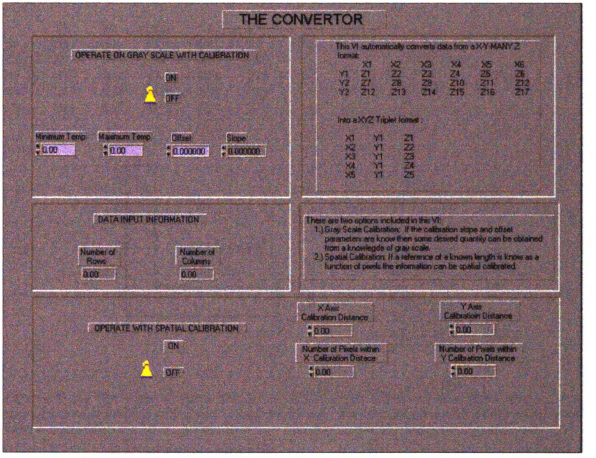

Figure C5. *The front panel of the LabVIEW program used to spatially and thermally calibrate the gray scale information form IPPLUS. This program also transforms the data into a format that can be easily plotted using commercially available software.*

	Y1	Y2	Y3	Y4	Y5
X1	G1	G2	G3	G4	G5
X2	G6	G7	G8	G9	G10
X3	G11	G12	G13	G14	G15
X4	G16	G17	G18	G19	G20
X5	G21	G22	G23	G24	G25

(a.)

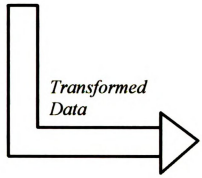

X1	Y1	G1
X1	Y2	G2
X1	Y3	G3
X1	Y4	G4
X1	Y5	G5
X2	Y1	G6
X2	Y2	G7
X2	Y3	G8
X2	Y4	G9
X2	Y5	G10

(b.)

Figure C5. (a.) *The output of bitmap analysis of IPPLUS, formatted as a 2 dimensional array of gray scale intensity as a function of X and Y pixel orientation.* ***(b.)*** *An XYZ format which is easily plotted using commercially developed software. In this case the data is spatially and thermally calibrated.*

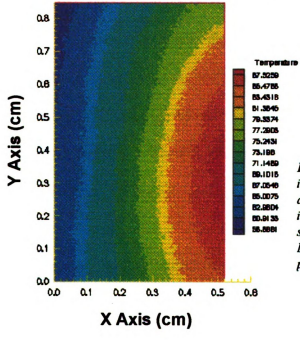

Figure C6. *A Pseudo-colored plot illustrating the temperature variations across a selected region in the thermal image in Figure C2. This data was spatially and thermally calibrated using the LabVIEW program in Figure C4 and plotted using Tecplot..*

APPENDIX D - BEAM DIAGNOSTICS

Laser beam diagnostics includes measurement of energy/power, intensity/beam profile, temporal/time dependence and measurements of beam diameter. These measurements provide a thorough understanding of the characteristics of the laser beam and become important when attempting to optimize the laser for a particular application. In this appendix, two of the initial steps towards developing beam profile measurement techniques are discussed.

CCD CAMERA:

Charged - coupled - device (CCD) cameras have many useful characteristics for doing laser-beam diagnostics. The cameras, when coupled with image processing software, have two primary features. First they provide a picture of the beam profile so the user can effectively see what the beam looks like. The ability to see the profile when adjusting the laser or aligning the optical train provides improvement in laser performance and experimental accuracy. Second, the quantitative and visual feedback complement each other by allowing for precise laser operation and provide a permanent record of the setup and results.

In this study a Javelin JE2062IR CCD camera was used in conjunction with Image Pro Plus (IPPLUS) image processing software to provide information about the spatial distribution of energy throughout the diameter of the laser beam. This CCD camera has a high response at the wavelength of the laser (1064 nm) and is ideally suited for low light

applications. In a typical setup, as shown in Figure D1, the laser beam is positioned to strike the center of the camera's lens. When the output of the laser is attenuated either by the use of beamsplitters or by a reduction in lamp current, beam analysis is possible.

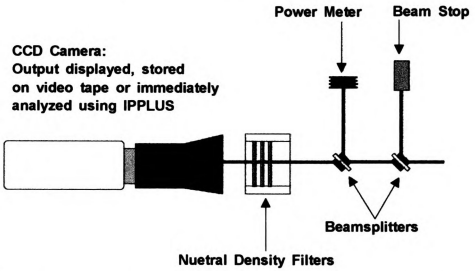

Figure D1. *A typical setup using the CCD camera to obtain a beam profile.*

The output of the CCD camera, shown in Figure D2, is a two dimensional monochrome image with varying gray scale intensity, and can be displayed on a standard black and white monitor. This simple setup provides useful "real time analysis" since the results of course adjustments can be visualized on the monitor with the naked eye.

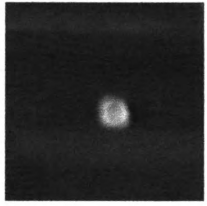

Figure D2. *The output of the laser when visualized with a black and white monitor.*

In order to examine the results of fine adjustments or to obtain a surface fit of the radiation distribution the CCD camera's output must be analyzed using IPPLUS. IPPLUS is a general purpose image processing system which provides the user with an intensity analysis toolbox. Using this type of analysis the user can collect data from the CCD's output based on the intensity values it contains. The bitmap analysis tool is extremely useful in this situation since it provides the intensity values of individual pixels within a user defined area of interest. For example, if the image in Figure D2 was analyzed using a bitmap analysis, information could be represented in a three dimensional plot. As shown in Figure D3, plots such as this give the user information pertaining to the beam's profile.

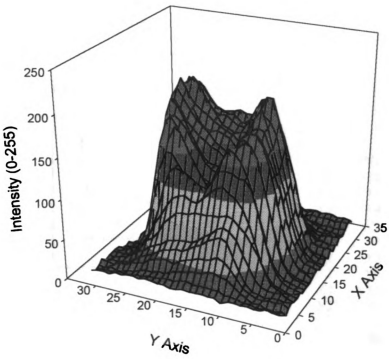

Figure D3. *A three dimensional representation of a laser beam profile. This information was plotted using Jandel Scientific's SigmaPlot.*

The output of the IPPLUS bitmap analysis is in the form of a 2 dimensional array as shown in Figure D4(a.). In order to use the automated surface fitting software, TableCurve3D, this output must be transformed into three columns representing (1.) the pixel numbers along the X axis, (2.) the pixel numbers along the Y axis and (3.) the gray scale intensity of each pixel. The transformed output is illustrated in Figure D4(b.). This transformation can be done fairly quickly using a LabVIEW VI called the "CONVERTOR", shown in Figure D5. In running this program the user is prompted by a

dialog box to enter the file to be converted. Once the conversion is complete, the user is asked to create a new file name.

	Y1	Y2	Y3	Y4	Y5
X1	G1	G2	G3	G4	G5
X2	G6	G7	G8	G9	G10
X3	G11	G12	G13	G14	G15
X4	G16	G17	G18	G19	G20
X5	G21	G22	G23	G24	G25

(a.)

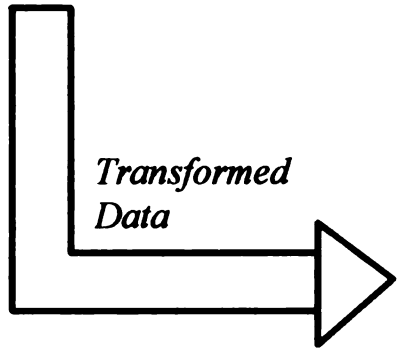

X1	Y1	G1
X1	Y2	G2
X1	Y3	G3
X1	Y4	G4
X1	Y5	G5
X2	Y1	G6
X2	Y2	G7
X2	Y3	G8
X2	Y4	G9
X2	Y5	G10

(b.)

Figure D4. ***(a.)*** *The output of bitmap analysis of IPPLUS, formatted as a 2 dimensional array.* ***(b.)*** *The necessary format for the automated surface fitting program, TableCurve3D.*

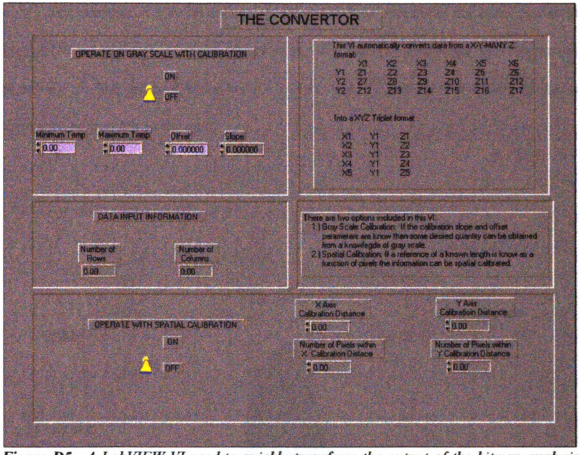

Figure D5. *A LabVIEW VI used to quickly transform the output of the bitmap analysis into the format necessary for the automated surface fitting program, TableCurve3D.*

Once the data has been converted to the proper format it can be imported into TableCurve3D as an ASCII file. This powerful program allows the user to define the type of equations used to fit the data. Then, based on these choices the program automatically generates several equations to fit the data.

The F-statistic is used to measure the extent to which each of the generated equations represent the data. If an additional parameter makes a significant contribution to a model, the F-statistic increases. Otherwise, a decrease occurs. Therefore, the higher the F-statistic, the more effectively a given equation models the data.

For example, if it is of interest to determine how accurately the beam profile in Figure D6 represents a Gaussian distribution, the user can customize the "surface-fit equations" to find the best Gaussian fit. In this case, 12 non-linear gaussian equations were automatically fit to the data.

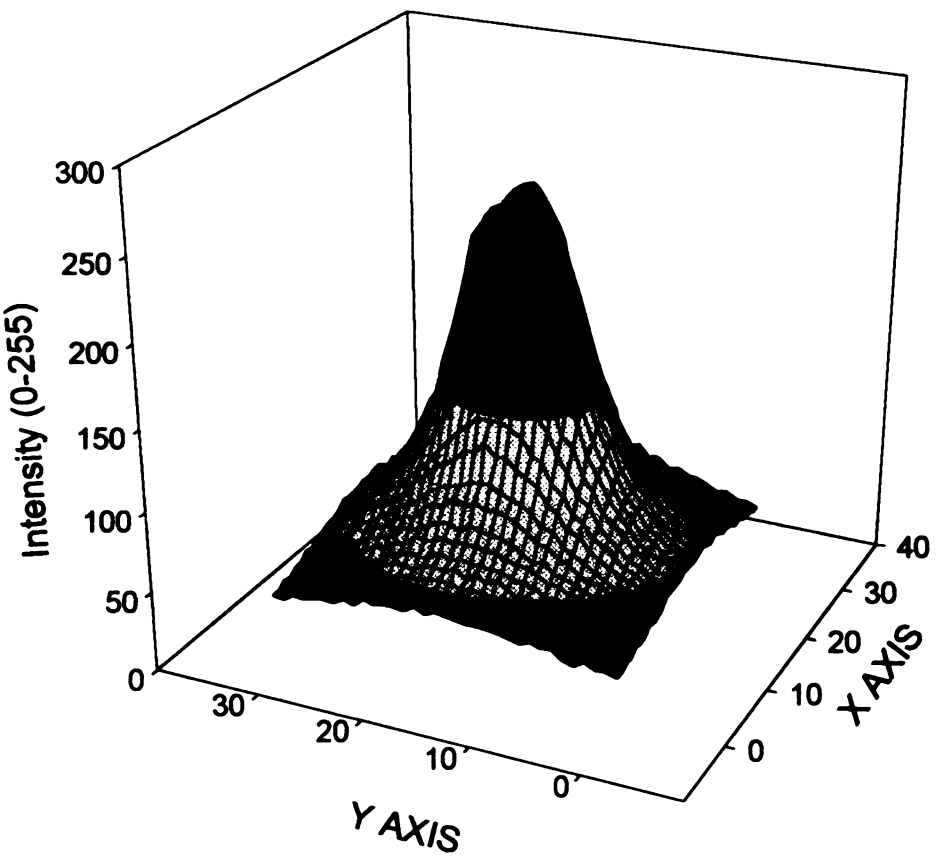

Figure D6. *A three dimensional representation of a laser beam profile. This information was plotted using Jandel Scientific's SigmaPlot.*

Based on the value of the F-statistic the generated equations are ranked. In this case a Gaussian equation of the form

$$z = a + b\exp\left[-0.5\left(\left(\frac{x-c}{d}\right)^2 + \left(\frac{y-e}{f}\right)^2\right)\right]$$

produced the highest F-statistic and best represented the experimental data. Along with yielding the best equation to fit the data, TableCurve3D plots the generated surface and the residuals. These plots are shown in Figure D7 and D8.

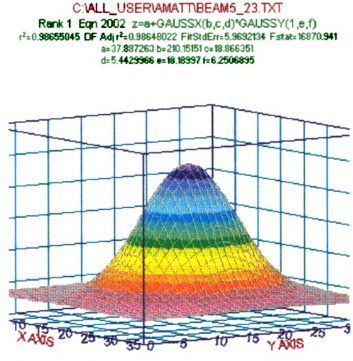

Figure D7*. A plot of the curve generated to fit the experimental data.*

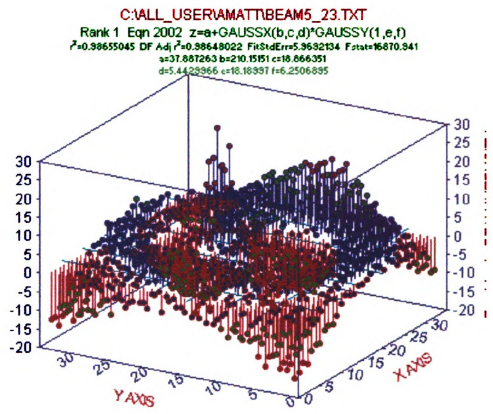

Figure D8. *A plot of the differences between the generated curve and the experimental data.*

Although a great deal of information can be obtained from this type of analysis, saturation problems with the CCD camera limit the application. Whenever the power density of the measured beam exceeds approximately 1.43 W/cm^2 saturation exists. Therefore, even when beamsplitters and neutral density filters are used to attenuate the laser's power and external optics are used to expand the beam, high laser lamp currents cause saturation in the output of the CCD camera as shown in Figure D9.

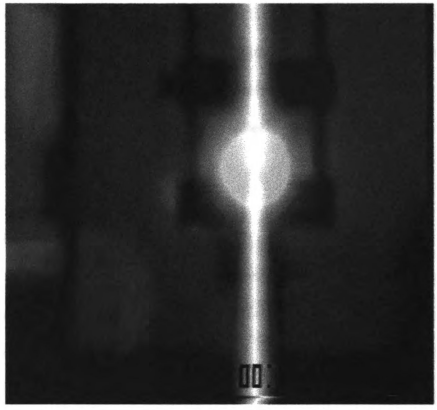

Figure D9. *An example of the saturation problems that occur when attempting to obtain the beam profile.*

Apart from the specific saturation problems with the currently used CCD camera, Roundy and Slobodzian state in their October 1994 Laser Focus World article that CCD cameras generally have some other deficiencies that affect their ability to make accurate laser beam measurements. First, CCD cameras have a low signal-to-noise (S/N) ratio, even when the signal is close to the saturation of the camera. This is important when the signal cannot be adjusted when close to camera saturation, or when information in the low-signal-level wings of the beam is important to the measurement of the laser characteristics.

A second drawback of CCD cameras is the variation in the camera baseline offset or zero signal level. Because all signal levels are measured depending on the baseline

offset, errors in the adjustment can directly affect the measurement of beam profile proprieties. The offset level drifts with time, environmental temperature, and aging. Also this drift is present as the camera heats up as a result of long operating times.

These errors combine to cause problems in obtaining precise laser-beam dimensional measurements.

KNIFE - EDGE METHOD:

One way to obtain accurate dimensional measurements of the laser and eliminate some of the problems associated with CCD cameras is to scan a knife edge across the width of the beam. As shown in Figure D9, a razor blade is traversed across the beam

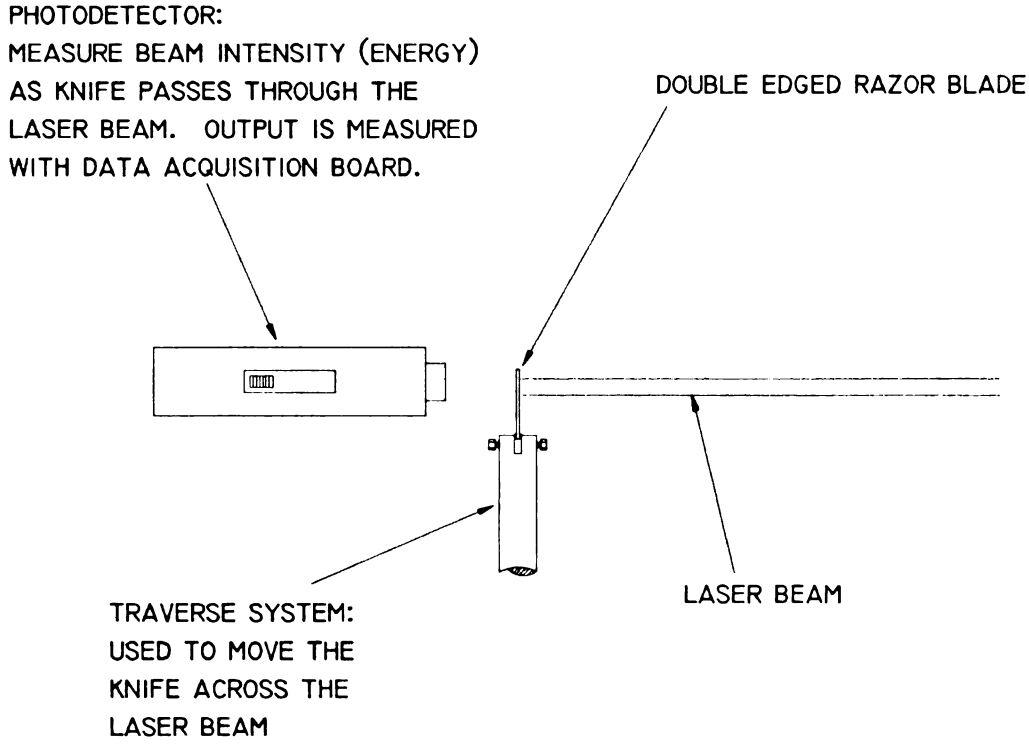

Figure D9. *Experimental setup for knife edge method. In this method a razor blade is passed through the beam. As the razor blade traverses across the beam profile, the unblocked portion of the beam is measured with a photodetector or energy meter. From this output the diameter of the beam is determined.*

profile using a micro-positioner. The beam diameter is considered to be the distance between the points where the knife-edge blocks 10% and 90% of the total beam energy. As illustrated in Figure D10, the choice of this "clip level" is based on the assumption that the measured beam has a Gaussian profile [Siegman, Sasnett, and Johnston 1991].

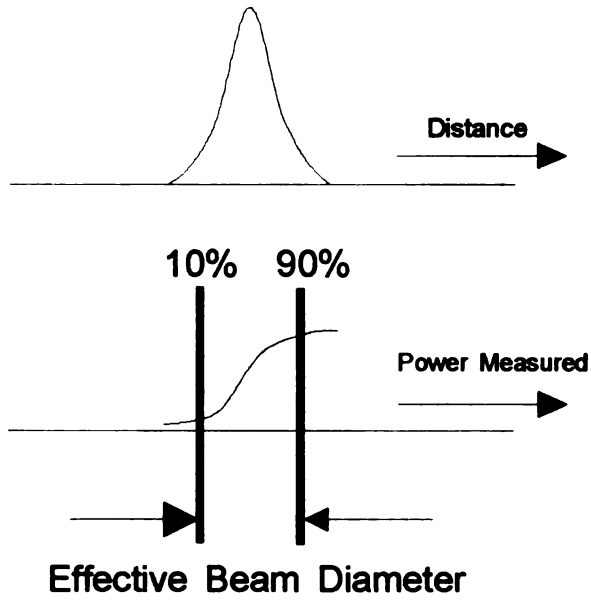

Figure D10. *A knife edge scanned across the beam profile produces an S-shaped curve as the detected power goes from 0%-100%. According to an ISO standard, the beam width is distance between the points where the detector output is between 10% and 90% of the maximum. [Siegman, Sasnett, and Johnston 1991]*

In order to automate this experimental procedure a LabVIEW program was developed. This program, pictured in Figure D11, allows the user to chose between measuring devices and to select the traversing step size. At each location, 30 measurements from one of the devices are averaged and the result is plotted as a function of position. When the measurements at each specific location are complete, the user is prompted to traverse the knife edge to the next location. This procedure is repeated until the knife edge is traversed to a point where it no longer blocks the beam. Based on the acquired information, a regression algorithm calculates the beam diameter and the user

has the option to save the data to a file. Depending on the traverse step size and the beam diameter this test typically takes less than 5 minutes to complete.

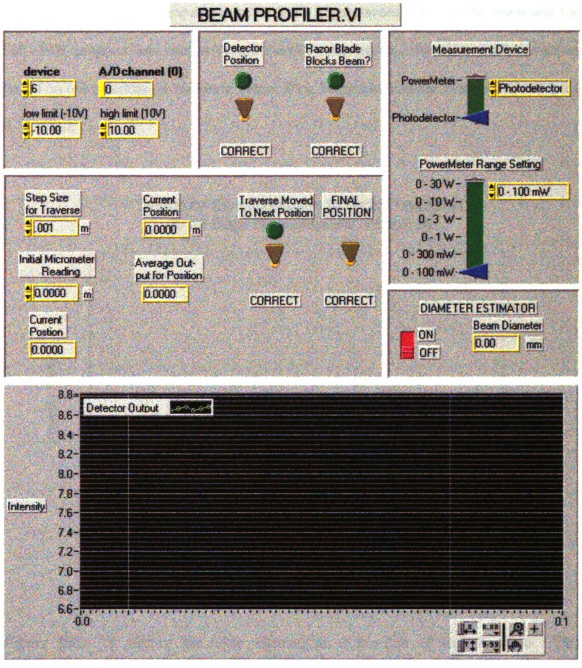

Figure D11. *The front panel of the knife edge traverse LabVIEW VI. This program is used to record the laser intensity as a function of knife edge scan position.*

The knife edge technique has been used to determine the diameter of the laser and to quantify the spatial distribution of radiation generated by a optical train. Based on manufacture specifications, the diameter of the laser is known to be approximately 0.7 mm.. In the first set of experiments, the knife edge traversed across the beam and the LabVIEW program was used to record the laser intensity as a function of scan position. Based on this information, shown in Figure D12, the beam diameter was determined to be 0.7128 mm.

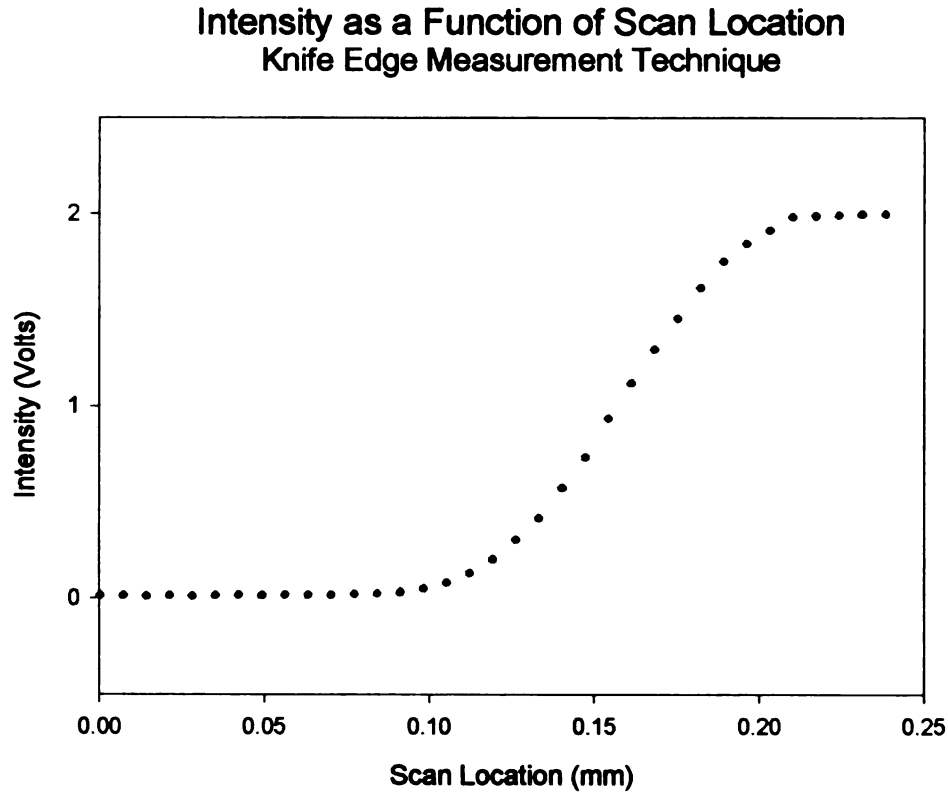

Figure D12. *A plot of the beam intensity as a function of scan location. This information is used to determine the effective beam diameter. In this case, the beam diameter was determined to be 0.7128 mm.*

In a second set of experiments the laser beam was passed through a beam expander and a plano-concave cylindrical lens. The output of this optical system is a line at the focal length of the cylindrical lens. If this optical system is ever to be used to provide a uniform heat flux along a surface, the distribution of radiation along the line must be quantified. This quantification was completed using an experimental setup similar to that in Figure D13. In this setup the beam is passed through a 6.35 mm slot prior to being blocked by the knife edge. If the distribution of radiation is truly uniform along this line, the output of the detector beyond the knife edge would increase linearly as it was exposed to larger amounts of laser radiation. As shown in Figure D14, the output of the detector did linearly increase as a function knife position.

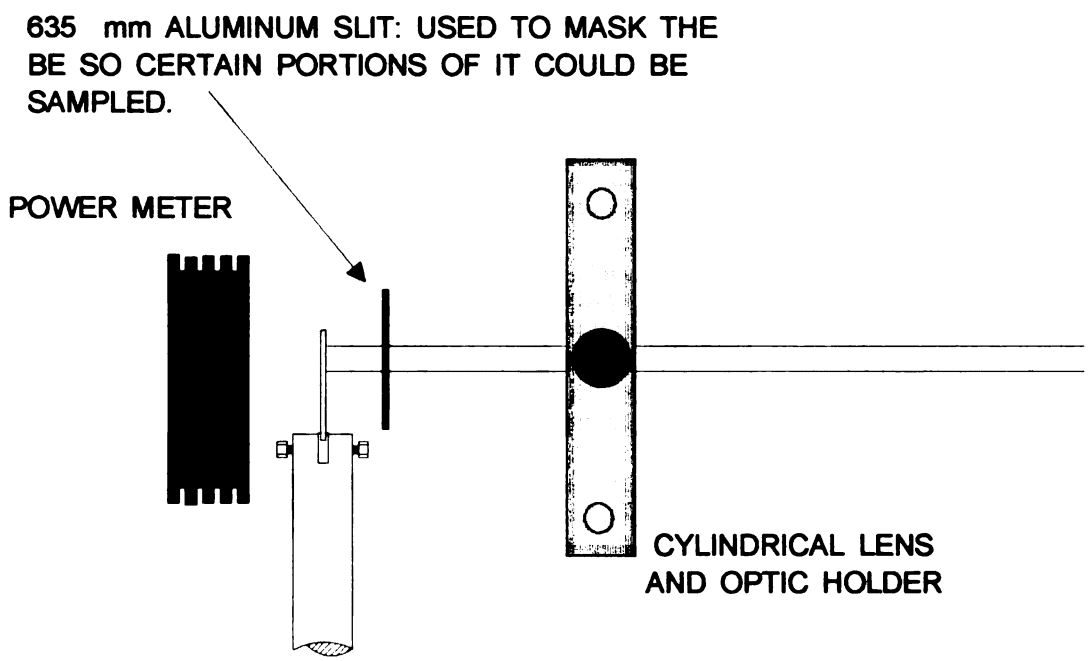

Figure D13. *A schematic representation of the experimental setup used to measure the distribution of radiation generated by an cylindrical lens.*

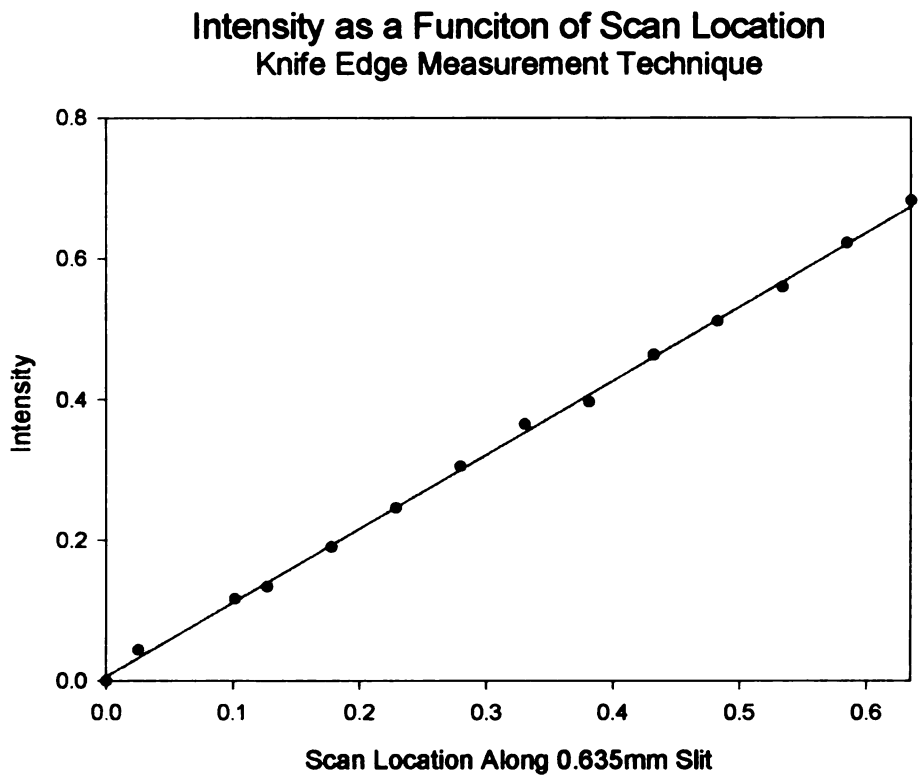

Figure D14. *Laser intensity as a function of scan location. In this case the laser was passed through a 0.635mm slit and the detector output was recorded as the knife edge was traversed across the slit. The linear increase with scan location is a good indication that the distribution of energy across the line of laser radiation is uniform.*

APPENDIX E

Infrared Thermography used to Measure the Temperature Distribution of Boron Doped Diamond Films Heated with Joule Heating

Due to the extended operational environments of modern sensors, it becomes necessary to investigate new materials for optimal sensing performance, especially under harsh environments. In most heating applications, temperature control is essential. Heat generation and temperature sensing are also required for liquid level sensing, mass flow meters, vacuum and pressure gauges, which are based on measurements of heat dissipation. Since the materials commonly used as heating elements lack high sensitivity to temperature change, different materials are utilized for heating and temperature sensing. In such a configuration, the thermal and chemical properties of the materials involved, if not carefully considered, may cause problems. It is also important to minimize the response time and uncertainties in the measurements associated with heat dissipation and the placement of sensing and heating elements.

Use of a single element as both a heater and temperature sensor may help to eliminate such problems. The desired material properties for such an element include high thermal conductivity, ability to be used as an electrical conductor and insulator, high sensitivity to temperature, micro-machining capability, resistance to chemical attack and mechanical stability. The unique intrinsic properties of diamond make it an excellent material for this sensor/heater application . Recent progress in the technology of chemical vapor deposited (CVD) diamond has lead to inexpensive device quality p-type

polycrystalline films . Since the motivation is present it seems logical to determine the heating characteristic of CVD diamond film. In this appendix, two diamond samples are heated with an AC voltage of 100 V and temperature measurements are made using infrared thermography.

EXPERIMENTAL SETUP

The experimental setup comprised of five primary components: 1.) Inframetrics Model 600L Infrared Imaging Radiometer, 2.) thermal image processing system, 3.) FOR.A VTG33 Video Timer, 4.) a video cassette recorder, and 5.) a variac power supply The first two components, the infrared radiometer and the image processing system, comprised the temperature measurement system. The video timer was used to superimpose digital indications of time and date onto the transient output from radiometer. This output was collected in standard RS-170 on a video cassette recorder. The power supply was used to energize each of the samples with an AC voltage of 100 V. A diagram of experimental setup is displayed in Figure E1.

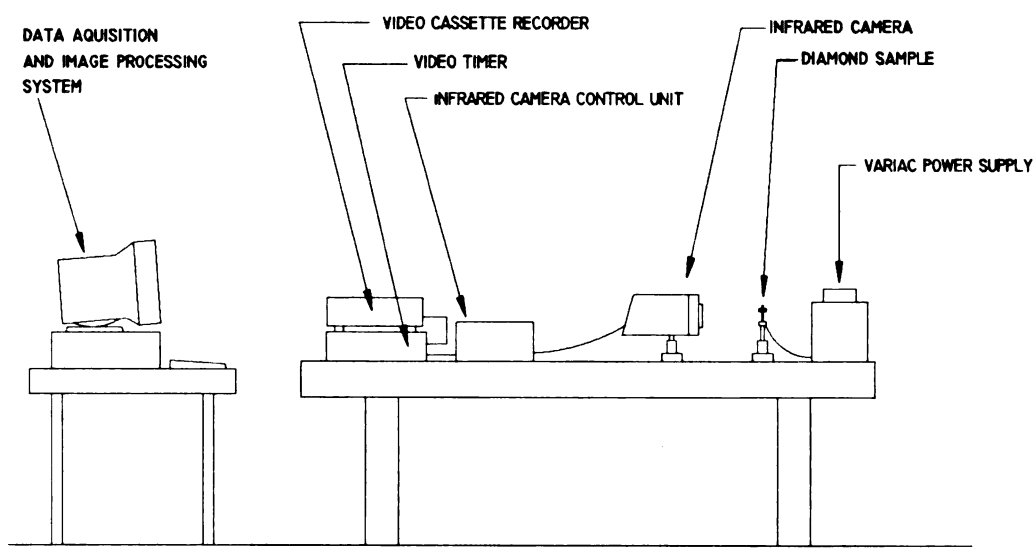

Figure E1. *Diagram of the data acquisition system*

Experimental Procedure

While applying an AC voltage of 100V to each of the samples, the dynamic temperature profiles of diamond/sensor substrates were measured with the infrared camera. The samples were suspended vertically using two lateral copper clamps which also served as electrical contacts. With this arrangement, heat was dissipated by conduction through the clamps and by natural convection. The emissivity of the samples were determined by comparing the measured radiosity from two heated bodies transmitted through and reflected by the surface. Using this method, the emissivities of the samples were determined to be. 0.64 and 0.72.

Under these conditions the temperature distributions across each of the samples were captured at various heating times. These results are shown in Figures E2 through E12

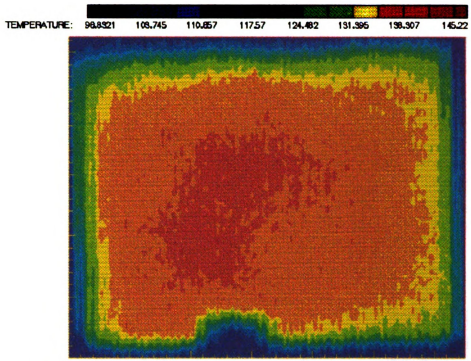

Figure E2. Temperature distribution (°C) of sample # 1 after 10 seconds of heating.

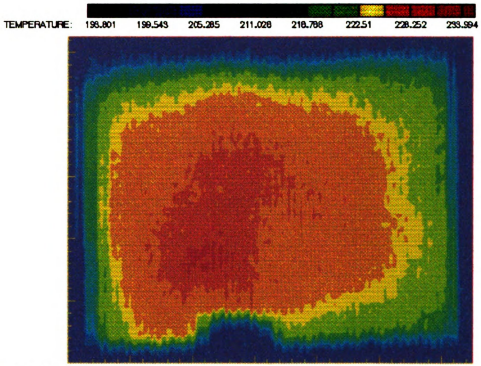

Figure E3. Temperature distribution (°C) of sample # 1 after 20 seconds of heating.

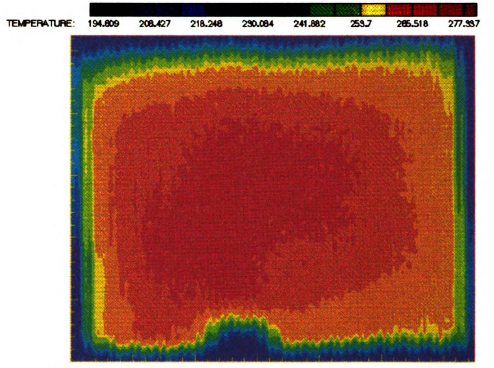

Figure E4. Temperature distribution (°C) of sample # 1 after 35 seconds of heating.

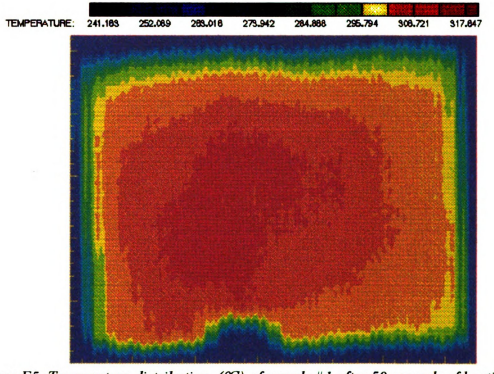

Figure E5. Temperature distribution (°C) of sample # 1 after 50 seconds of heating.

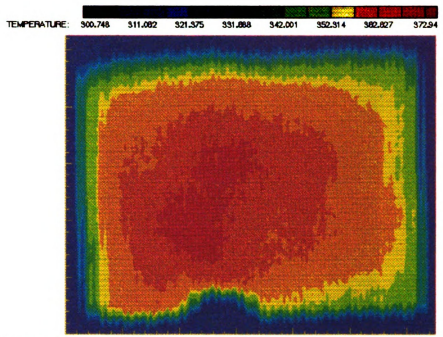

Figure E6. Temperature distribution (℃) of sample #1 after 65 seconds of heating.

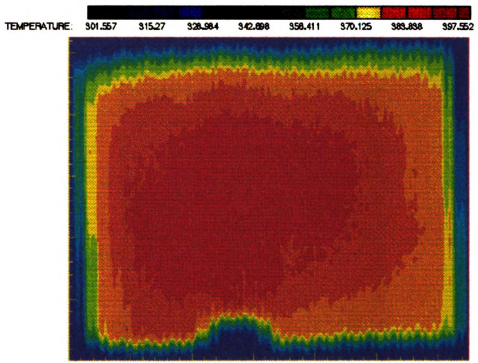

Figure E7. Temperature distribution (℃) of sample #1 after 80 seconds of heating.

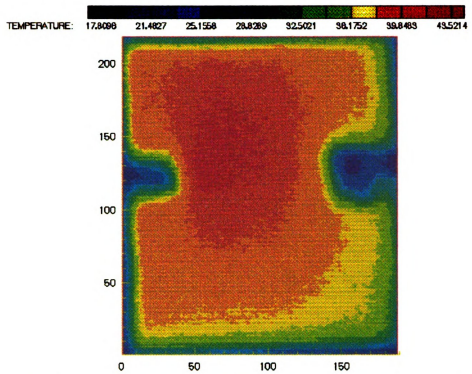

Figure E8. Temperature distribution (℃) of sample #2 after 5 seconds of heating.

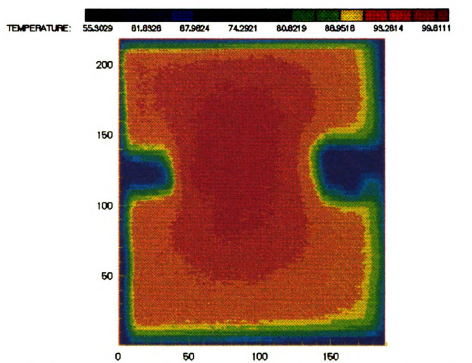

Figure E9. Temperature distribution (℃) of sample #2 after 15 seconds of heating.

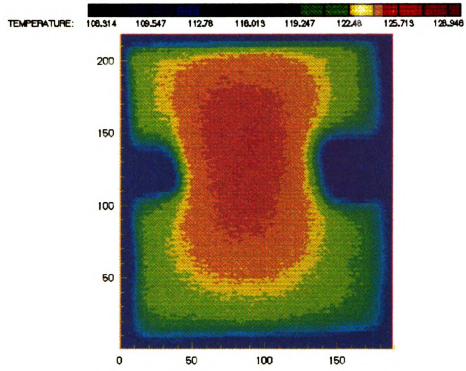

Figure E10. Temperature distribution (℃) of sample #2 after 35 seconds of heating.

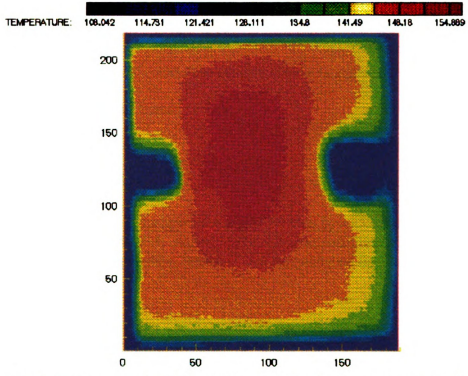

Figure E11. Temperature distribution (℃) of sample #2 after 50 seconds of heating.

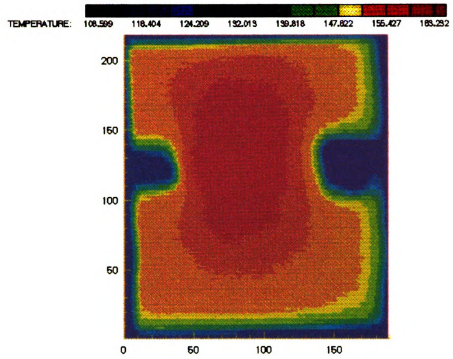

Figure E12. Temperature distribution (℃) of sample #2 after 65 seconds of heating.

These results illustrate that the high thermal conductivity of the diamond substrates produce relatively isothermal surfaces even at high temperatures. As an application, these results verify that a diamond sensor/heater structure is capable of delivering high power densities along a uniformally heated surface.

This appendix represents a portion of a paper written by G.S. Yang, D.M. Aslam, M. White, and J.J. McGrath. This paper, "The Characterization of a Single Structure Diamond Heater and Temperature Sensor, " will be published in September 1996

APPENDIX F

This appendix describes the specific operating conditions for the LabVIEW program developed to monitor the output of the photodetector and externally trigger the video timer. The front panel of this program is shown in Figure F1.

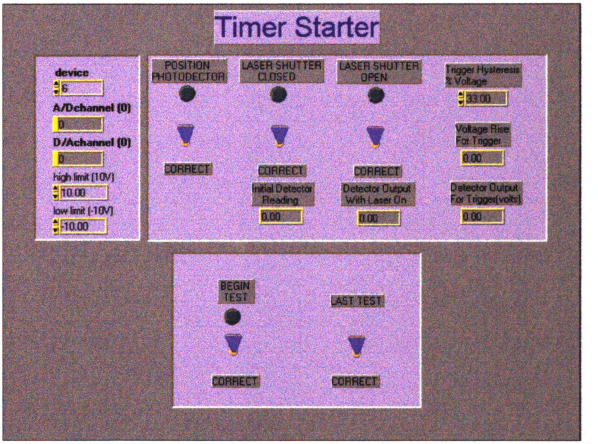

Step 1. Accept the program default settings.
If the default settings are accepted by the user, the program is set to establish communication with the data acquisition board in slot (device) 6. The photodetector response is monitored with A/D channel 0, and the digital to analog signal is generated using D/A channel 0.

Step 2. Run the program
The program is started by depressing the arrow on the left hand side of the menu bar. A "virtual" LED on the front panel is illuminated under the "POSITION PHOTODETECTOR" label. If the photodetector is properly positioned, the toggle button can swithed to "CORRECT". Once this button is depressed the LED under the "LASER SHUTTER CLOSED" label is lit up. If the laser shutter is closed, the toggle button can switched to "CORRECT." At this point, the response of the photodetector is sampled 60 times and an average value is obtained to represent the response of the detector when the shutter is closed.

When the average value is obtained the LED under the "LASER SHUTTER OPEN" label is illuminated. Once the shutter is opened, the toggle button is pressed and output of the photodetector is once again sampled 60 times. The average of these samples represent the response of the detector when the shutter is opened. These average responses are used to develop the trigger criteria and once established do not have to be repeated from test to test unless the laser's power is significantly reduced. At this point the LED under the "BEGIN TEST" label is illuminated and as soon as the experimental components are prepared for data acquisition the toggle button can be switched to correct. Once the button is depressed, the photodector response is sampled at 200 kHz until the laser shutter is opened. When the shutter opens the trigger conditions are meet and a TTL low signal is sent to the video timer. Once the signal is sent, the program loops back and prepares itself for the next test.

APPENDIX G - NLIN INPUT FILE

417	3	2	25	0	0
2.005	0.0004	25			
1	26.82517772		1	1	0.00248724
2	26.79217294		1	1	0.002637982
3	26.72616325		1	1	0.002788724
4	26.67665608		1	1	0.002939466
5	26.57764161		1	1	0.003090208
6	26.54463671		1	1	0.00324095
7	26.49512929		1	1	0.003391691
8	26.46212438		1	1	0.003542433
9	26.41261721		1	1	0.003693175
10	26.36310979		1	1	0.003843917
11	26.36310979		1	1	0.003994659
12	26.3466074		1	1	0.004145401
13	26.2971001		1	1	0.004296142
14	26.24759268		1	1	0.004446884
15	26.2145879		1	1	0.004597626
16	26.18158312		1	1	0.004748368
17	26.14857847		1	1	0.00489911
18	26.1650806		1	1	0.005049852
19	26.13207595		1	1	0.005200593
20	26.13207582		1	1	0.005351335
21	26.1320757		1	1	0.005502077
22	26.11557343		1	1	0.005652819
23	26.04956387		1	1	0.005803561
24	26.00005633		1	1	0.005954303
25	26.01655884		1	1	0.006105045
26	26.00005633		1	1	0.006255786
27	25.95054916		1	1	0.006406528
28	25.91754438		1	1	0.00655727
29	25.86803708		1	1	0.006708012
30	25.86803695		1	1	0.006858754
31	25.86803708		1	1	0.007009496
32	25.90104199		1	1	0.007160237
33	25.90104199		1	1	0.007310979
34	25.86803695		1	1	0.007461721
35	25.83503217		1	1	0.007612463
36	25.81852978		1	1	0.007763205
37	25.80202739		1	1	0.007913947
38	25.83503217		1	1	0.008064688
39	25.85153456		1	1	0.00821543
40	25.81852978		1	1	0.008366172
41	25.73601771		1	1	0.008516914
42	25.67000777		1	1	0.008667656
43	25.71951507		1	1	0.008818398
44	25.75251997		1	1	0.008969139
45	25.7525201		1	1	0.009119881
46	25.80202727		1	1	0.009270623
47	25.80202727		1	1	0.009421365
48	25.7525201		1	1	0.009572107
49	25.7030128		1	1	0.009722849
50	25.70301268		1	1	0.009873591
51	25.68651029		1	1	0.010024332

52	25.70301268	1	1	0.010175074
53	25.67000777	1	1	0.010325816
54	25.6205006	1	1	0.010476558
55	25.5379884	1	1	0.0106273
56	25.55449091	1	1	0.010778042
57	25.63700286	1	1	0.010928783
58	25.6205006	1	1	0.011079525
59	25.57099318	1	1	0.011230267
60	25.5379884	1	1	0.011381009
61	25.58749569	1	1	0.011531751
62	25.62050047	1	1	0.011682493
63	25.52148613	1	1	0.011833234
64	25.4389738	1	1	0.011983976
65	25.4389738	1	1	0.012134718
66	25.45547619	1	1	0.01228546
67	25.45547632	1	1	0.012436202
68	25.4389738	1	1	0.012586944
69	25.43897393	1	1	0.012737685
70	25.43897393	1	1	0.012888427
71	25.50498349	1	1	0.013039169
72	25.47197871	1	1	0.013189911
73	25.38946651	1	1	0.013340653
74	25.38946663	1	1	0.013491395
75	25.38946663	1	1	0.013642136
76	25.42247141	1	1	0.013792878
77	25.38946651	1	1	0.01394362
78	25.38946651	1	1	0.014094362
79	25.4059689	1	1	0.014245104
80	25.3564616	1	1	0.014395846
81	25.33995921	1	1	0.014546588
82	25.35646173	1	1	0.014697329
83	25.38946651	1	1	0.014848071
84	25.38946651	1	1	0.014998813
85	25.32345682	1	1	0.015149555
86	25.33995921	1	1	0.015300297
87	25.42247129	1	1	0.015451039
88	25.4059689	1	1	0.01560178
89	25.35646173	1	1	0.015752522
90	25.29045192	1	1	0.015903264
91	25.2244421	1	1	0.016054006
92	25.22444223	1	1	0.016204748
93	25.29045179	1	1	0.01635549
94	25.30695431	1	1	0.016506231
95	25.29045192	1	1	0.016656973
96	25.27394953	1	1	0.016807715
97	25.24094449	1	1	0.016958457
98	25.20793971	1	1	0.017109199
99	25.25744714	1	1	0.017259941
100	25.3564616	1	1	0.017410682
101	25.37296412	1	1	0.017561424
102	25.30695431	1	1	0.017712166
103	25.29045192	1	1	0.017862908
104	25.29045192	1	1	0.01801365
105	25.37296399	1	1	0.018164392
106	25.42247141	1	1	0.018315134
107	25.37296412	1	1	0.018465875
108	25.3564616	1	1	0.018616617
109	25.3564616	1	1	0.018767359
110	25.4059689	1	1	0.018918101
111	25.45547619	1	1	0.019068843

112	25.3564616	1	1	0.019219585
113	25.29045192	1	1	0.019370326
114	25.3564616	1	1	0.019521068
115	25.4389738	1	1	0.01967181
116	25.38946651	1	1	0.019822552
117	25.38946651	1	1	0.019973294
118	25.4059689	1	1	0.020124036
119	25.42247141	1	1	0.020274777
120	25.37296412	1	1	0.020425519
121	25.32345682	1	1	0.020576261
122	25.30695443	1	1	0.020727003
123	25.33995921	1	1	0.020877745
124	25.3564616	1	1	0.021028487
125	25.29045192	1	1	0.021179228
126	25.27394953	1	1	0.02132997
127	25.33995909	1	1	0.021480712
128	25.37296399	1	1	0.021631454
129	25.32345682	1	1	0.021782196
130	25.32345682	1	1	0.021932938
131	25.3234567	1	1	0.02208368
132	25.29045192	1	1	0.022234421
133	25.2739494	1	1	0.022385163
134	25.24094462	1	1	0.022535905
135	25.19143732	1	1	0.022686647
136	25.19143732	1	1	0.022837389
137	25.19143732	1	1	0.022988131
138	25.17493493	1	1	0.023138872
139	25.15843242	1	1	0.023289614
140	28.22788465	1	2	0.00248724
141	28.16187509	1	2	0.002637982
142	28.04635836	1	2	0.002788724
143	27.93084163	1	2	0.002939466
144	27.83182729	1	2	0.003090208
145	27.76581773	1	2	0.00324095
146	27.76581773	1	2	0.003391691
147	27.76581773	1	2	0.003542433
148	27.69980817	1	2	0.003693175
149	27.63379861	1	2	0.003843917
150	27.58429018	1	2	0.003994659
151	27.55128414	1	2	0.004145401
152	27.5512854	1	2	0.004296142
153	27.5512854	1	2	0.004446884
154	27.51827936	1	2	0.004597626
155	27.45226854	1	2	0.004748368
156	27.38625898	1	2	0.00489911
157	27.3532542	1	2	0.005049852
158	27.32024942	1	2	0.005200593
159	27.27074225	1	2	0.005351335
160	27.25423986	1	2	0.005502077
161	27.20473269	1	2	0.005652819
162	27.12222074	1	2	0.005803561
163	27.05621118	1	2	0.005954303
164	27.0232064	1	2	0.006105045
165	27.05621118	1	2	0.006255786
166	27.03970879	1	2	0.006406528
167	27.0232064	1	2	0.00655727
168	27.00670401	1	2	0.006708012
169	27.00670401	1	2	0.006858754
170	27.00670401	1	2	0.007009496
171	26.99020162	1	2	0.007160237

172	26.94069445	1	2	0.007310979
173	26.94069445	1	2	0.007461721
174	26.94069445	1	2	0.007612463
175	26.99020162	1	2	0.007763205
176	26.95719684	1	2	0.007913947
177	26.94069445	1	2	0.008064688
178	26.87468489	1	2	0.00821543
179	26.79217294	1	2	0.008366172
180	26.79217294	1	2	0.008516914
181	26.84168011	1	2	0.008667656
182	26.84168011	1	2	0.008818398
183	26.87468489	1	2	0.008969139
184	26.87468489	1	2	0.009119881
185	26.89118728	1	2	0.009270623
186	26.84168011	1	2	0.009421365
187	26.79217294	1	2	0.009572107
188	26.77567055	1	2	0.009722849
189	26.77567055	1	2	0.009873591
190	26.75916816	1	2	0.010024332
191	26.72616338	1	2	0.010175074
192	26.67665608	1	2	0.010325816
193	26.6931586	1	2	0.010476558
194	26.70966086	1	2	0.0106273
195	26.75916803	1	2	0.010778042
196	26.72616338	1	2	0.010928783
197	26.67665596	1	2	0.011079525
198	26.66015369	1	2	0.011230267
199	26.66015357	1	2	0.011381009
200	26.66015369	1	2	0.011531751
201	26.57764149	1	2	0.011682493
202	26.59414413	1	2	0.011833234
203	26.57764161	1	2	0.011983976
204	26.61064639	1	2	0.012134718
205	26.61064627	1	2	0.01228546
206	26.6436513	1	2	0.012436202
207	26.594144	1	2	0.012586944
208	26.52813432	1	2	0.012737685
209	26.59414413	1	2	0.012888427
210	26.62714879	1	2	0.013039169
211	26.62714879	1	2	0.013189911
212	26.62714891	1	2	0.013340653
213	26.66015369	1	2	0.013491395
214	26.59414413	1	2	0.013642136
215	26.49512941	1	2	0.013792878
216	26.49512941	1	2	0.01394362
217	26.54463671	1	2	0.014094362
218	26.5611391	1	2	0.014245104
219	26.5116318	1	2	0.014395846
220	26.54463658	1	2	0.014546588
221	26.5611391	1	2	0.014697329
222	26.57764161	1	2	0.014848071
223	26.56113922	1	2	0.014998813
224	26.56113922	1	2	0.015149555
225	26.56113922	1	2	0.015300297
226	26.59414413	1	2	0.015451039
227	26.5611391	1	2	0.01560178
228	26.52813419	1	2	0.015752522
229	26.49512929	1	2	0.015903264
230	26.52813419	1	2	0.016054006
231	26.57764161	1	2	0.016204748

232	26.52813432	1	2	0.01635549
233	26.49512929	1	2	0.016506231
234	26.44562212	1	2	0.016656973
235	26.44562212	1	2	0.016807715
236	26.49512929	1	2	0.016958457
237	26.47862702	1	2	0.017109199
238	26.42911973	1	2	0.017259941
239	26.39611482	1	2	0.017410682
240	26.4786269	1	2	0.017561424
241	26.56113922	1	2	0.017712166
242	26.57764161	1	2	0.017862908
243	26.56113922	1	2	0.01801365
244	26.5116318	1	2	0.018164392
245	26.49512929	1	2	0.018315134
246	26.4786269	1	2	0.018465875
247	26.4786269	1	2	0.018616617
248	26.49512941	1	2	0.018767359
249	26.49512941	1	2	0.018918101
250	26.54463658	1	2	0.019068843
251	26.49512941	1	2	0.019219585
252	26.39611457	1	2	0.019370326
253	26.3796123	1	2	0.019521068
254	26.3796123	1	2	0.01967181
255	26.33010488	1	2	0.019822552
256	26.28059759	1	2	0.019973294
257	26.31360249	1	2	0.020124036
258	26.36310991	1	2	0.020274777
259	26.3466074	1	2	0.020425519
260	26.31360262	1	2	0.020576261
261	26.28059771	1	2	0.020727003
262	26.2640952	1	2	0.020877745
263	26.29709998	1	2	0.021028487
264	26.36310979	1	2	0.021179228
265	26.36310979	1	2	0.02132997
266	26.31360249	1	2	0.021480712
267	26.24759281	1	2	0.021631454
268	26.21458803	1	2	0.021782196
269	26.28059759	1	2	0.021932938
270	26.39611469	1	2	0.02208368
271	26.3796123	1	2	0.022234421
272	26.31360262	1	2	0.022385163
273	26.28059771	1	2	0.022535905
274	26.2971001	1	2	0.022686647
275	26.24759268	1	2	0.022837389
276	26.2145879	1	2	0.022988131
277	26.2640952	1	2	0.023138872
278	26.23109042	1	2	0.023289614
279	29.01296142	1	3	0.00248724
280	28.93044947	1	3	0.002637982
281	28.91394708	1	3	0.002788724
282	28.93044947	1	3	0.002939466
283	28.86443991	1	3	0.003090208
284	28.83143513	1	3	0.00324095
285	28.7159184	1	3	0.003391691
286	28.63340645	1	3	0.003542433
287	28.61690406	1	3	0.003693175
288	28.53439211	1	3	0.003843917
289	28.46838255	1	3	0.003994659
290	28.45188016	1	3	0.004145401
291	28.45188016	1	3	0.004296142

292	28.3858706	1	3	0.004446884
293	28.30335865	1	3	0.004597626
294	28.23734909	1	3	0.004748368
295	28.25385148	1	3	0.00489911
296	28.2208467	1	3	0.005049852
297	28.2208467	1	3	0.005200593
298	28.2208467	1	3	0.005351335
299	28.27035387	1	3	0.005502077
300	28.23734909	1	3	0.005652819
301	28.18784192	1	3	0.005803561
302	28.13833475	1	3	0.005954303
303	28.10532997	1	3	0.006105045
304	28.12183236	1	3	0.006255786
305	28.0558228	1	3	0.006406528
306	28.02281802	1	3	0.00655727
307	28.02281802	1	3	0.006708012
308	27.98981324	1	3	0.006858754
309	28.00631563	1	3	0.007009496
310	27.97331085	1	3	0.007160237
311	27.95680846	1	3	0.007310979
312	27.92380368	1	3	0.007461721
313	27.97331085	1	3	0.007612463
314	27.97331085	1	3	0.007763205
315	27.94030607	1	3	0.007913947
316	27.92380368	1	3	0.008064688
317	27.92380368	1	3	0.00821543
318	27.90730129	1	3	0.008366172
319	27.87429651	1	3	0.008516914
320	27.80828695	1	3	0.008667656
321	27.79178456	1	3	0.008818398
322	27.87429651	1	3	0.008969139
323	27.92380368	1	3	0.009119881
324	27.92380368	1	3	0.009270623
325	27.90730129	1	3	0.009421365
326	27.87429651	1	3	0.009572107
327	27.85779412	1	3	0.009722849
328	27.84129173	1	3	0.009873591
329	27.85779412	1	3	0.010024332
330	27.82478934	1	3	0.010175074
331	27.80828695	1	3	0.010325816
332	27.79178456	1	3	0.010476558
333	27.77528217	1	3	0.0106273
334	27.725775	1	3	0.010778042
335	27.725775	1	3	0.010928783
336	27.74227739	1	3	0.011079525
337	27.70927261	1	3	0.011230267
338	27.69277022	1	3	0.011381009
339	27.65976418	1	3	0.011531751
340	27.67626657	1	3	0.011682493
341	27.64326179	1	3	0.011833234
342	27.62675814	1	3	0.011983976
343	27.67626783	1	3	0.012134718
344	27.64326179	1	3	0.01228546
345	27.59375336	1	3	0.012436202
346	27.56074732	1	3	0.012586944
347	27.57725097	1	3	0.012737685
348	27.57725097	1	3	0.012888427
349	27.54424493	1	3	0.013039169
350	27.56074732	1	3	0.013189911
351	27.56074732	1	3	0.013340653

352	27.57725097	1	3	0.013491395
353	27.56074858	1	3	0.013642136
354	27.54424619	1	3	0.013792878
355	27.56074732	1	3	0.01394362
356	27.52774254	1	3	0.014094362
357	27.51124015	1	3	0.014245104
358	27.52774254	1	3	0.014395846
359	27.56074732	1	3	0.014546588
360	27.57724971	1	3	0.014697329
361	27.61025575	1	3	0.014848071
362	27.62675814	1	3	0.014998813
363	27.54424493	1	3	0.015149555
364	27.47823537	1	3	0.015300297
365	27.47823537	1	3	0.015451039
366	27.51124015	1	3	0.01560178
367	27.54424493	1	3	0.015752522
368	27.56074732	1	3	0.015903264
369	27.59375462	1	3	0.016054006
370	27.61025575	1	3	0.016204748
371	27.54424493	1	3	0.01635549
372	27.47823537	1	3	0.016506231
373	27.49473776	1	3	0.016656973
374	27.52774254	1	3	0.016807715
375	27.49473776	1	3	0.016958457
376	27.41222581	1	3	0.017109199
377	27.4287282	1	3	0.017259941
378	27.39572342	1	3	0.017410682
379	27.37922103	1	3	0.017561424
380	27.39572342	1	3	0.017712166
381	27.44523059	1	3	0.017862908
382	27.46173298	1	3	0.01801365
383	27.4287282	1	3	0.018164392
384	27.39572342	1	3	0.018315134
385	27.44523059	1	3	0.018465875
386	27.46173298	1	3	0.018616617
387	27.44523059	1	3	0.018767359
388	27.4287282	1	3	0.018918101
389	27.44523059	1	3	0.019068843
390	27.46173298	1	3	0.019219585
391	27.4287282	1	3	0.019370326
392	27.37922103	1	3	0.019521068
393	27.4287282	1	3	0.01967181
394	27.49473776	1	3	0.019822552
395	27.44523059	1	3	0.019973294
396	27.34621625	1	3	0.020124036
397	27.37922103	1	3	0.020274777
398	27.4287282	1	3	0.020425519
399	27.41222581	1	3	0.020576261
400	27.37922103	1	3	0.020727003
401	27.41222581	1	3	0.020877745
402	27.44523059	1	3	0.021028487
403	27.41222581	1	3	0.021179228
404	27.37922103	1	3	0.02132997
405	27.4287282	1	3	0.021480712
406	27.4287282	1	3	0.021631454
407	27.37922103	1	3	0.021782196
408	27.39572342	1	3	0.021932938
409	27.46173298	1	3	0.02208368
410	27.46173298	1	3	0.022234421
411	27.41222581	1	3	0.022385163

412	27.39572342	1	3	0.022535905
413	27.39572342	1	3	0.022686647
414	27.37922103	1	3	0.022837389
415	27.34621625	1	3	0.022988131
416	27.31321147	1	3	0.023138872
417	27.31321147	1	3	0.023289614
2				
0.0005	0.0254			

APPENDIX I - NLIN OUTPUT FILE

BEGIN LISTING INPUT QUANTITIES

BLOCK 1
N = NO. DATA POINTS, NP = NO. PARAMETERS
NT = NO. OF INDEPENDENT VARIABLES
ITMAX = MAXIMUM NO. OF ITERATIONS
MODEL = MODEL NUMBER, IF SEVERAL MODELS IN SUBROUTINES: MODEL AND SENS
IPRINT = 1 FOR USUAL PRINTOUTS, 0 FOR LESS

N	NP	NT	ITMAX	MODEL	IPRINT
417	3	2	25	0	0

BLOCK 2
B(1),B(2),..,B(NP) ARE INITIAL PARAMETER ESTIMATES

B(1) = .20050E+01
B(2) = .40000E-03
B(3) = .25000E+02

BLOCK 3
J = DATA POINT INDEX, Y(J) = MEASURED VALUE
SIGMA(J) = STANDARD DEVIATION OF Y(J)
T(J,1) = FIRST INDEPENDENT VARIABLE

J	Y(J)	SIGMA(J)	T(J,1)	T(J,2)
1	26.82518	1.00000	1.00000	.00249
2	26.79217	1.00000	1.00000	.00264
3	26.72616	1.00000	1.00000	.00279
4	26.67666	1.00000	1.00000	.00294
5	26.57764	1.00000	1.00000	.00309
6	26.54464	1.00000	1.00000	.00324
7	26.49513	1.00000	1.00000	.00339
8	26.46212	1.00000	1.00000	.00354
9	26.41262	1.00000	1.00000	.00369
10	26.36311	1.00000	1.00000	.00384
11	26.36311	1.00000	1.00000	.00399
12	26.34661	1.00000	1.00000	.00415
13	26.29710	1.00000	1.00000	.00430
14	26.24759	1.00000	1.00000	.00445
15	26.21459	1.00000	1.00000	.00460
16	26.18158	1.00000	1.00000	.00475
17	26.14858	1.00000	1.00000	.00490
18	26.16508	1.00000	1.00000	.00505
19	26.13208	1.00000	1.00000	.00520
20	26.13208	1.00000	1.00000	.00535
21	26.13208	1.00000	1.00000	.00550
22	26.11557	1.00000	1.00000	.00565
23	26.04956	1.00000	1.00000	.00580
24	26.00006	1.00000	1.00000	.00595
25	26.01656	1.00000	1.00000	.00611
26	26.00006	1.00000	1.00000	.00626
27	25.95055	1.00000	1.00000	.00641
28	25.91754	1.00000	1.00000	.00656
29	25.86804	1.00000	1.00000	.00671
30	25.86804	1.00000	1.00000	.00686
31	25.86804	1.00000	1.00000	.00701
32	25.90104	1.00000	1.00000	.00716
33	25.90104	1.00000	1.00000	.00731
34	25.86804	1.00000	1.00000	.00746
35	25.83503	1.00000	1.00000	.00761
36	25.81853	1.00000	1.00000	.00776

37	25.80203	1.00000	1.00000	.00791
38	25.83503	1.00000	1.00000	.00806
39	25.85153	1.00000	1.00000	.00822
40	25.81853	1.00000	1.00000	.00837
41	25.73602	1.00000	1.00000	.00852
42	25.67001	1.00000	1.00000	.00867
43	25.71952	1.00000	1.00000	.00882
44	25.75252	1.00000	1.00000	.00897
45	25.75252	1.00000	1.00000	.00912
46	25.80203	1.00000	1.00000	.00927
47	25.80203	1.00000	1.00000	.00942
48	25.75252	1.00000	1.00000	.00957
49	25.70301	1.00000	1.00000	.00972
50	25.70301	1.00000	1.00000	.00987
51	25.68651	1.00000	1.00000	.01002
52	25.70301	1.00000	1.00000	.01018
53	25.67001	1.00000	1.00000	.01033
54	25.62050	1.00000	1.00000	.01048
55	25.53799	1.00000	1.00000	.01063
56	25.55449	1.00000	1.00000	.01078
57	25.63700	1.00000	1.00000	.01093
58	25.62050	1.00000	1.00000	.01108
59	25.57099	1.00000	1.00000	.01123
60	25.53799	1.00000	1.00000	.01138
61	25.58750	1.00000	1.00000	.01153
62	25.62050	1.00000	1.00000	.01168
63	25.52149	1.00000	1.00000	.01183
64	25.43897	1.00000	1.00000	.01198
65	25.43897	1.00000	1.00000	.01213
66	25.45548	1.00000	1.00000	.01229
67	25.45548	1.00000	1.00000	.01244
68	25.43897	1.00000	1.00000	.01259
69	25.43897	1.00000	1.00000	.01274
70	25.43897	1.00000	1.00000	.01289
71	25.50498	1.00000	1.00000	.01304
72	25.47198	1.00000	1.00000	.01319
73	25.38947	1.00000	1.00000	.01334
74	25.38947	1.00000	1.00000	.01349
75	25.38947	1.00000	1.00000	.01364
76	25.42247	1.00000	1.00000	.01379
77	25.38947	1.00000	1.00000	.01394
78	25.38947	1.00000	1.00000	.01409
79	25.40597	1.00000	1.00000	.01425
80	25.35646	1.00000	1.00000	.01440
81	25.33996	1.00000	1.00000	.01455
82	25.35646	1.00000	1.00000	.01470
83	25.38947	1.00000	1.00000	.01485
84	25.38947	1.00000	1.00000	.01500
85	25.32346	1.00000	1.00000	.01515
86	25.33996	1.00000	1.00000	.01530
87	25.42247	1.00000	1.00000	.01545
88	25.40597	1.00000	1.00000	.01560
89	25.35646	1.00000	1.00000	.01575
90	25.29045	1.00000	1.00000	.01590
91	25.22444	1.00000	1.00000	.01605
92	25.22444	1.00000	1.00000	.01620
93	25.29045	1.00000	1.00000	.01636
94	25.30695	1.00000	1.00000	.01651
95	25.29045	1.00000	1.00000	.01666
96	25.27395	1.00000	1.00000	.01681
97	25.24094	1.00000	1.00000	.01696
98	25.20794	1.00000	1.00000	.01711
99	25.25745	1.00000	1.00000	.01726
100	25.35646	1.00000	1.00000	.01741
101	25.37296	1.00000	1.00000	.01756
102	25.30695	1.00000	1.00000	.01771
103	25.29045	1.00000	1.00000	.01786
104	25.29045	1.00000	1.00000	.01801
105	25.37296	1.00000	1.00000	.01816
106	25.42247	1.00000	1.00000	.01832
107	25.37296	1.00000	1.00000	.01847

108	25.35646	1.00000	1.00000	.01862
109	25.35646	1.00000	1.00000	.01877
110	25.40597	1.00000	1.00000	.01892
111	25.45548	1.00000	1.00000	.01907
112	25.35646	1.00000	1.00000	.01922
113	25.29045	1.00000	1.00000	.01937
114	25.35646	1.00000	1.00000	.01952
115	25.43897	1.00000	1.00000	.01967
116	25.38947	1.00000	1.00000	.01982
117	25.38947	1.00000	1.00000	.01997
118	25.40597	1.00000	1.00000	.02012
119	25.42247	1.00000	1.00000	.02027
120	25.37296	1.00000	1.00000	.02043
121	25.32346	1.00000	1.00000	.02058
122	25.30695	1.00000	1.00000	.02073
123	25.33996	1.00000	1.00000	.02088
124	25.35646	1.00000	1.00000	.02103
125	25.29045	1.00000	1.00000	.02118
126	25.27395	1.00000	1.00000	.02133
127	25.33996	1.00000	1.00000	.02148
128	25.37296	1.00000	1.00000	.02163
129	25.32346	1.00000	1.00000	.02178
130	25.32346	1.00000	1.00000	.02193
131	25.32346	1.00000	1.00000	.02208
132	25.29045	1.00000	1.00000	.02223
133	25.27395	1.00000	1.00000	.02239
134	25.24094	1.00000	1.00000	.02254
135	25.19144	1.00000	1.00000	.02269
136	25.19144	1.00000	1.00000	.02284
137	25.19144	1.00000	1.00000	.02299
138	25.17493	1.00000	1.00000	.02314
139	25.15843	1.00000	1.00000	.02329
140	28.22788	1.00000	2.00000	.00249
141	28.16188	1.00000	2.00000	.00264
142	28.04636	1.00000	2.00000	.00279
143	27.93084	1.00000	2.00000	.00294
144	27.83183	1.00000	2.00000	.00309
145	27.76582	1.00000	2.00000	.00324
146	27.76582	1.00000	2.00000	.00339
147	27.76582	1.00000	2.00000	.00354
148	27.69981	1.00000	2.00000	.00369
149	27.63380	1.00000	2.00000	.00384
150	27.58429	1.00000	2.00000	.00399
151	27.55128	1.00000	2.00000	.00415
152	27.55129	1.00000	2.00000	.00430
153	27.55129	1.00000	2.00000	.00445
154	27.51828	1.00000	2.00000	.00460
155	27.45227	1.00000	2.00000	.00475
156	27.38626	1.00000	2.00000	.00490
157	27.35325	1.00000	2.00000	.00505
158	27.32025	1.00000	2.00000	.00520
159	27.27074	1.00000	2.00000	.00535
160	27.25424	1.00000	2.00000	.00550
161	27.20473	1.00000	2.00000	.00565
162	27.12222	1.00000	2.00000	.00580
163	27.05621	1.00000	2.00000	.00595
164	27.02321	1.00000	2.00000	.00611
165	27.05621	1.00000	2.00000	.00626
166	27.03971	1.00000	2.00000	.00641
167	27.02321	1.00000	2.00000	.00656
168	27.00670	1.00000	2.00000	.00671
169	27.00670	1.00000	2.00000	.00686
170	27.00670	1.00000	2.00000	.00701
171	26.99020	1.00000	2.00000	.00716
172	26.94069	1.00000	2.00000	.00731
173	26.94069	1.00000	2.00000	.00746
174	26.94069	1.00000	2.00000	.00761
175	26.99020	1.00000	2.00000	.00776
176	26.95720	1.00000	2.00000	.00791
177	26.94069	1.00000	2.00000	.00806
178	26.87468	1.00000	2.00000	.00822

179	26.79217	1.00000	2.00000	.00837
180	26.79217	1.00000	2.00000	.00852
181	26.84168	1.00000	2.00000	.00867
182	26.84168	1.00000	2.00000	.00882
183	26.87468	1.00000	2.00000	.00897
184	26.87468	1.00000	2.00000	.00912
185	26.89119	1.00000	2.00000	.00927
186	26.84168	1.00000	2.00000	.00942
187	26.79217	1.00000	2.00000	.00957
188	26.77567	1.00000	2.00000	.00972
189	26.77567	1.00000	2.00000	.00987
190	26.75917	1.00000	2.00000	.01002
191	26.72616	1.00000	2.00000	.01018
192	26.67666	1.00000	2.00000	.01033
193	26.69316	1.00000	2.00000	.01048
194	26.70966	1.00000	2.00000	.01063
195	26.75917	1.00000	2.00000	.01078
196	26.72616	1.00000	2.00000	.01093
197	26.67666	1.00000	2.00000	.01108
198	26.66015	1.00000	2.00000	.01123
199	26.66015	1.00000	2.00000	.01138
200	26.66015	1.00000	2.00000	.01153
201	26.57764	1.00000	2.00000	.01168
202	26.59414	1.00000	2.00000	.01183
203	26.57764	1.00000	2.00000	.01198
204	26.61065	1.00000	2.00000	.01213
205	26.61065	1.00000	2.00000	.01229
206	26.64365	1.00000	2.00000	.01244
207	26.59414	1.00000	2.00000	.01259
208	26.52813	1.00000	2.00000	.01274
209	26.59414	1.00000	2.00000	.01289
210	26.62715	1.00000	2.00000	.01304
211	26.62715	1.00000	2.00000	.01319
212	26.62715	1.00000	2.00000	.01334
213	26.66015	1.00000	2.00000	.01349
214	26.59414	1.00000	2.00000	.01364
215	26.49513	1.00000	2.00000	.01379
216	26.49513	1.00000	2.00000	.01394
217	26.54464	1.00000	2.00000	.01409
218	26.56114	1.00000	2.00000	.01425
219	26.51163	1.00000	2.00000	.01440
220	26.54464	1.00000	2.00000	.01455
221	26.56114	1.00000	2.00000	.01470
222	26.57764	1.00000	2.00000	.01485
223	26.56114	1.00000	2.00000	.01500
224	26.56114	1.00000	2.00000	.01515
225	26.56114	1.00000	2.00000	.01530
226	26.59414	1.00000	2.00000	.01545
227	26.56114	1.00000	2.00000	.01560
228	26.52813	1.00000	2.00000	.01575
229	26.49513	1.00000	2.00000	.01590
230	26.52813	1.00000	2.00000	.01605
231	26.57764	1.00000	2.00000	.01620
232	26.52813	1.00000	2.00000	.01636
233	26.49513	1.00000	2.00000	.01651
234	26.44562	1.00000	2.00000	.01666
235	26.44562	1.00000	2.00000	.01681
236	26.49513	1.00000	2.00000	.01696
237	26.47863	1.00000	2.00000	.01711
238	26.42912	1.00000	2.00000	.01726
239	26.39611	1.00000	2.00000	.01741
240	26.47863	1.00000	2.00000	.01756
241	26.56114	1.00000	2.00000	.01771
242	26.57764	1.00000	2.00000	.01786
243	26.56114	1.00000	2.00000	.01801
244	26.51163	1.00000	2.00000	.01816
245	26.49513	1.00000	2.00000	.01832
246	26.47863	1.00000	2.00000	.01847
247	26.47863	1.00000	2.00000	.01862
248	26.49513	1.00000	2.00000	.01877
249	26.49513	1.00000	2.00000	.01892

250	26.54464	1.00000	2.00000	.01907
251	26.49513	1.00000	2.00000	.01922
252	26.39611	1.00000	2.00000	.01937
253	26.37961	1.00000	2.00000	.01952
254	26.37961	1.00000	2.00000	.01967
255	26.33010	1.00000	2.00000	.01982
256	26.28060	1.00000	2.00000	.01997
257	26.31360	1.00000	2.00000	.02012
258	26.36311	1.00000	2.00000	.02027
259	26.34661	1.00000	2.00000	.02043
260	26.31360	1.00000	2.00000	.02058
261	26.28060	1.00000	2.00000	.02073
262	26.26410	1.00000	2.00000	.02088
263	26.29710	1.00000	2.00000	.02103
264	26.36311	1.00000	2.00000	.02118
265	26.36311	1.00000	2.00000	.02133
266	26.31360	1.00000	2.00000	.02148
267	26.24759	1.00000	2.00000	.02163
268	26.21459	1.00000	2.00000	.02178
269	26.28060	1.00000	2.00000	.02193
270	26.39611	1.00000	2.00000	.02208
271	26.37961	1.00000	2.00000	.02223
272	26.31360	1.00000	2.00000	.02239
273	26.28060	1.00000	2.00000	.02254
274	26.29710	1.00000	2.00000	.02269
275	26.24759	1.00000	2.00000	.02284
276	26.21459	1.00000	2.00000	.02299
277	26.26410	1.00000	2.00000	.02314
278	26.23109	1.00000	2.00000	.02329
279	29.01296	1.00000	3.00000	.00249
280	28.93045	1.00000	3.00000	.00264
281	28.91395	1.00000	3.00000	.00279
282	28.93045	1.00000	3.00000	.00294
283	28.86444	1.00000	3.00000	.00309
284	28.83144	1.00000	3.00000	.00324
285	28.71592	1.00000	3.00000	.00339
286	28.63341	1.00000	3.00000	.00354
287	28.61690	1.00000	3.00000	.00369
288	28.53439	1.00000	3.00000	.00384
289	28.46838	1.00000	3.00000	.00399
290	28.45188	1.00000	3.00000	.00415
291	28.45188	1.00000	3.00000	.00430
292	28.38587	1.00000	3.00000	.00445
293	28.30336	1.00000	3.00000	.00460
294	28.23735	1.00000	3.00000	.00475
295	28.25385	1.00000	3.00000	.00490
296	28.22085	1.00000	3.00000	.00505
297	28.22085	1.00000	3.00000	.00520
298	28.22085	1.00000	3.00000	.00535
299	28.27035	1.00000	3.00000	.00550
300	28.23735	1.00000	3.00000	.00565
301	28.18784	1.00000	3.00000	.00580
302	28.13833	1.00000	3.00000	.00595
303	28.10533	1.00000	3.00000	.00611
304	28.12183	1.00000	3.00000	.00626
305	28.05582	1.00000	3.00000	.00641
306	28.02282	1.00000	3.00000	.00656
307	28.02282	1.00000	3.00000	.00671
308	27.98981	1.00000	3.00000	.00686
309	28.00632	1.00000	3.00000	.00701
310	27.97331	1.00000	3.00000	.00716
311	27.95681	1.00000	3.00000	.00731
312	27.92380	1.00000	3.00000	.00746
313	27.97331	1.00000	3.00000	.00761
314	27.97331	1.00000	3.00000	.00776
315	27.94031	1.00000	3.00000	.00791
316	27.92380	1.00000	3.00000	.00806
317	27.92380	1.00000	3.00000	.00822
318	27.90730	1.00000	3.00000	.00837
319	27.87430	1.00000	3.00000	.00852
320	27.80829	1.00000	3.00000	.00867

321	27.79178	1.00000	3.00000	.00882
322	27.87430	1.00000	3.00000	.00897
323	27.92380	1.00000	3.00000	.00912
324	27.92380	1.00000	3.00000	.00927
325	27.90730	1.00000	3.00000	.00942
326	27.87430	1.00000	3.00000	.00957
327	27.85779	1.00000	3.00000	.00972
328	27.84129	1.00000	3.00000	.00987
329	27.85779	1.00000	3.00000	.01002
330	27.82479	1.00000	3.00000	.01018
331	27.80829	1.00000	3.00000	.01033
332	27.79178	1.00000	3.00000	.01048
333	27.77528	1.00000	3.00000	.01063
334	27.72578	1.00000	3.00000	.01078
335	27.72578	1.00000	3.00000	.01093
336	27.74228	1.00000	3.00000	.01108
337	27.70927	1.00000	3.00000	.01123
338	27.69277	1.00000	3.00000	.01138
339	27.65976	1.00000	3.00000	.01153
340	27.67627	1.00000	3.00000	.01168
341	27.64326	1.00000	3.00000	.01183
342	27.62676	1.00000	3.00000	.01198
343	27.67627	1.00000	3.00000	.01213
344	27.64326	1.00000	3.00000	.01229
345	27.59375	1.00000	3.00000	.01244
346	27.56075	1.00000	3.00000	.01259
347	27.57725	1.00000	3.00000	.01274
348	27.57725	1.00000	3.00000	.01289
349	27.54424	1.00000	3.00000	.01304
350	27.56075	1.00000	3.00000	.01319
351	27.56075	1.00000	3.00000	.01334
352	27.57725	1.00000	3.00000	.01349
353	27.56075	1.00000	3.00000	.01364
354	27.54425	1.00000	3.00000	.01379
355	27.56075	1.00000	3.00000	.01394
356	27.52774	1.00000	3.00000	.01409
357	27.51124	1.00000	3.00000	.01425
358	27.52774	1.00000	3.00000	.01440
359	27.56075	1.00000	3.00000	.01455
360	27.57725	1.00000	3.00000	.01470
361	27.61026	1.00000	3.00000	.01485
362	27.62676	1.00000	3.00000	.01500
363	27.54424	1.00000	3.00000	.01515
364	27.47824	1.00000	3.00000	.01530
365	27.47824	1.00000	3.00000	.01545
366	27.51124	1.00000	3.00000	.01560
367	27.54424	1.00000	3.00000	.01575
368	27.56075	1.00000	3.00000	.01590
369	27.59375	1.00000	3.00000	.01605
370	27.61026	1.00000	3.00000	.01620
371	27.54424	1.00000	3.00000	.01636
372	27.47824	1.00000	3.00000	.01651
373	27.49474	1.00000	3.00000	.01666
374	27.52774	1.00000	3.00000	.01681
375	27.49474	1.00000	3.00000	.01696
376	27.41223	1.00000	3.00000	.01711
377	27.42873	1.00000	3.00000	.01726
378	27.39572	1.00000	3.00000	.01741
379	27.37922	1.00000	3.00000	.01756
380	27.39572	1.00000	3.00000	.01771
381	27.44523	1.00000	3.00000	.01786
382	27.46173	1.00000	3.00000	.01801
383	27.42873	1.00000	3.00000	.01816
384	27.39572	1.00000	3.00000	.01832
385	27.44523	1.00000	3.00000	.01847
386	27.46173	1.00000	3.00000	.01862
387	27.44523	1.00000	3.00000	.01877
388	27.42873	1.00000	3.00000	.01892
389	27.44523	1.00000	3.00000	.01907
390	27.46173	1.00000	3.00000	.01922
391	27.42873	1.00000	3.00000	.01937

```
   392 27.37922  1.00000  3.00000   .01952
   393 27.42873  1.00000  3.00000   .01967
   394 27.49474  1.00000  3.00000   .01982
   395 27.44523  1.00000  3.00000   .01997
   396 27.34622  1.00000  3.00000   .02012
   397 27.37922  1.00000  3.00000   .02027
   398 27.42873  1.00000  3.00000   .02043
   399 27.41223  1.00000  3.00000   .02058
   400 27.37922  1.00000  3.00000   .02073
   401 27.41223  1.00000  3.00000   .02088
   402 27.44523  1.00000  3.00000   .02103
   403 27.41223  1.00000  3.00000   .02118
   404 27.37922  1.00000  3.00000   .02133
   405 27.42873  1.00000  3.00000   .02148
   406 27.42873  1.00000  3.00000   .02163
   407 27.37922  1.00000  3.00000   .02178
   408 27.39572  1.00000  3.00000   .02193
   409 27.46173  1.00000  3.00000   .02208
   410 27.46173  1.00000  3.00000   .02223
   411 27.41223  1.00000  3.00000   .02239
   412 27.39572  1.00000  3.00000   .02254
   413 27.39572  1.00000  3.00000   .02269
   414 27.37922  1.00000  3.00000   .02284
   415 27.34622  1.00000  3.00000   .02299
   416 27.31321  1.00000  3.00000   .02314
   417 27.31321  1.00000  3.00000   .02329

BLOCK 4
IEXTRA = NO. OF EXTRA(I) PARAMETERS. 0 IF NONE

     IEXTRA =       2

BLOCK 5
EXTRA(1),... ARE EXTRA CONSTANTS USED AS DESIRED

EXTRA( 1) =        .00050
EXTRA( 2) =        .02540
END INPUT QUANTITIES - - BEGIN OUTPUT CALCULATIONS

SY =  SUM OF SQUARES FOR PRESENT PARAMETER VALUES
SYP = SUM OF SQUARES FOR GAUSS PARAMETER VALUES, SHOULD BE SMALLER THAN SY
   SYP DECREASES TOWARD A POSITIVE CONSTANT
G =  MEASURE OF THE SLOPE, SHOULD BECOME SMALLER AS  ITERATIONS PROCEED
   G SHOULD APPROACH ZERO AT CONVERGENCE
H =  FRACTION OF THE GAUSS STEP, AS GIVEN BY THE    BOX-KANEMASU METHOD


  MAX      H        G        SY        SYP
   1   1.000041  .424764E+03  .427074E+03  .229201E+01
     B(1) =    .173125E+01
     B(2) =    .397739E-03
     B(3) =    .243881E+02

  P(1,KP)      P(2,KP)      P(3,KP)      P(4,KP)      P(5,KP)
 .4171636D-01 -.8303156D-05 -.4902552D-02
-.8303156D-05  .2024217D-08 -.1333698D-05
-.4902552D-02 -.1333698D-05  .1732886D-01
  CORRELATION MATRIX
 .1000000E+01
-.9035692E+00  .1000000E+01
-.1823409E+00 -.2251873E+00  .1000000E+01
XTX(I,K),K=1,NP
 .8955616E+03  .4046721E+07  .5648878E+03
 .4046721E+07  .1879476E+11  .2591869E+07
 .5648878E+03  .2591869E+07  .4170000E+03
XTY(I),I=1,NP, WHERE Y IS RESID
-.6000147E+03 -.2736183E+07 -.4156496E+03
XTY(I),I=1,NP, Y IS Y, NOT RESID
-.2038851E+01 -.1093333E+05 -.1172693E+01
   MAX      NP    INDEX      IP
    1       3      0       4
```

```
   MAX      NP    INDEX      IP
    2       3       1       3
  MAX       H         G        SY        SYP
   2     .999196  .191240E-02  .229194E+01  .229003E+01
     B(1) =     .172848E+01
     B(2) =     .398018E-03
     B(3) =     .243884E+02

  P(1,KP)      P(2,KP)      P(3,KP)      P(4,KP)      P(5,KP)
 .4259919D-01 -.9786584D-05 -.4885013D-02
-.9786584D-05  .2747824D-08 -.1558354D-05
-.4885013D-02 -.1558354D-05  .1734423D-01
  CORRELATION MATRIX
 .1000000E+01
-.9045571E+00  .1000000E+01
-.1797163E+00 -.2257326E+00  .1000000E+01
XTX(I,K),K=1,NP
 .8864573E+03  .3475908E+07  .5619645E+03
 .3475908E+07  .1401292E+11  .2237994E+07
 .5619645E+03  .2237994E+07  .4170000E+03
XTY(I),I=1,NP, WHERE Y IS RESID
-.1286398E+01 -.4925585E+04 -.7841158E+00
XTY(I),I=1,NP, Y IS Y, NOT RESID
-.1151528E+00 -.5364410E+03 -.6663583E-01
   MAX      NP    INDEX      IP
    2       3       1       4
   MAX      NP    INDEX      IP
    3       3       1       1
   MAX      NP    INDEX      IP
    3       3       2       2
   MAX      NP    INDEX      IP
    3       3       3       3
  MAX       H         G        SY        SYP
   3    1.000000  .412786E-07  .229003E+01  .229003E+01
     B(1) =     .172850E+01
     B(2) =     .398007E-03
     B(3) =     .243885E+02

  P(1,KP)      P(2,KP)      P(3,KP)      P(4,KP)      P(5,KP)
 .4260317D-01 -.9810796D-05 -.4880215D-02
-.9810796D-05  .2760675D-08 -.1563382D-05
-.4880215D-02 -.1563382D-05  .1735952D-01
  CORRELATION MATRIX
 .1000000E+01
-.9046397E+00  .1000000E+01
-.1794523E+00 -.2258336E+00  .1000000E+01
XTX(I,K),K=1,NP
 .8875802E+03  .3472610E+07  .5623259E+03
 .3472610E+07  .1396815E+11  .2234416E+07
 .5623259E+03  .2234416E+07  .4170000E+03
XTY(I),I=1,NP, WHERE Y IS RESID
 .1574945E-02  .5687588E+01  .1635058E-02
XTY(I),I=1,NP, Y IS Y, NOT RESID
-.1114548E+00 -.5179943E+03 -.6444745E-01
   MAX      NP    INDEX      IP
    3       3       3       4

SEQUENTIAL ESTIMATES OF THE PARAMETERS GIVEN BELOW


 I    ETA  RES.  B(1)      B(2)      B(3)      B(4)
 1   26.82  .006 .1732E+01 .3984E-03 .2439E+02
 2   26.77  .024 .1144E+01 .5628E-03 .2478E+02
 3   26.72  .005 .1743E+01 .3962E-03 .2438E+02
 4   26.68  .000 .1854E+01 .3657E-03 .2431E+02
 5   26.63 -.056 .2264E+01 .2532E-03 .2405E+02
 6   26.59 -.049 .2284E+01 .2477E-03 .2404E+02
 7   26.55 -.059 .2286E+01 .2473E-03 .2403E+02
 8   26.52 -.056 .2236E+01 .2606E-03 .2407E+02
 9   26.48 -.070 .2222E+01 .2645E-03 .2408E+02
10   26.45 -.085 .2227E+01 .2632E-03 .2407E+02
```

11	26.42	-.053	.2154E+01	.2825E-03	.2412E+02
12	26.38	-.038	.2074E+01	.3035E-03	.2417E+02
13	26.35	-.058	.2041E+01	.3121E-03	.2419E+02
14	26.33	-.078	.2038E+01	.3130E-03	.2419E+02
15	26.30	-.083	.2036E+01	.3136E-03	.2419E+02
16	26.27	-.090	.2035E+01	.3136E-03	.2419E+02
17	26.25	-.097	.2037E+01	.3132E-03	.2419E+02
18	26.22	-.055	.2003E+01	.3220E-03	.2421E+02
19	26.20	-.063	.1980E+01	.3278E-03	.2422E+02
20	26.17	-.040	.1945E+01	.3366E-03	.2424E+02
21	26.15	-.017	.1903E+01	.3473E-03	.2427E+02
22	26.13	-.011	.1865E+01	.3568E-03	.2429E+02
23	26.11	-.056	.1856E+01	.3589E-03	.2430E+02
24	26.08	-.084	.1863E+01	.3573E-03	.2429E+02
25	26.06	-.047	.1851E+01	.3603E-03	.2430E+02
26	26.04	-.044	.1839E+01	.3633E-03	.2431E+02
27	26.02	-.074	.1840E+01	.3629E-03	.2431E+02
28	26.01	-.088	.1846E+01	.3614E-03	.2430E+02
29	25.99	-.120	.1862E+01	.3577E-03	.2429E+02
30	25.97	-.102	.1868E+01	.3560E-03	.2429E+02
31	25.95	-.084	.1868E+01	.3560E-03	.2429E+02
32	25.94	-.034	.1853E+01	.3597E-03	.2430E+02
33	25.92	-.018	.1835E+01	.3641E-03	.2431E+02
34	25.90	-.035	.1823E+01	.3668E-03	.2432E+02
35	25.89	-.052	.1818E+01	.3682E-03	.2432E+02
36	25.87	-.053	.1813E+01	.3694E-03	.2432E+02
37	25.86	-.054	.1808E+01	.3704E-03	.2432E+02
38	25.84	-.007	.1794E+01	.3738E-03	.2433E+02
39	25.83	.024	.1774E+01	.3784E-03	.2434E+02
40	25.81	.005	.1761E+01	.3816E-03	.2435E+02
41	25.80	-.064	.1762E+01	.3813E-03	.2435E+02
42	25.79	-.116	.1773E+01	.3786E-03	.2434E+02
43	25.77	-.054	.1772E+01	.3790E-03	.2434E+02
44	25.76	-.008	.1762E+01	.3812E-03	.2435E+02
45	25.75	.005	.1752E+01	.3836E-03	.2435E+02
46	25.74	.067	.1732E+01	.3882E-03	.2437E+02
47	25.72	.079	.1711E+01	.3928E-03	.2438E+02
48	25.71	.041	.1699E+01	.3957E-03	.2438E+02
49	25.70	.003	.1693E+01	.3969E-03	.2439E+02
50	25.69	.014	.1687E+01	.3985E-03	.2439E+02
51	25.68	.009	.1681E+01	.3997E-03	.2439E+02
52	25.67	.036	.1673E+01	.4016E-03	.2440E+02
53	25.66	.014	.1668E+01	.4027E-03	.2440E+02
54	25.65	-.025	.1669E+01	.4026E-03	.2440E+02
55	25.64	-.097	.1678E+01	.4004E-03	.2439E+02
56	25.63	-.071	.1684E+01	.3991E-03	.2439E+02
57	25.62	.021	.1678E+01	.4004E-03	.2439E+02
58	25.61	.015	.1674E+01	.4014E-03	.2440E+02
59	25.60	-.026	.1674E+01	.4012E-03	.2440E+02
60	25.59	-.049	.1677E+01	.4006E-03	.2439E+02
61	25.58	.009	.1674E+01	.4013E-03	.2440E+02
62	25.57	.051	.1667E+01	.4029E-03	.2440E+02
63	25.56	-.039	.1669E+01	.4025E-03	.2440E+02
64	25.55	-.113	.1678E+01	.4004E-03	.2439E+02
65	25.54	-.105	.1686E+01	.3986E-03	.2439E+02
66	25.54	-.080	.1692E+01	.3975E-03	.2439E+02
67	25.53	-.072	.1696E+01	.3966E-03	.2439E+02
68	25.52	-.081	.1700E+01	.3956E-03	.2438E+02
69	25.51	-.073	.1704E+01	.3948E-03	.2438E+02
70	25.50	-.065	.1707E+01	.3942E-03	.2438E+02
71	25.50	.008	.1704E+01	.3949E-03	.2438E+02
72	25.49	-.018	.1703E+01	.3951E-03	.2438E+02
73	25.48	-.093	.1708E+01	.3941E-03	.2438E+02
74	25.48	-.086	.1712E+01	.3932E-03	.2438E+02
75	25.47	-.079	.1715E+01	.3924E-03	.2438E+02
76	25.46	-.039	.1716E+01	.3924E-03	.2438E+02
77	25.46	-.066	.1718E+01	.3919E-03	.2437E+02
78	25.45	-.059	.1719E+01	.3916E-03	.2437E+02
79	25.44	-.036	.1719E+01	.3916E-03	.2437E+02
80	25.44	-.080	.1722E+01	.3910E-03	.2437E+02
81	25.43	-.090	.1726E+01	.3902E-03	.2437E+02

82	25.42	-.068	.1728E+01	.3899E-03	.2437E+02
83	25.42	-.029	.1727E+01	.3900E-03	.2437E+02
84	25.41	-.023	.1726E+01	.3903E-03	.2437E+02
85	25.41	-.084	.1728E+01	.3897E-03	.2437E+02
86	25.40	-.062	.1730E+01	.3894E-03	.2437E+02
87	25.40	.026	.1725E+01	.3903E-03	.2437E+02
88	25.39	.015	.1722E+01	.3910E-03	.2437E+02
89	25.39	-.029	.1721E+01	.3911E-03	.2437E+02
90	25.38	-.090	.1724E+01	.3905E-03	.2437E+02
91	25.38	-.151	.1731E+01	.3892E-03	.2437E+02
92	25.37	-.147	.1737E+01	.3880E-03	.2436E+02
93	25.37	-.076	.1739E+01	.3876E-03	.2436E+02
94	25.36	-.055	.1739E+01	.3875E-03	.2436E+02
95	25.36	-.067	.1740E+01	.3873E-03	.2436E+02
96	25.35	-.079	.1742E+01	.3870E-03	.2436E+02
97	25.35	-.108	.1745E+01	.3863E-03	.2436E+02
98	25.34	-.136	.1750E+01	.3854E-03	.2436E+02
99	25.34	-.083	.1751E+01	.3851E-03	.2436E+02
100	25.34	.020	.1747E+01	.3858E-03	.2436E+02
101	25.33	.041	.1743E+01	.3867E-03	.2436E+02
102	25.33	-.021	.1741E+01	.3870E-03	.2436E+02
103	25.32	-.034	.1741E+01	.3872E-03	.2436E+02
104	25.32	-.031	.1740E+01	.3873E-03	.2436E+02
105	25.32	.055	.1735E+01	.3883E-03	.2437E+02
106	25.31	.108	.1728E+01	.3897E-03	.2437E+02
107	25.31	.062	.1723E+01	.3907E-03	.2437E+02
108	25.31	.049	.1719E+01	.3915E-03	.2437E+02
109	25.30	.052	.1715E+01	.3923E-03	.2437E+02
110	25.30	.105	.1709E+01	.3935E-03	.2438E+02
111	25.30	.157	.1701E+01	.3951E-03	.2438E+02
112	25.30	.061	.1697E+01	.3959E-03	.2438E+02
113	25.29	-.002	.1696E+01	.3961E-03	.2438E+02
114	25.29	.067	.1692E+01	.3968E-03	.2439E+02
115	25.29	.152	.1685E+01	.3983E-03	.2439E+02
116	25.28	.105	.1680E+01	.3993E-03	.2439E+02
117	25.28	.108	.1675E+01	.4003E-03	.2439E+02
118	25.28	.127	.1669E+01	.4014E-03	.2440E+02
119	25.28	.146	.1663E+01	.4026E-03	.2440E+02
120	25.27	.098	.1659E+01	.4034E-03	.2440E+02
121	25.27	.051	.1656E+01	.4039E-03	.2440E+02
122	25.27	.037	.1655E+01	.4042E-03	.2440E+02
123	25.27	.072	.1652E+01	.4047E-03	.2440E+02
124	25.27	.090	.1648E+01	.4054E-03	.2441E+02
125	25.26	.026	.1647E+01	.4056E-03	.2441E+02
126	25.26	.012	.1647E+01	.4057E-03	.2441E+02
127	25.26	.079	.1644E+01	.4063E-03	.2441E+02
128	25.26	.114	.1640E+01	.4071E-03	.2441E+02
129	25.26	.066	.1638E+01	.4075E-03	.2441E+02
130	25.26	.068	.1636E+01	.4079E-03	.2441E+02
131	25.25	.069	.1633E+01	.4083E-03	.2441E+02
132	25.25	.038	.1632E+01	.4086E-03	.2441E+02
133	25.25	.022	.1632E+01	.4087E-03	.2441E+02
134	25.25	-.009	.1632E+01	.4086E-03	.2441E+02
135	25.25	-.058	.1634E+01	.4082E-03	.2441E+02
136	25.25	-.057	.1636E+01	.4078E-03	.2441E+02
137	25.25	-.055	.1638E+01	.4075E-03	.2441E+02
138	25.25	-.071	.1640E+01	.4070E-03	.2441E+02
139	25.24	-.087	.1643E+01	.4065E-03	.2441E+02
140	27.89	.343	.1643E+01	.5746E-03	.2396E+02
141	27.84	.327	.1643E+01	.5712E-03	.2397E+02
142	27.79	.259	.1643E+01	.5611E-03	.2399E+02
143	27.74	.188	.1644E+01	.5491E-03	.2403E+02
144	27.70	.132	.1645E+01	.5372E-03	.2406E+02
145	27.66	.106	.1646E+01	.5274E-03	.2408E+02
146	27.62	.145	.1647E+01	.5223E-03	.2410E+02
147	27.58	.182	.1647E+01	.5203E-03	.2410E+02
148	27.55	.151	.1648E+01	.5171E-03	.2411E+02
149	27.51	.119	.1649E+01	.5131E-03	.2412E+02
150	27.48	.102	.1651E+01	.5090E-03	.2413E+02
151	27.45	.100	.1652E+01	.5054E-03	.2414E+02
152	27.42	.130	.1653E+01	.5033E-03	.2414E+02

153	27.39	.159	.1653E+01	.5024E-03	.2414E+02
154	27.36	.154	.1654E+01	.5014E-03	.2415E+02
155	27.34	.115	.1655E+01	.4992E-03	.2415E+02
156	27.31	.075	.1657E+01	.4961E-03	.2416E+02
157	27.29	.067	.1659E+01	.4930E-03	.2416E+02
158	27.26	.058	.1661E+01	.4899E-03	.2417E+02
159	27.24	.033	.1664E+01	.4863E-03	.2418E+02
160	27.22	.039	.1667E+01	.4832E-03	.2419E+02
161	27.19	.012	.1670E+01	.4796E-03	.2419E+02
162	27.17	-.049	.1674E+01	.4747E-03	.2420E+02
163	27.15	-.094	.1679E+01	.4691E-03	.2421E+02
164	27.13	-.107	.1684E+01	.4635E-03	.2423E+02
165	27.11	-.054	.1688E+01	.4595E-03	.2423E+02
166	27.09	-.051	.1692E+01	.4558E-03	.2424E+02
167	27.07	-.049	.1696E+01	.4524E-03	.2425E+02
168	27.05	-.047	.1699E+01	.4492E-03	.2425E+02
169	27.04	-.029	.1702E+01	.4465E-03	.2426E+02
170	27.02	-.012	.1705E+01	.4444E-03	.2426E+02
171	27.00	-.012	.1707E+01	.4424E-03	.2427E+02
172	26.99	-.044	.1710E+01	.4398E-03	.2427E+02
173	26.97	-.028	.1713E+01	.4377E-03	.2427E+02
174	26.95	-.013	.1715E+01	.4359E-03	.2428E+02
175	26.94	.052	.1716E+01	.4355E-03	.2428E+02
176	26.92	.034	.1717E+01	.4348E-03	.2428E+02
177	26.91	.033	.1717E+01	.4341E-03	.2428E+02
178	26.89	-.019	.1720E+01	.4325E-03	.2428E+02
179	26.88	-.088	.1724E+01	.4297E-03	.2429E+02
180	26.87	-.074	.1727E+01	.4272E-03	.2429E+02
181	26.85	-.011	.1729E+01	.4260E-03	.2429E+02
182	26.84	.002	.1730E+01	.4251E-03	.2429E+02
183	26.83	.048	.1731E+01	.4250E-03	.2429E+02
184	26.81	.061	.1730E+01	.4251E-03	.2429E+02
185	26.80	.089	.1729E+01	.4257E-03	.2429E+02
186	26.79	.052	.1729E+01	.4256E-03	.2429E+02
187	26.78	.014	.1731E+01	.4250E-03	.2429E+02
188	26.77	.009	.1732E+01	.4242E-03	.2430E+02
189	26.75	.021	.1733E+01	.4237E-03	.2430E+02
190	26.74	.015	.1733E+01	.4232E-03	.2430E+02
191	26.73	-.007	.1735E+01	.4223E-03	.2430E+02
192	26.72	-.046	.1737E+01	.4208E-03	.2430E+02
193	26.71	-.019	.1739E+01	.4198E-03	.2430E+02
194	26.70	.008	.1740E+01	.4192E-03	.2430E+02
195	26.69	.067	.1739E+01	.4196E-03	.2430E+02
196	26.68	.044	.1739E+01	.4196E-03	.2430E+02
197	26.67	.004	.1740E+01	.4190E-03	.2430E+02
198	26.66	-.003	.1742E+01	.4183E-03	.2430E+02
199	26.65	.007	.1743E+01	.4178E-03	.2431E+02
200	26.64	.016	.1743E+01	.4175E-03	.2431E+02
201	26.64	-.058	.1746E+01	.4161E-03	.2431E+02
202	26.63	-.033	.1748E+01	.4151E-03	.2431E+02
203	26.62	-.041	.1749E+01	.4141E-03	.2431E+02
204	26.61	.001	.1750E+01	.4136E-03	.2431E+02
205	26.60	.009	.1751E+01	.4133E-03	.2431E+02
206	26.59	.050	.1751E+01	.4135E-03	.2431E+02
207	26.59	.008	.1751E+01	.4132E-03	.2431E+02
208	26.58	-.050	.1753E+01	.4121E-03	.2431E+02
209	26.57	.024	.1753E+01	.4120E-03	.2431E+02
210	26.56	.064	.1753E+01	.4124E-03	.2431E+02
211	26.56	.071	.1752E+01	.4129E-03	.2431E+02
212	26.55	.078	.1750E+01	.4135E-03	.2431E+02
213	26.54	.118	.1748E+01	.4145E-03	.2431E+02
214	26.53	.059	.1748E+01	.4148E-03	.2431E+02
215	26.53	-.033	.1749E+01	.4140E-03	.2431E+02
216	26.52	-.026	.1751E+01	.4133E-03	.2431E+02
217	26.52	.030	.1751E+01	.4133E-03	.2431E+02
218	26.51	.052	.1750E+01	.4135E-03	.2431E+02
219	26.50	.009	.1751E+01	.4132E-03	.2431E+02
220	26.50	.048	.1751E+01	.4134E-03	.2431E+02
221	26.49	.071	.1750E+01	.4139E-03	.2431E+02
222	26.48	.093	.1748E+01	.4145E-03	.2431E+02
223	26.48	.082	.1747E+01	.4150E-03	.2431E+02

224	26.47	.088	.1746E+01	.4156E-03	.2431E+02
225	26.47	.093	.1745E+01	.4162E-03	.2431E+02
226	26.46	.132	.1743E+01	.4172E-03	.2431E+02
227	26.46	.104	.1741E+01	.4179E-03	.2431E+02
228	26.45	.076	.1740E+01	.4182E-03	.2431E+02
229	26.45	.048	.1740E+01	.4183E-03	.2431E+02
230	26.44	.086	.1739E+01	.4188E-03	.2431E+02
231	26.44	.140	.1737E+01	.4198E-03	.2430E+02
232	26.43	.095	.1736E+01	.4203E-03	.2430E+02
233	26.43	.067	.1735E+01	.4205E-03	.2430E+02
234	26.42	.022	.1736E+01	.4203E-03	.2430E+02
235	26.42	.027	.1736E+01	.4202E-03	.2430E+02
236	26.41	.080	.1735E+01	.4205E-03	.2430E+02
237	26.41	.068	.1735E+01	.4207E-03	.2430E+02
238	26.41	.023	.1735E+01	.4205E-03	.2430E+02
239	26.40	-.006	.1736E+01	.4201E-03	.2430E+02
240	26.40	.080	.1736E+01	.4204E-03	.2430E+02
241	26.39	.166	.1733E+01	.4215E-03	.2430E+02
242	26.39	.187	.1730E+01	.4228E-03	.2430E+02
243	26.39	.174	.1728E+01	.4239E-03	.2430E+02
244	26.38	.128	.1726E+01	.4245E-03	.2430E+02
245	26.38	.115	.1725E+01	.4251E-03	.2430E+02
246	26.38	.102	.1724E+01	.4255E-03	.2430E+02
247	26.37	.105	.1723E+01	.4260E-03	.2430E+02
248	26.37	.125	.1722E+01	.4266E-03	.2430E+02
249	26.37	.128	.1720E+01	.4272E-03	.2430E+02
250	26.36	.180	.1718E+01	.4282E-03	.2430E+02
251	26.36	.134	.1716E+01	.4288E-03	.2429E+02
252	26.36	.038	.1717E+01	.4286E-03	.2430E+02
253	26.36	.024	.1717E+01	.4284E-03	.2430E+02
254	26.35	.026	.1718E+01	.4281E-03	.2430E+02
255	26.35	-.020	.1719E+01	.4275E-03	.2430E+02
256	26.35	-.067	.1722E+01	.4266E-03	.2430E+02
257	26.35	-.032	.1723E+01	.4260E-03	.2430E+02
258	26.34	.020	.1724E+01	.4257E-03	.2430E+02
259	26.34	.006	.1725E+01	.4254E-03	.2430E+02
260	26.34	-.025	.1726E+01	.4248E-03	.2430E+02
261	26.34	-.056	.1728E+01	.4240E-03	.2430E+02
262	26.33	-.070	.1730E+01	.4232E-03	.2430E+02
263	26.33	-.035	.1731E+01	.4226E-03	.2430E+02
264	26.33	.033	.1731E+01	.4225E-03	.2430E+02
265	26.33	.034	.1732E+01	.4224E-03	.2430E+02
266	26.33	-.013	.1733E+01	.4220E-03	.2430E+02
267	26.33	-.078	.1735E+01	.4211E-03	.2430E+02
268	26.32	-.109	.1737E+01	.4201E-03	.2430E+02
269	26.32	-.041	.1739E+01	.4195E-03	.2430E+02
270	26.32	.075	.1738E+01	.4197E-03	.2430E+02
271	26.32	.060	.1738E+01	.4199E-03	.2430E+02
272	26.32	-.004	.1739E+01	.4196E-03	.2430E+02
273	26.32	-.036	.1740E+01	.4191E-03	.2430E+02
274	26.32	-.018	.1741E+01	.4187E-03	.2430E+02
275	26.31	-.067	.1742E+01	.4180E-03	.2430E+02
276	26.31	-.099	.1744E+01	.4171E-03	.2431E+02
277	26.31	-.048	.1746E+01	.4166E-03	.2431E+02
278	26.31	-.080	.1748E+01	.4159E-03	.2431E+02
279	28.95	.061	.1745E+01	.4160E-03	.2431E+02
280	28.90	.029	.1743E+01	.4161E-03	.2431E+02
281	28.85	.060	.1741E+01	.4161E-03	.2431E+02
282	28.81	.122	.1742E+01	.4161E-03	.2431E+02
283	28.77	.098	.1742E+01	.4161E-03	.2431E+02
284	28.73	.106	.1742E+01	.4161E-03	.2431E+02
285	28.69	.029	.1740E+01	.4161E-03	.2431E+02
286	28.65	-.017	.1738E+01	.4160E-03	.2432E+02
287	28.62	.002	.1736E+01	.4159E-03	.2432E+02
288	28.58	-.047	.1734E+01	.4157E-03	.2432E+02
289	28.55	-.080	.1731E+01	.4154E-03	.2432E+02
290	28.52	-.066	.1729E+01	.4151E-03	.2433E+02
291	28.49	-.036	.1727E+01	.4149E-03	.2433E+02
292	28.46	-.073	.1726E+01	.4146E-03	.2433E+02
293	28.43	-.127	.1723E+01	.4141E-03	.2434E+02
294	28.40	-.166	.1721E+01	.4136E-03	.2434E+02

295	28.38	-.124	.1720E+01	.4131E-03	.2434E+02
296	28.35	-.132	.1718E+01	.4125E-03	.2435E+02
297	28.33	-.107	.1717E+01	.4121E-03	.2435E+02
298	28.30	-.084	.1716E+01	.4116E-03	.2435E+02
299	28.28	-.011	.1716E+01	.4115E-03	.2435E+02
300	28.26	-.022	.1716E+01	.4112E-03	.2435E+02
301	28.24	-.050	.1716E+01	.4109E-03	.2435E+02
302	28.22	-.079	.1715E+01	.4105E-03	.2436E+02
303	28.20	-.091	.1715E+01	.4100E-03	.2436E+02
304	28.18	-.055	.1715E+01	.4097E-03	.2436E+02
305	28.16	-.101	.1715E+01	.4091E-03	.2436E+02
306	28.14	-.116	.1715E+01	.4085E-03	.2436E+02
307	28.12	-.097	.1715E+01	.4080E-03	.2437E+02
308	28.10	-.113	.1715E+01	.4074E-03	.2437E+02
309	28.09	-.079	.1715E+01	.4070E-03	.2437E+02
310	28.07	-.095	.1715E+01	.4065E-03	.2437E+02
311	28.05	-.095	.1716E+01	.4060E-03	.2437E+02
312	28.04	-.112	.1716E+01	.4054E-03	.2437E+02
313	28.02	-.046	.1716E+01	.4051E-03	.2437E+02
314	28.00	-.031	.1716E+01	.4049E-03	.2438E+02
315	27.99	-.049	.1717E+01	.4046E-03	.2438E+02
316	27.97	-.051	.1717E+01	.4043E-03	.2438E+02
317	27.96	-.036	.1717E+01	.4040E-03	.2438E+02
318	27.95	-.039	.1718E+01	.4038E-03	.2438E+02
319	27.93	-.058	.1718E+01	.4034E-03	.2438E+02
320	27.92	-.111	.1719E+01	.4028E-03	.2438E+02
321	27.91	-.114	.1719E+01	.4022E-03	.2438E+02
322	27.89	-.019	.1720E+01	.4021E-03	.2438E+02
323	27.88	.043	.1719E+01	.4023E-03	.2438E+02
324	27.87	.056	.1719E+01	.4025E-03	.2438E+02
325	27.86	.051	.1719E+01	.4027E-03	.2438E+02
326	27.84	.030	.1719E+01	.4028E-03	.2438E+02
327	27.83	.025	.1719E+01	.4029E-03	.2438E+02
328	27.82	.020	.1718E+01	.4029E-03	.2438E+02
329	27.81	.048	.1718E+01	.4031E-03	.2438E+02
330	27.80	.025	.1718E+01	.4032E-03	.2438E+02
331	27.79	.020	.1718E+01	.4032E-03	.2438E+02
332	27.78	.013	.1718E+01	.4032E-03	.2438E+02
333	27.77	.007	.1718E+01	.4032E-03	.2438E+02
334	27.76	-.032	.1718E+01	.4030E-03	.2438E+02
335	27.75	-.022	.1719E+01	.4028E-03	.2438E+02
336	27.74	.004	.1719E+01	.4027E-03	.2438E+02
337	27.73	-.020	.1719E+01	.4026E-03	.2438E+02
338	27.72	-.027	.1720E+01	.4024E-03	.2438E+02
339	27.71	-.051	.1720E+01	.4021E-03	.2438E+02
340	27.70	-.026	.1721E+01	.4019E-03	.2438E+02
341	27.69	-.050	.1721E+01	.4016E-03	.2438E+02
342	27.68	-.058	.1722E+01	.4012E-03	.2438E+02
343	27.68	.000	.1722E+01	.4012E-03	.2438E+02
344	27.67	-.025	.1722E+01	.4010E-03	.2438E+02
345	27.66	-.066	.1723E+01	.4006E-03	.2438E+02
346	27.65	-.092	.1724E+01	.4001E-03	.2439E+02
347	27.64	-.067	.1725E+01	.3997E-03	.2439E+02
348	27.64	-.060	.1726E+01	.3994E-03	.2439E+02
349	27.63	-.085	.1727E+01	.3989E-03	.2439E+02
350	27.62	-.062	.1727E+01	.3986E-03	.2439E+02
351	27.62	-.054	.1728E+01	.3983E-03	.2439E+02
352	27.61	-.031	.1728E+01	.3982E-03	.2439E+02
353	27.60	-.040	.1729E+01	.3980E-03	.2439E+02
354	27.59	-.050	.1729E+01	.3977E-03	.2439E+02
355	27.59	-.027	.1730E+01	.3976E-03	.2439E+02
356	27.58	-.054	.1730E+01	.3973E-03	.2439E+02
357	27.58	-.064	.1731E+01	.3970E-03	.2439E+02
358	27.57	-.041	.1732E+01	.3968E-03	.2439E+02
359	27.56	-.002	.1732E+01	.3968E-03	.2439E+02
360	27.56	.020	.1731E+01	.3969E-03	.2439E+02
361	27.55	.059	.1731E+01	.3972E-03	.2439E+02
362	27.55	.081	.1730E+01	.3976E-03	.2439E+02
363	27.54	.005	.1729E+01	.3976E-03	.2439E+02
364	27.53	-.056	.1730E+01	.3974E-03	.2439E+02
365	27.53	-.051	.1731E+01	.3971E-03	.2439E+02

```
366   27.52  -.012 .1731E+01 .3971E-03 .2439E+02
367   27.52   .026 .1731E+01 .3972E-03 .2439E+02
368   27.51   .047 .1730E+01 .3975E-03 .2439E+02
369   27.51   .085 .1729E+01 .3979E-03 .2439E+02
370   27.50   .107 .1728E+01 .3984E-03 .2439E+02
371   27.50   .045 .1727E+01 .3986E-03 .2439E+02
372   27.49  -.016 .1727E+01 .3985E-03 .2439E+02
373   27.49   .005 .1727E+01 .3985E-03 .2439E+02
374   27.49   .042 .1727E+01 .3987E-03 .2439E+02
375   27.48   .014 .1727E+01 .3988E-03 .2439E+02
376   27.48  -.065 .1727E+01 .3985E-03 .2439E+02
377   27.47  -.044 .1728E+01 .3983E-03 .2439E+02
378   27.47  -.073 .1729E+01 .3979E-03 .2439E+02
379   27.46  -.086 .1730E+01 .3975E-03 .2439E+02
380   27.46  -.065 .1731E+01 .3972E-03 .2439E+02
381   27.46  -.012 .1731E+01 .3972E-03 .2439E+02
382   27.45   .008 .1731E+01 .3972E-03 .2439E+02
383   27.45  -.021 .1731E+01 .3971E-03 .2439E+02
384   27.45  -.051 .1731E+01 .3969E-03 .2439E+02
385   27.44   .002 .1731E+01 .3969E-03 .2439E+02
386   27.44   .022 .1731E+01 .3970E-03 .2439E+02
387   27.44   .008 .1731E+01 .3971E-03 .2439E+02
388   27.43  -.005 .1731E+01 .3971E-03 .2439E+02
389   27.43   .015 .1731E+01 .3971E-03 .2439E+02
390   27.43   .034 .1730E+01 .3973E-03 .2439E+02
391   27.42   .004 .1730E+01 .3973E-03 .2439E+02
392   27.42  -.043 .1731E+01 .3972E-03 .2439E+02
393   27.42   .009 .1731E+01 .3972E-03 .2439E+02
394   27.42   .078 .1730E+01 .3975E-03 .2439E+02
395   27.41   .031 .1729E+01 .3977E-03 .2439E+02
396   27.41  -.066 .1730E+01 .3974E-03 .2439E+02
397   27.41  -.030 .1730E+01 .3973E-03 .2439E+02
398   27.41   .022 .1730E+01 .3974E-03 .2439E+02
399   27.40   .007 .1730E+01 .3974E-03 .2439E+02
400   27.40  -.024 .1730E+01 .3973E-03 .2439E+02
401   27.40   .011 .1730E+01 .3974E-03 .2439E+02
402   27.40   .046 .1730E+01 .3976E-03 .2439E+02
403   27.40   .015 .1730E+01 .3976E-03 .2439E+02
404   27.40  -.016 .1730E+01 .3976E-03 .2439E+02
405   27.39   .035 .1729E+01 .3977E-03 .2439E+02
406   27.39   .037 .1729E+01 .3979E-03 .2439E+02
407   27.39  -.011 .1729E+01 .3978E-03 .2439E+02
408   27.39   .007 .1729E+01 .3979E-03 .2439E+02
409   27.39   .075 .1728E+01 .3981E-03 .2439E+02
410   27.39   .076 .1727E+01 .3984E-03 .2439E+02
411   27.38   .028 .1727E+01 .3985E-03 .2439E+02
412   27.38   .013 .1727E+01 .3986E-03 .2439E+02
413   27.38   .014 .1727E+01 .3986E-03 .2439E+02
414   27.38  -.001 .1727E+01 .3986E-03 .2439E+02
415   27.38  -.033 .1727E+01 .3985E-03 .2439E+02
416   27.38  -.065 .1728E+01 .3982E-03 .2439E+02
417   27.38  -.064 .1729E+01 .3980E-03 .2439E+02
    MAX     NP   INDEX     IP
     4      3      1      1
    MAX     NP   INDEX     IP
     4      3      2      2
    MAX     NP   INDEX     IP
     4      3      3      3
   MAX      H       G       SY       SYP
    4   1.000000  .408732E-07  .229003E+01  .229003E+01
      B(1) =    .172850E+01
      B(2) =    .398010E-03
      B(3) =    .243885E+02

  P(1,KP)      P(2,KP)      P(3,KP)      P(4,KP)      P(5,KP)
 .4260245D-01 -.9810103D-05 -.4881226D-02
-.9810103D-05  .2760122D-08 -.1561317D-05
-.4881226D-02 -.1561317D-05  .1734645D-01
  CORRELATION MATRIX
 .1000000E+01
-.9046741E+00  .1000000E+01
```

```
-.1795586E+00 -.2256428E+00  .1000000E+01
XTX(I,K),K=1,NP
 .8875370E+03  .3472562E+07  .5623120E+03
 .3472562E+07  .1396846E+11  .2234441E+07
 .5623120E+03  .2234441E+07  .4170000E+03
XTY(I),I=1,NP, WHERE Y IS RESID
-.2978191E-02 -.9529109E+01 -.3557077E-02
XTY(I),I=1,NP, Y IS Y, NOT RESID
-.1114359E+00 -.5179274E+03 -.6443841E-01
   MAX      NP    INDEX      IP
    4       3       3       4
```

APPENDIX J - A Listing of the Estimated Thermal Diffusivities

Copper Sample:

Test Number	Estimated $\alpha \times 10^6$ [m^2/s]	Test Number	Estimated $\alpha \times 10^6$ [m^2/s]	Test Number	Estimated $\alpha \times 10^6$ [m^2/s]
1	100.24	16	101.23	31	105.56
2	97.23	17	104.35	32	100.52
3	100.98	18	102.91	33	102.94
4	99.54	19	106.86	34	105.57
5	94.02	20	102.095	35	100.34
6	97.59	21	103.56	36	101.268
7	97.8	22	98.86	37	103.45
8	98.82	23	98.669	38	99.47
9	97.6	24	106.16	39	97.17
10	99.44	25	100.3	40	95.24
11	100.31	26	103.18	41	99.57
12	96.68	27	97.88	42	97.26
13	99.29	28	98.54		
14	98.16	29	100.61		
15	100.68	30	100.53		

Iron Sample:

Test Number	Estimated $\alpha \times 10^6$ [m^2/s]
1	14.27
2	11.02
3	13.34
4	12.95
5	12.25
6	13.65
7	13.49
8	10.86
9	11.28
10	10.95
11	13.06
12	13.49
13	13.98
14	11
15	14.09

Diamond Sample AT#4:

Test Number	Estimated $\alpha \times 10^6$ [m^2/s]
1	425
2	401
3	456
4	400
5	410
6	420
7	392
8	428
9	446
10	425
11	377
12	401
13	451
14	396
15	433

Diamond Sample ST#192:

Test Number	Estimated $\alpha \times 10^6$ [m^2/s]
1	492
2	457
3	442
4	474
5	479
6	480
7	499
8	476
9	497
10	492
11	436
12	490
13	481
14	459

APPENDIX K - Fast Line Scan Mode

Introduction:

The Inframetrics Model 600L radiometer is equipped with a high speed measurement mode known as the fast line scan mode. This feature is designed to capture thermal events along a line with a sampling rate of 8 KHz.

The horizontal scan mechanism in the radiometer is a resonant galvanometer. The frequency of this galvanometer is 3933 Hz. The "galvo" operates in a sinusoidal scan mode and produces 3933 left to right scans and 3933 right to left scans in one second. Therefore during this second 7866 lines are scanned. This results in a difference of 127.1 microseconds between consecutive scan lines.

In order to scan at this rate the vertical scan galvanometer is stopped *somewhere* near the center of the field of view. In many application it is important to know which line is being measured. In this study a simple experiment, shown in Figure 1 and Figure 2, was conducted to determine if the vertical scan galvanometer is positioned in the same location each time the fast line scan mode is used.

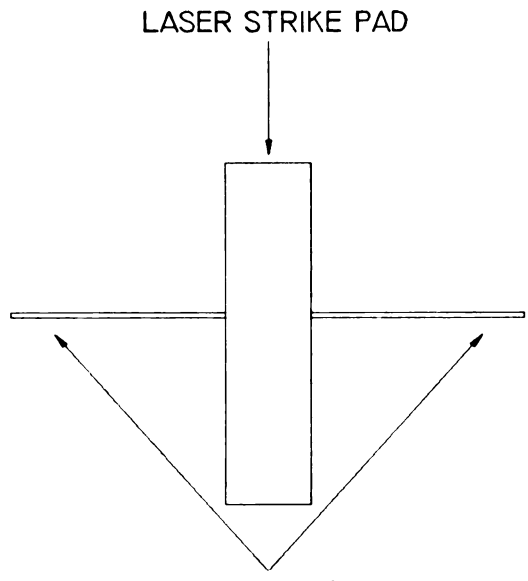

Figure 1. *Copper test specimen used for fast line scan mode experiment.*

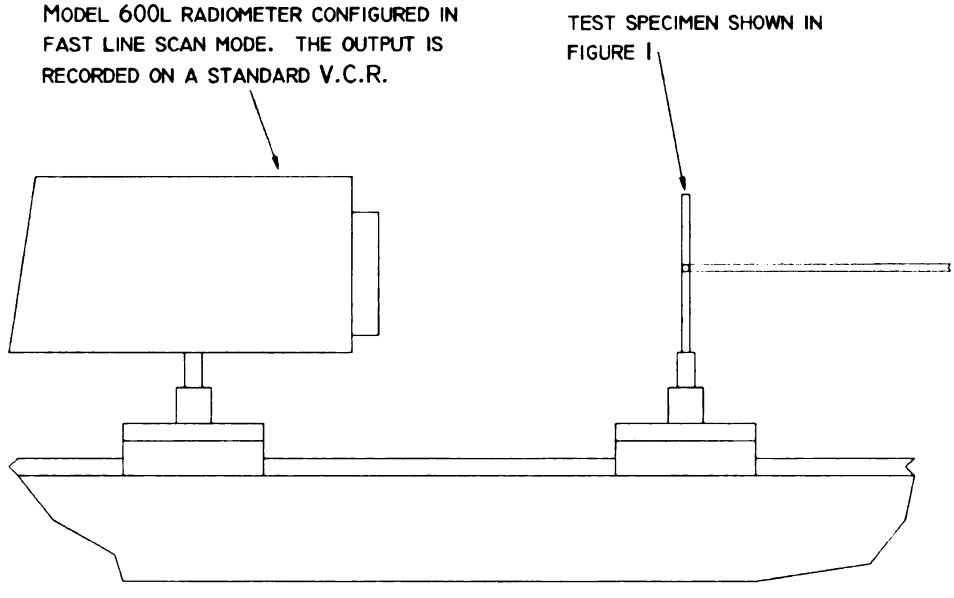

Figure 2. *Experimental Setup*

Experiment and Results

In this experiment the beam of the Nd:YAG laser is positioned in the center of the laser strike pad shown in Figure 1. The two thin fins are used to carry heat away from the strike pad.

The radiometer is configured in the fast line mode and the temperatures are recorded along *some* line at ~8000 Hz.

The measured temperatures will depend on the location of the vertical scan galvanometer. In this experiment several measurements were taken and the test specimen was adjusted to vertically move the position of the thin fins. In the first series of tests, the specimen was positioned in a way that the line scan mode would not read the temperatures along the two thin fins. The results are shown in Figures 3 and 4.

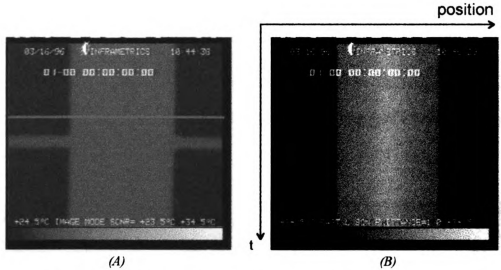

Figure 3. (A) Radiometer placed in image mode. The red line indicates approximate location of the fast line scan. (B) The radiometer is placed the fast line scan mode and the specimen heated with a Nd:YAG laser.

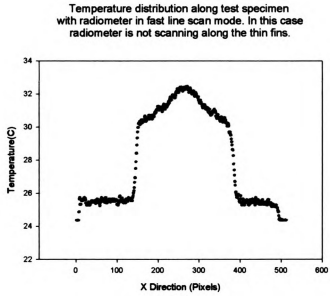

Figure 4. The temperature profile along a line not corresponding to the location of the two thin fins.

In the next series of tests, the specimen was positioned so the line scan mode would read the temperature distribution along the thin fins. The results of these tests are shown in Figure 5 and Figure 6.

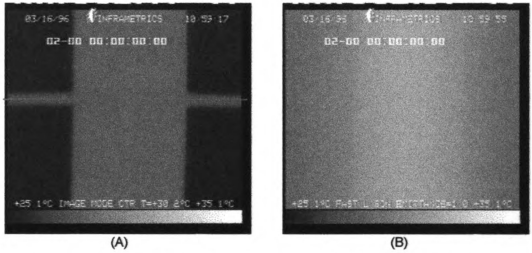

Figure 5. *(A) Radiometer placed in image mode. The red line indicates approximate location of the fast line scan. (B)The radiometer is placed the fast line scan mode and the specimen heated with a Nd:YAG laser.*

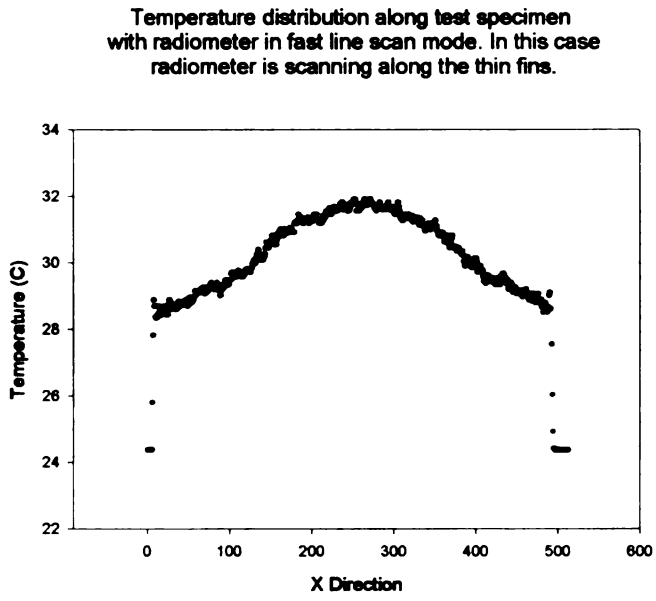

Figure 6. *The temperature profile along a line corresponding to the location of the two thin fins.*

Tests similar to this were repeated several times. It was found that the vertical scan "galvo" positions itself in the same location of the radiometer field of view each time the fast line scan mode in used. When data is analyzed with the ThermoGRAM processing software this position corresponds to line number 95.